ÇUKUROVA UNIVERSITY
INSTITUTE OF NATURAL AND APPLIED SCIENCES

MSc. THESIS

Engin PINAR

EXPERIMENTAL INVESTIGATION OF THE FLOW STRUCTURE AROUND SPHERES PLACED SIDE BY SIDE

DEPARTMENT OF MECHANICAL ENGINEERING

ADANA, 2009

INSTITUTE OF NATURAL AND APPLIED SCIENCES
UNIVERSITY OF CUKUROVA

EXPERIMENTAL INVESTIGATION OF THE FLOW STRUCTURE AROUND SPHERES PLACED SIDE BY SIDE

Engin PINAR
M.Sc. THESIS

DEPARTMENT OF MECHANICAL ENGINEERING

We certified that the thesis titled above was reviewed and approved for the award of degree of master of science by the board of jury on ……..

Signature:……	Signature:……	Signature:……
Prof.Dr.Beşir ŞAHİN	Assoc.Prof.DrHüseyinAKILLI	Assist.Prof .Dr.Sami AKÖZ
Advisor	Member	Member

This M.sc. Thesis is performed in Department of Mechanical Engineering of Institute of Natural and Applied Sciences of Cukurova Universty.

Registration Number

Prof. Dr. Aziz **ERTUNÇ**
Director
The Institute of Natural and Applied Sciences

Not: The usage of the presented specific declarations, figures, and photographs either in thesis or in any other reference without citiation is subject to " The law of Arts and Intellectual Products" numbered 5846 of Turkish Republic.

ABSTRACT

M.Sc.THESIS

EXPERIMENTAL INVESTIGATION OF THE FLOW STRUCTURE AROUND SPHERES PLACED SIDE BY SIDE

Engin PINAR

DEPARTMENT OF MECHANICAL ENGINEERING
INSTITUTE OF NATURAL AND APPLIED SCIENCES
UNIVERSITY OF ÇUKUROVA

Supervisor : Prof. Dr. Beşir ŞAHİN
Year : 2009, Pages: 99
Jury : Prof. Dr. Beşir ŞAHİN
Assoc. Prof. Dr. Hüseyin AKILLI
Assist. Prof. Dr. Sami AKÖZ

The aim of this work is to investigate details of flow structure around sphere and cylinder in a free-stream flow using both the dye visualization and laser based particle image velocimetry (PIV) technique. Experiments were classified in two parts. Firstly, Flow structure around the sphere and cylinder were compared with each other for Reynolds number Re=5000. Secondly, Three dimensional flow characteristics around a single sphere and side-by-side spheres were investigated at Re= 5000 based on the diameter of the sphere. Experiments were conducted both in the plan-view and end-view planes in order to understand complex flow structure in the downstream region of the sphere(s) for values of gap ratios (G/D) of 1.0, 1.25, 1.5 and 2.0 and for values of length ratios (L/D) of 0.50, 0.75, 1.50, 3.00. Results obtained in this study provide information which designers need for various industrial applications such as designing low drag vehicles and drying process of some product etc. The quantitative results of turbulence characteristics were presented with the time-averaged and instantaneous velocity vectors, vorticity contours, streamlines, velocity fluctuations of U_{rms} and V_{rms} and variations of turbulence stress which were using the experimental results of PIV.

Keywords: **Cylinder, PIV, Side by side spheres, Wake region**

ÖZ

YÜKSEK LİSANS TEZİ

YAN YANA KÜRELER ETRAFINDAKİ AKIŞ YAPISININ DENEYSEL İNCELENMESİ

Engin PINAR

ÇUKUROVA ÜNİVERSİTESİ
FEN BİLİMLERİ ENSTİTÜSÜ
MAKİNA MÜHENDİSLİĞİ ANABİLİM DALI

Danışman : Prof. Dr. Beşir ŞAHİN
Yıl : 2009, Sayfa:99
Jüri : Prof. Dr. Beşir ŞAHİN
Doç.Dr. Hüseyin AKILLI
Yrd.Doç.Dr. Sami AKÖZ

Bu çalışmanın amacı serbest akışta küre ve silindir etrafındaki akış yapısını hem boya ile görüntüleme hem de Parçacık Görüntülemeli Hız Ölçme (PIV) yöntemiyle incelemektir. Deneyler iki kısma ayrılmıştır. İlk olarak, küre ve silindir etrafındaki akış yapısı Reynolds sayısının 5000 değeri için bir biri ile karşılaştırılmıştır. İkinci olarak, tek ve yan yana iki küre etrafındaki üç boyutlu akış yapısı küre çapına bağlı olarak Re=5000 değerinde incelenmiştir. Deneyeler hem düzlemsel hem de bu düzleme dik düzlemlerde kürenin arkasındaki karmaşık akış yapısını anlamak için boşluk oranının (G/D) 1.0, 1.25, 1.50 ve 2.0 değerleri ile uzunluk oranının (L/D) 0.50, 0.75, 1.50, 3.00, değerleri için gerçekleştirilmiştir. Bu çalışmanın sonuçları düşük sürüklenme katsayılı araçların tasarlanması ve bazı ürünlerin kurutulması gibi çeşitli endüstriyel uygulamalar için tasarımcılara ihtiyaç duydukları bilgiyi sağlayacaktır. PIV deneylerinden elde edilen verilerin analizi sonucunda ortalama ve anlık hız vektörleri, girdap eş değer eğrileri, akım çizgileri, U_{rms} ve V_{rms} çalkantı hızları, akışa ait türbülans gerilmelerinin nitel sonuçları gösterilmiştir.

Anahtar kelimeler: Ard izi, PIV, Silindir, Yan yana dizili küreler,

ACKNOWLEDGEMENTS

This list endless if I have to thank all the people that made possible this work. My first thanks goes to my advisor Prof. Dr. Beşir ŞAHİN for his support, guidance and encouragement. He has been a great source of motivation, both personal and technical. His generous advices, encouragements and constant faith have made my time with him is a very challenging and rewarding experience.

I would like to thank Assoc.Prof. Dr. Muammer ÖZGÖREN for his continues support, useful comments, help, encouragements for creating research opportunities and sharing his knowledge and helping in conduction of experiments.

I would also like to thank Assoc.Prof. Dr. Hüseyin AKILLI for their very useful comments. This work could never have been completed without the unselfish help of him. I would like to thank him for the countless hours of discussion about fluid mechanics and his sincere interest in my research.

I would like to thank Assist.Prof. Dr Atakan AKAR and Reserch. Asist. Sedat YAYLA sharing their knowledge and experiance and for moral support.

I owe special thanks to Mr Kamil PAYDAŞ and Mrs Burcu Elveren OĞUZ and Mr. Arda MATUR. I really appreciate their providing everything necessary to complete this work and continuous moral support, help and excellent friend ship.

My sincere thanks go to, Reserch. Asist Çetin CANPOLAT for continuous moral support, helping in conduction of experiments and writting my thesis and friend ship.

On a personal level many thanks go to my friends Mr. Alper Öncebe, Mr. Volkan Vural TAŞ and Mr Atilla ÖZ for their moral support, help and friendship.

I also want to thank, My close friend Mr.Gökhan FİLİK and his family for their continuous moral support, excellent friend ship and sharing their house with me.

Last but not least, I would like to thank my mother Nesrin ÖRENER, my brother Özgür PINAR, my little brother Çağdaş PINAR, my father Hasan PINAR and his wife Ayla PINAR for their patience and trust. Finally I would like to thank my lovely uncle Asım ÖRENER who we lost during my study of thesis and his family for their support and trust.

TABLE OF CONTENTS Page

ABSTRACT…… I

ÖZ..... II

ACKNOWLEDGEMENTS…… III

TABLE OF CONTENTS……..…….. IV

LIST OF FIGURES……...…….. VI

NOMENCLATURE…… XII

1. INTRODUCTION……...…….. 1

1.1 Flow structure of near wake behind a sphere depending on the Reynolds Number……. 1

1.1.1 Region I (20<Re<800) …….. 1

1.1.2 Region II (800<Re<3.7x10^5) …….. 4

1.1.3. Region III (Re ≥ 3x10^5) ……... 5

1.2 Changing St number with Re number…… 5

1.3 Flow around a Cylinder……. 7

2. PREVIOUS STUDIES……... 11

2.1. Flow structure around spheres ……...…….. 11

2.2. Flow structure around cylinders …… 19

3. MATERIAL METHOD…….……..... 23

3.1. Experimental Arrangement…… 23

3.1.1. Water Channel System……..... 23

3.2. Measurement Techniques…… 25

3.2.1. Flow Visualization Techniques…… 25

3.2.2. Particle Image Velocimetry (PIV) Techniques ……... 26

3.2.2.1. Principles of PIV ……..…. 28

3.2.2.2. Image Acquisition ……... 30

3.2.2.3 Seeding …… 30

3.2.2.4. Illumination …… 31

3.2.2.5. Cameras (Image Capturing) ….…..... 32

3.2.2.6. Correlation (Image Evaluation) ……..…… 33
3.2.2.7. Validation and further analysis (Image Post-Processing)…… 34
4. RESULT AND DISCUSSIONS……..... 36
4.1. Experimental investigation of flow structure around a sphere and cylinder via flow visualization…… 36
4.1.1. Introduction ……...……...…. 36
4.1.2. Experimental Arrangement …….……... 37
4.1.3 Results and Discussion……. 41
4.2.3.1. Dye visualization Results 41
4.2.3.2. Spectral analysis and calculation of vortex shedding frequency..... 44
4.1.3.3. Particle Image Velocimetry (PIV) Results……. 46
4.2. Investigation of three Dimensional Flow characteristics around side by side spheres ……... 56
4.2.1. Introduction……..…. 56
4.2.2. Experimental Arrangement …… 57
4.2.3. Results and Discussion …….. 60
4.2.3.1 Dye visualization Results 60
4.2.3.2 Particle Image Velocimetry (PIV) Results 64
5. CONCLUSIONS…….……... 92
REFERENCES…….…… 95
CIRRICULUM VITAE……... 99

LIST OF FIGURES Page

Figure 1.1.	Schematic representations of hairpin vortex Achenbach, (1974)	2
Figure 1.2.	Side views of the periodic wake of a single sphere at *Re* = 300. (a) Dye visualisation; (b) vortical structures from DNS (Schouveiler et al, 2004)	3
Figure 1.3.	Variation of C_d with Reynolds number.	4
Figure 1.4.	Strouhal number based on hairpin-shaped vortex and large-scale vortex shedding versus Reynolds number (Sakamoto and Haniu, 1990)	6
Figure 1.5.	The Kelvin-Helmholtz (secondary) vortices and the Karman vortices from circular cylinder.	9
Figure 3.1.a.	Representation of Plan view setup	24
Figure 3.1.b.	Representation of Side view setup	24
Figure 3.2.	Overview of dye visualization technique around side-by-side sphere	25
Figure 3.3.	A typical PIV experimental set-up (McLean, 2007)	26
Figure 3.4.	Overview of (PIV) visualization technique around side-by-side sphere	27
Figure 3.5.	Interrogation areas	29
Figure 3.6.	Schematic of experimental apparatus and digital PIV instrumentation	30
Figure 3.7.	PIV overview (Schiwietz, T., Westermann, R., 2004)	33
Figure 4.1.	Schematic of the experimental system and definition of the parameters for the cylinder and the sphere.	39
Figure 4.2.	The scheme of experimental arrangements which includes positions of camera and laser	40
Figure 4.3.	Instantaneous flow visualization with laser illumination of Rhodamine dye injection technique in near wake	42

region around a sphere is illustrated. Evolution stages of the flow structure are shown at Re=5000. Dye ports are made on the sphere equator with a diameter of 0.5mm.

Figure 4.4. Instantaneous flow visualization with laser illumination of Rhodamine dye injection technique around a cylinder for Re=5000 in shallow water is displayed (Akilli et at.2007). 43

Figure 4.5. Instantaneous flow visualization with laser illumination of Rhodamine dye injection technique in far wake region around a sphere for Re=5000 is shown. 44

Figure 4.6. Time history of instantaneous streamwise velocity component u (mm/s) against time t (s) and spectrum analysis Su for the cylinder (top two graphics) and the sphere (bottom two graphics) at Re = 5000. 45

Figure 4.7. Comparison of patterns of instantaneous vorticity ω for the cylinder (left column) and the sphere (right column) is presented. Both minimum and incremental contour levels of positive (solid line) and negative (dashed line) instantaneous vortices in all images are 6 (1/sec). All patterns are scaled with respect to the bluff body size. 47

Figure 4.8. Comparison of flow patterns of the cylinder (left column) and the sphere (right column) for dimensionless time-averaged velocity field <V>, streamline topology <y>, streamwise velocity <u> cross-stream velocity <v> is shown for Re=5000. Minimum and incremental values of the patterns are given on each image. All patterns are scaled with respect to the bluff body size. 50

Figure 4.9. Comparison of dimensionless time-averaged flow patterns of vorticity <ω>, streamwiseReynolds normal stress <u'u' U_∞^2 > , transverse Reynolds normal stress < v'v' U_∞^2 > and Reynolds stress correlations < u'v' U_∞^2 > 52

is given for Re=5000 for a cylinder (left columnn) and sphere (right column). Minimum and incremental values of the patterns are given on each image. All patterns are scaled with respect to the bluff body size.

Figure 4.10. Comparison of dimensionless time-averaged flow patterns of rms contours of the streamwise velocity $< urms\ U_\infty >$, cross-stream velocity $< vrms\ U_\infty >$, vortcity $<U_\infty\ rms\ w>$ is diplayed for Re=5000 for a cylinder (left columnn) and sphere (right column). Minimum and incremental values of the patterns are given on each image. All patterns are scaled with respect to the bluff body size. 55

Figure 4.11 a) spheres used dye experiments b) Spheres used PIV experiments 57

Figure 4.12. Sketch of the special aperture 58

Figure 4.13. Schematic of the experimental system and definition of parameters for the sphere. 59

Figure 4.14. Dye visualization results for single and side by side sphere with various gap ratios for small wake region, Re=5000, G/D = b)1.00, c)1.25, d)1.50, e)2.00 62

Figure 4.15. Dye visualization results for single and side by side sphere with various gap ratios for large wake region, Re=5000, G/D = b)1.00, c)1.25, d)1.50, e)2.00 63

Figure 4.16. Patterns of a) time-averaged velocity vector <V>, b) instantaneous velocity vectors V, c) instantaneous vorticity contours ω, $|\Delta_{min}|=2$ d) time-averaged streamlines $<\psi>$, for the case of single sphere, Re=5000. 66

Figure 4.17. Patterns of a) time-averaged vorticity contours $|<\omega_{min}>|= 2$, $<\Delta\omega>=1.5$ b) Reynolds stress contours, |< 64

$(u'v'/U^2)_{min}>|$ =0.004 $<\Delta(u'v'/U^2)>$=0.004 c) square root of streamwise velocity, <(Urms/U)min>= 0.004, ΔUrms=0.002 d) square root of transverse velocity<(Vrms/U)min>= 0.004 ve ΔVrms=0.002 for the case of single sphere, Re=5000.

Figure 4.18. Patterns of time-averaged velocity vector, <V> of two side by side spheres for the gap ratios of G/D=1.00, 1.25, 1.50, 2.00, 2.50, Re=5000. 67

Figure 4.19. Patterns of instantaneous velocity vector, V of two side by side spheres for the gap ratios of G/D=1.00, 1.25, 1.50, 2.00, 2.50, Re=5000. 68

Figure 4.20. Patterns of instantaneous vorticity contours ω, $|\Delta_{min}|$=2 of two side by side spheres for the gap ratios of G/D=1.00, 1.25, 1.50, 2.00, 2.50, Re=5000. 69

Figure 4.21. Patterns of time-averaged streamlines, Ψ of two side by side spheres for the gap ratios of G/D=1.00, 1.25, 1.50, 2.00, 2.50, Re=5000. 70

Figure 4.22. Patterns of Reynolds stress contours, $| < (u'v'/U^2)_{min}>|$ =0.004 $<\Delta(u'v'/U^2)>$=0.004 of two side by side spheres for the gap ratios of G/D=1.00, 1.25, 1.50, 2.00, 2.50, Re=5000. 72

Figure 4.23. Patterns of square root of streamwise velocity, $<(Urms/U)_{min}>$= 0.004, ΔUrms=0.002 of two side by side spheres for the gap ratios of G/D=1.00, 1.25, 1.50, 2.00, 2.50, Re=5000. 75

Figure 4.24. Patterns of square root of transverse velocity, $<(Vrms/U)_{min}>$= 0.004, ΔVrms=0.002 of two side by side spheres for the gap ratios of G/D=1.00, 1.25, 1.50, 2.00, 2.50, Re=5000. 76

Figure 4.25. Patterns of time-averaged vorticity contours $|<\omega_{min}>|$= 2, 77

$<\Delta\omega>$=1.5 of two side by side spheres for the gap ratios of G/D=1.00, 1.25, 1.50, 2.00, 2.50, Re=5000.

Figure 4.26. Patterns of time-averaged velocity vectors, <V> of the single sphere on end-view cross-section for L/D=0.50, 0.75, 1.50, 3.0, Re=5000. 79

Figure 4.27. Patterns of time-averaged vorticity contours $|<\omega_{min}>|$= 0.5, $<\Delta\omega>$=0.5 of the single sphere on end-view cross-section for L/D=0.50, 0.75, 1.50, 3.0, Re=5000. 80

Figure 4.28. Patterns of instantaneous vorticity contours $|<\omega_{min}>|$= 5, $<\Delta\omega>$= 5 of the single sphere on end-view cross-section for L/D=0.50, 0.75, 1.50, 3.0, Re=5000. 81

Figure 4.29. Patterns of time-averaged streamlines, Ψ of the single sphere on end-view cross-section for L/D=0.50, 0.75, 1.50, 3.0, Re=5000. 82

Figure 4.30. Patterns of time-averaged velocity vectors, <V> of the two side by side spheres on end-view cross-section for L/D=0.50, 0.75, 1.50, 3.0 and gap ratio of G/D=1.0, Re=5000. 84

Figure 4.31. Patterns of time-averaged velocity vectors, <V> of the two side by side spheres on end-view cross-section for L/D=0.50, 0.75, 1.50, 3.0 and gap ratio of G/D=1.25, Re=5000. 85

Figure 4.32. Patterns of time-averaged velocity vectors, <V> of the two side by side spheres on end-view cross-section for L/D=0.50, 0.75, 1.50, 3.0 and gap ratio of G/D=1.50, Re=5000. 86

Figure 4.33. Patterns of time-averaged velocity vectors, <V> of the two side by side spheres on end-view cross-section for L/D=0.50, 0.75, 1.50, 3.0 and gap ratio of G/D=2.00, 87

Re=5000.

Figure 4.34. Patterns of time-averaged streamlines, Ψ of the two side by side spheres on end-view cross-section for L/D=0.50, 0.75, 1.50, 3.0 and gap ratio of G/D=1.00, Re=5000. 88

Figure 4.35. Patterns of time-averaged streamlines, Ψ of the two side by side spheres on end-view cross-section for L/D=0.50, 0.75, 1.50, 3.0 and gap ratio of G/D=1.25, Re=5000. 89

Figure 4.36. Patterns of time-averaged streamlines, Ψ of the two side by side spheres on end-view cross-section for L/D=0.50, 0.75, 1.50, 3.0 and gap ratio of G/D=1.50, Re=5000. 90

Figure 4.37. Patterns of time-averaged streamlines, Ψ of the two side by side spheres on end-view cross-section for L/D=0.50, 0.75, 1.50, 3.0 and gap ratio of G/D=2.00, Re=5000. 91

NOMENCLATURE

V	: Free stream velocity
S	: Saddle point
F	: Focus
N	: Nodal point
$<\omega>$	: Time-averaged vorticity
ω	: Instantaneous vorticity
$<\Psi>$	: Time-averaged streamline
<V>	: Time-averaged velocity distribution
V	: Instantaneous velocity distribution
Re	: Reynolds number depending on the sphere diameter
U	: Stremavise Velocity Component
V	: Transverse Velocity Component
$u'v'/U^2$	: Reynolds stress correlations
U_{rms}/U	: Square root of streamwise velocity
V_{rms}/U	: Square root of transverse velocity
ω^*	: Normalized vorticity ($\omega^*=\omega.c/U_\infty$)
f	: Frequency
D	: Sphere Diameter
St	: Strouhal Number
G/D	: Ratio of gap distance between central points of spheres and sphere diameter
L/D	: Ratio of distance between measurement section and central point of spheres in end-view plane and sphere diameter

1. INTRODUCTION

Flow past a bluff body such as a sphere and cylinder is a generic flow–structure interaction having important implications for flow-induced vibration and noise generation. It has been attracted a great deal of attention recently. Bluff bodies such as cylinder and sphere usually cause massive flow separation, unsteady flow, and complicated vortex shedding. It is well known that the sphere and cylinder do not have a fixed flow separation point, depending on the Reynolds number, surface characters, control techniques, multiple arrangement, blockage ratio, alignment and so on. Moreover, the separation points have been known to move along the sphere and cylinder surfaces depending on the condition of the outer flow and boundary layer developed on the sphere surface. To design low drag vehicles or to apply flow control schemes to a bluff body, an understanding of the physical nature of the flow around a bluff body is essential. The flow in the near-wake region behind the cylinder and sphere, incorporating the vortex formation region, plays an important role in determining the steady and unsteady forces acting on the body Ozgoren et al (2009) .

Although a spherical body is perfectly axi-symmetric, the vortical structure around it has been known to show diverse flow characteristics such as axi-symmetric flow, planar symmetric flow, and irregular rotation of separation points, unsteady flow, periodic vortex shedding, laminar wake, shear layer instability, turbulent wake, and turbulent separation, depending on the Reynolds number. Jang and Lee (2007).

1.1. Flow structure of near wake behind a sphere depending on the Reynolds Number

1.1.1. Region I (20<Re<800)

The flow around a sphere shows steady axi-symmetric flow in the range of Reynolds number 20–210. The axisymmetry is then broken, and planar-symmetric flow appears until Reynolds number Re = 280 based on sphere diameter. According to taneda's flow-visualization experiment in the range of 5<Re<300 (Taneda 1956), When the Re is over 130, faint periodic pulsative motion with a very long period

occurs at rear of the vortex-ring formed behind the sphere. From Re = 280, unsteadiness starts to occur in the planar-symmetric flow, Vortex shedding begins to occur when Re number is passed the value of approximately Re=300. After Re=300, the vortex structure is converted to vortex called hairpin. Vortex shedding occur different frequencies, regimes and similar vortex structure up to certain high Re numbers and hairpin vortices are periodically shed. Hairpin vortex structure determined by Achenbach (1974) is shown below both in plan-view and side-view in Figue1.1.

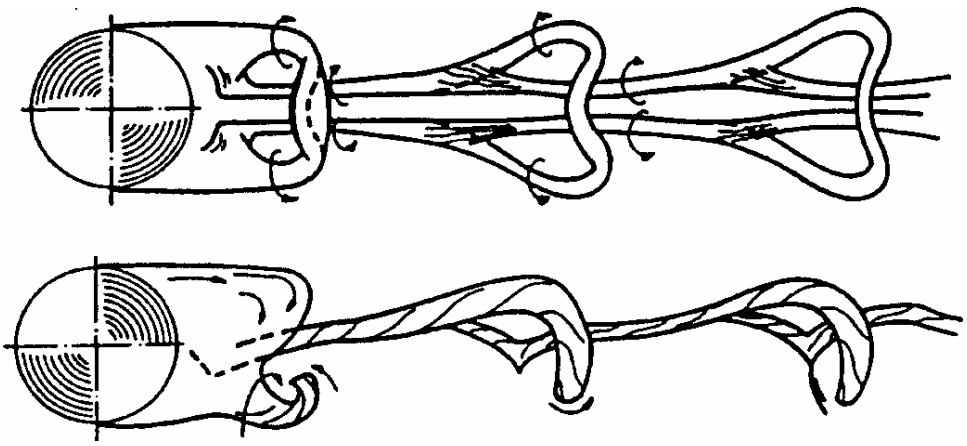


Figure 1.1. Schematic representations of hairpin vortex (Achenbach, 1974)

a)

b)

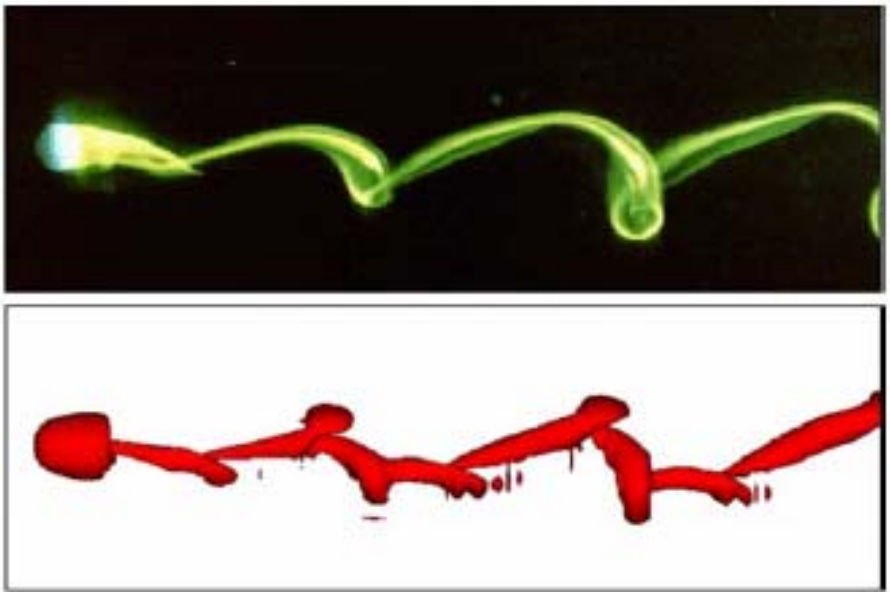


Figure 1.2. Side views of the periodic wake of a single sphere at *Re* = 300.
(a) Dye visualisation; (b) vortical structures from DNS (Schouveiler et al, 2004)

In the range of Reynolds number 420≤Re≤800, asymmetric flow is observed, and unsteadiness continues (Taneda 1956; Nakamura 1976; Wu and Faeth 1993; Johnson and Patel 1990; Leweke et al. 1999). Many experimental and numerical research works on sphere wake have been carried out in this Reynolds number range to study laminar flow separation and laminar wake . When the Re is grater than 420, the amplitude and wave form of the fluctuating velocity based on the shedding of the hairpin-shaped vortices begin to be generated with irregularity, and their shedding direction oscillates intermittently from left to right as described Sakamoto and Haniu (1990) . When the Re exceeds 480, the waveform of fluctuating velocity based on the shedding of the hairpin-shaped vortices becomes irregular. In other words, the shedding pattern of the vortex is always in the irregular mode. Sakamoto and Haniu (1990) also studied Reynolds number 650, the cylindrical vortex sheet separated from the sphere surface develops pulsation mode, and the vortex tubes begin to be

periodically shed in accordance with the pulsation as if covering the vortex formation region.

1.1.2 Region II (800<Re<3.7x10^5)

When the Reynolds number exceeds Re = 800, the large-scale low-frequency vortex shedding and small-scale high-frequency shear layer instabilities become prominent flow phenomena. A large-scale vortex is shed with wavy shape, and turbulence occurs in the far field. This range of Reynolds number is called as a subcritical region in the literature. Jang and Lee (2007) stated that in the subcritical Reynolds numbers from Re=800 to Re=3.7x105, the drag coefficient of a sphere has almost constant values, and the flow separates laminarily from the sphere. In addition, Kelvin–Helmhortz instability occurs in the separating shear layers, and the wake becomes turbulent. The laminar flow separation begins at approximately 80^o-90^o from the stagnation point on the upstream of the sphere at Re=2x10^5 in subcritical flow region and drag coefficient, is approximately 0.5. These values are almost constant independent from Reynolds number. The drag coefficient C_d drops rapidly to nearly 0.07 and separated flow region change into downstream side of the sphere in subcritical flow region (2x10^5<Re<3.7x10^5) Ozgoren et al. (2009). Figure 1.3 presents the variation of C_d against Reynolds number.

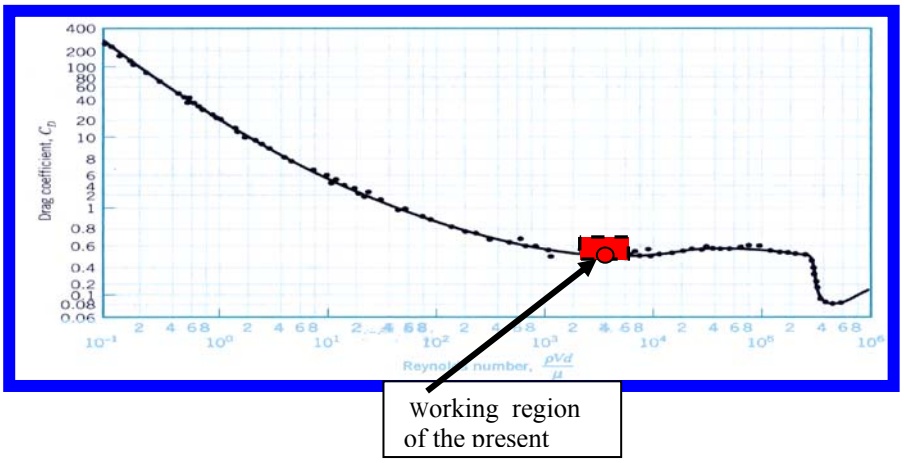


Figure1.3. Variation of C_d with Reynolds number.

1.1.3. Region III (Re ≥ 3x10^5)

At the critical Reynolds number of Re = 3.7x105, the drag coefficient is rapidly reduced. This happens due to the sequential laminar separation, reattachment, and turbulent separation from the boundary layer of the sphere. The sphere wake becomes fully turbulent beyond this critical Reynolds number. In this region, the drag coefficient Cd increases in a bit with increasing Reynolds number and supercritical flow region. becomes turbulent. A few experimental studies on the turbulent flow around a sphere have been conducted in the subcritical Reynolds number regime. Most of them focused on the vortex shedding phenomena by measuring the dominant shedding frequencies using a hot-wire anemometry and on wake structures with qualitative flow visualization methods Achenbah (1972, 1974) Werle (1980), Constantinescu and Squires (2003, 2004), Kim and Durbin (1988). The experimental measurements of turbulent flow around a sphere are not easy to carry out. This is attributed to several factors such as supporting difficulty of a sphere in the wind tunnel test section, strong time dependency of the flow field, large area of separated flow, and three-dimensional complicated flow structure

1.2. Changing St number with Re number

The frequency of the vortex shedding is indicated with dimensionless Strouhal number, St like cylinder. Strouhal number, St is shown as a function of Reynolds number for the flow structure around sphere. Strouhal number (Strouhal 1878) St (Strouhal number, $S_t = f\,D/\,U_\infty$, where *f* is the frequency, D is the cylinder diameter, U_∞ is the free-stream velocity, and the vortices produced in this manner are termed Strouhal vortices.

$$St = f\frac{D}{V}$$

f: Frequency of Vortex Shedding(Hz)

D: Sphere Diameter

V: Free Stream Velocity

Figure1.4. represents variation of Strouhal number, St based on hairpin-shaped vortex and large-scale vortex shedding versus Reynolds number (Sakamoto and Haniu, 1990)

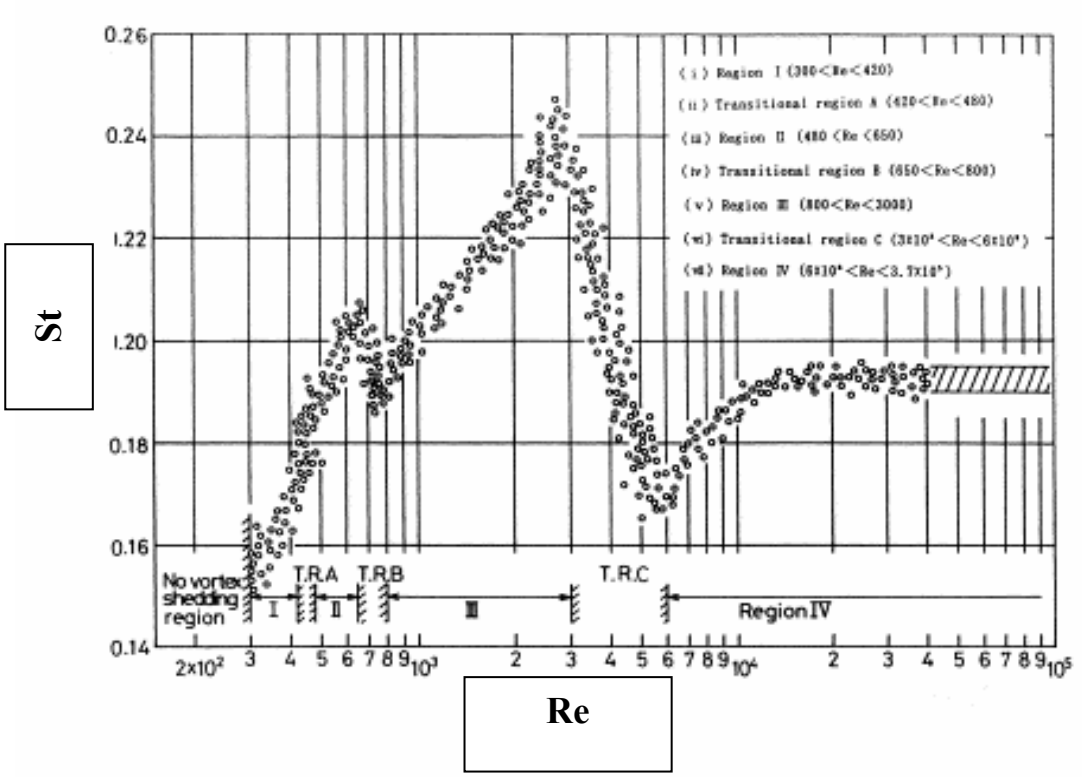


Figure 1.4. Strouhal number, St based on hairpin-shaped vortex and large-scale vortex shedding versus Reynolds number (Sakamoto and Haniu, 1990)

In the range of 300<Re<650, St number increases to a value of (0.16 – 0.21)

650<Re<800, St number decreases to a value of (0.21 – 0.19)

800<Re<3000, St number increases to a value of (0.19 – 0.24)

3000<Re<6000, St number decreases to a value of (0.24 –0.17)

6000<Re<20000, St number increases to a value of (0.17- 0.19)

For Re>20000, St number has a constant value of 0.19

1.3. Flow around a Cylinder

Bluff body is a widely studied problem since the study of Strouhal (Strouhal , 1878) who observed vortex shedding from a circular cylinder. Most of works were carried out on the cylinders having circular, square and rectangular cross-section, but the flow around circular cylinders remains the principal subject of researchers because, despite the geometric simplicity, the mechanisms involved are complex and the flow patterns are not easy to understand, especially for large Reynolds numbers and when control processes are implemented.

When a flow goes across a circular cylinder, complex flow phenomena and behaviors in the vicinity of the cylinder surface and the wake region, e.g. flow separation, vortex shedding and shear-layer instability etc., are usually induced in different regimes of Reynolds numbers. These flow phenomena would inevitably apply unsteady lift and drag forces to the cylinder (Huang et al. 2005) . In the absence of external forces, the dynamics of flow around a cylinder depends only on the Reynolds number ($Re = U_\infty D / \nu$ where U_∞ is the free-stream velocity far from the cylinder, d the cylinder diameter and ν the kinematic viscosity). Properties of this flow are well-known for a wide range of flow regimes, from creeping flows ($Re << 1$) to fully turbulent flows ($Re \approx 10^7$) (Delaunay and Kaiktsis 1999). The flow regimes at low Reynolds numbers can be classified as follows:

For $Re < 6$, the flow is steady and two-dimensional, with only one separation point, at the rear stagnation point. In the range $6 < Re < 47$, the flow is still steady and two-dimensional, but a vortex pair appears behind the cylinder (Jackson 1987) , whose recirculation length increases linearly with *Re*. At the critical Reynolds number ($Re \approx 47$), Henderson and Barkley (1996) discussed that unsteadiness arises spontaneously even though all the imposed conditions are being held steady and vortex shedding appears behind the circular cylinder, resulting in the well-known von Karman vortex street. When a vortex is shed from one side of the cylinder, a negative pressure pulse is generated on the side whereas a positive pressure pulse is generated on the other side; alternate vortex shedding from the upper and lower sides of the cylinder produces negative and positive pulses alternately and thus produces

sound pressure waves on both sides; the frequency of the sound pressure waves is the same as that of vortex shedding as well as the fluctuation frequency of the lift force.

When Re <200, vortex shedding occurs in the near wake behind the cylinder accompanying a periodically oscillating lift force. Each half of the period, a vortex breaks off, so the surface pressure distribution around the cylinder changes dramatically as the cylinder experiences a sudden impulse. These vortices generate alternating high and low pressure regions on the lee side of the body in such a way that the cylinder experiences a periodic net force. This oscillation may amplify the vortex shedding, because now the cylinder itself is moving in the flow, forcing the vortex street to occur with large amplitude as described by Vallejo (1984) .

Finally for higher values of Re, that is, when Re > 200, the flow becomes three-dimensional and turbulent.

1.2. Karman Vortices and Kelvin-Helmholtz Vortices

Two types of streamwise vortices have been reported in the laminar and transitional wakes of cylinders. At a sufficiently high value of Reynolds number, so-called “transition waves” appears in the shear layer separating from the surface of the cylinder. These waves are detectable in the region of the wake extending from the separation point on the body to the first appearance of the large-scale Karman vortex. As a result, a vortex is shed from the cylinder when the local pressure changes each time. Therefore, the cylinder is subjected to a fluctuating drag and lift in addition to the mean drag and lift. The drag, lift and vortex shedding frequency are normally expressed in non-dimensional forms as the drag coefficient C_D, the lift coefficient C_L, and the Strouhal number St. These three non-dimensional parameters depend on the nature of both the approaching flow and the cylinder. When the cylinder is located near a plane boundary, the bed proximity and the velocity gradient in the boundary layer, as well as the turbulent characteristics of the boundary layer, also have some influence on these parameters.

When the value of Reynolds number is sufficiently high, then these transition waves take the form of train of Kelvin-Helmholtz vortices shown in Figure 1.4. In

the bluff body community, these small-scale vortices are often referred to as Bloor-Gerrard vortices. The onset of "transition waves" is expected to be strong function of the disturbance level of the free stream, in view of the fact that they arise from convective-type instability, as described by Ho and Huerre (1984). Bloor (1964) detected the small-scale vortices for the range of Reynolds number Re>1300, however, Ünal and Rockwell (1988) first noted these vortices at Re_D=1900. Wu et al. (1994) discussed the possible influence of background disturbance levels and observed these waves over the range of Reynolds numbers $1000 \leq Re \leq 3000$.

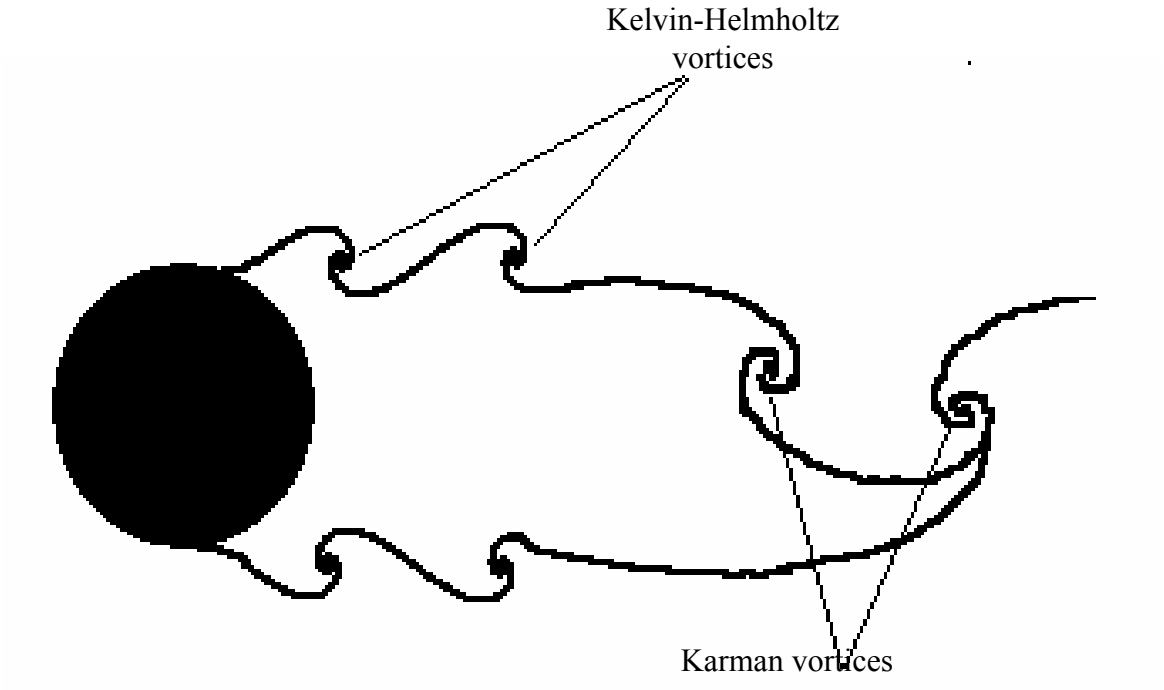


Figure 1.5. The Kelvin-Helmholtz (secondary) vortices and the Karman vortices from circular cylinder.

Kelvin-Helmholtz vortices in the shear layer are an essential feature of the transition from a laminar to turbulent state. As a consequence of this transition process, the first Karman vortex formed from the cylinder at Re_D=5000 is essentially turbulent. A Karman vortex from circular cylinder is shown in Figure 1.5.

2. LITERATURE SURVEY

2.1. Flow structure around spheres

The flow around a sphere has attracted a renewed interest in recent years. Although the sphere is the simplest geometry representing a three-dimensional bluff body, a number of applications exist, ranging from the aerodynamics of sports balls to particle-laden or multi-phase flows. A number of studies have examined the flow field around sphere and the aerodynamic force in a uniform flow. Flow over a sphere is a typical bluff-body flow with many engineering applications as mentioned in the literature. However, Ozgoren et all (2009) indicated that it has not been studied in depth as compared to the flow over a circular cylinder because of the difficulties in the experimental set-up as well as in the computational approach for studying flow over a sphere in the past.

Achenback(1972) observed the flow around a sphere for the case of smooth surface of the sphere within the range of Re=5x104 – 6x104. Total drag coefficient, C_d local static pressure and surface drag coefficient, C_d were measured at 0.45 % turbulence intensity and results were compared with the literature. He explained the flow separation occurred at transition of laminar boundary layer to turbulent boundary layer and dependency of drag coefficient , F_d to Reynolds number, Re.

Achenback(1974) studied the flow around unsteady flow structure around sphere and vortex shedding from sphere for different Reynolds numbers up to Re=400. He confirmed that Strouhal number, St is a function of Reynolds number, Re with performing experiments in water. He showed that there was a phase difference between vortex shedding from spheres and recorded signals which were measured different points along arc which had an angle of 75 deg with streamwise direction simultaneously. He emphasized the recirculation behind the sphere and vortex separation and he tried to explain these events.

Taneda (1978) performed experimental studies on the wake configuration of the sphere by means of the surface oil-flow method, the smoke method and the tuft-grid method in a wind tunnel of Reynolds numbers ranging from 10^4 to 10^6. It is

found that the wake performs a progressive wave motions at Reynolds number between Re=10^4 and Re=3.8 x 10^3, and that it forms a pair of streamwise line vortices at Reynolds numbers between Re=3.6 x 10^5 and Re=10^6.

Werle (1980) visualized sphere wake in a water tunnel using dye at Re = $1.6x10^4$ to see the recirculating flow behind the sphere and the shear layer instability of a ring-shaped vortex.

Yutaka et al. (1982) investigated the dynamic interaction between two spheres to obtain fundamental information about two phase flow. Spheres were arranged in side by side and tandem positions for Re $\leq$ 1000. The flow structure around spheres was observed by using concentrated milk and results were tried to explain.

Tsuji et all (1982) investigated the dynamic interaction influence of flow between two spheres to obtain the fundamental information about two phase flow. Spheres arranged side by side and tandem for lower values of Re=1000. The flow structure behind spheres was observed using increased density milk and results were evaluated. They measured drag force, F_D on the sphere using pendulum method which was developed to detect small drag at the intermediate Reynolds numbers. They stated that although the influence is limited and drag increases with small range compared with the case of two spheres aligned streamwise, Drag is increased due to an increase in local Reynolds number caused by nozzel effect when two spheres arranged in order side by side. They tried to interpret dynamic interaction between other type of sphere arrangement and flow.

Mehta (1985) performed research work about aerodynamics of sport balls (baseball, tennis, cricket). He investigated the path of these balls in air and Magnus effect which is the effect on the flow structure around sphere when it rotates about its own axis. Due to the Magnus effect the separation converted from symmetric form to asymmetric one. However, he compared the effect of different surface properties of used ball in his study.

Wei et al. (1988) conducted experiments in wind tunnel about dynamic loading due to vortices around stationary volleyball ball. They visualized the flow structure passed the ball and measured the aerodynamic loads by using strain gage balance system. They determined the separation around sphere by hot-film method.

Their results showed that separation region can be changed under the motion of the varied tail vortex system. Drag and fluctuation of traverse loads also show that the flow characteristics are proportional to averaged drag independent from the position of sewing line of the ball according to uniform flow direction.

Kim and Durbin (1988) observed frequencies of vortices in the sphere wake and the drag increment by acoustic excitation. They found that two dominant modes of unsteadiness existed in the sphere wake and excitation reduced the mean base pressure behind the sphere and increased the drag.

Sakamoto and Haniu (1990) experimentally observed vortex shedding from spheres in a uniform flow. They used low speed wind tunnel to measure the vortex shedding frequency. Flow-visualization experiments were carried out in a water channel. They found that the variation of Strouhal number, St with the Reynolds number, number Re can be classified into four regions, and the relationship between the Strouhal number, St and the configuration of the wake in each region is clarified. When a Reynolds number, Re exceeds about 300, the hairpin-shaped vortices begin to be periodically shed with regularity in its strength and frequency, forming laminar vortices until a Reynolds number, Re is about 800. When a Reynolds number, Re exceeds about 800, the hairpin-shaped vortices begin to change from laminar to turbulent vortices with alternate fluctuations, this pattern of vortex shedding continues as far as the region of $Re=3.7x10^5$,wich is called the upper critical Reynolds number. When a Reynolds number, Re exceeds 800, the vortex tubes begin to be periodically shed covering the vortex formation region, in accordance with the pulsation of the vortex sheet separated from the surface of the sphere. At the Reynolds number, Re ranging from $8x10^2$ to $1.5x10^4$, the higher and lower frequency modes of the Strouhal number, St which are caused by the periodic fluctuation in the vortex tube formed by the pulsation of the vortex sheet separated from the surface of the sphere and in the turbulent wake with progressive wave motion respectively, are coexisted.

Kim et al.(1990) showed that the flow structure passed through the sphere was unsteady within the range of $120 \leq Re \leq 300$ experimentally. They stated that consequence of this event, symmetrical vortex shedding causes asymmetric and time-

dependent flow structure downstream of the sphere in high Reynolds numbers. They investigated later the linear stability of symmetric base flow by using spectral analysis of computational flow dynamics. They evaluated their computational results for critical Reynolds number, Re and compared with the previous experimental results of the Strouhal number, St.

Wu and Faeth (1993) studied the wake region of stationary spheres in a channel filled with water and glycerin mixture in the range of $30<Re<4000$. The flow region was visualized with a technique which is based on the illumination of the dye tracks and velocities on the streamwise direction were determined with a lased based measurement. Beyond the sphere, in the recirculating region, symmetrical and steady flow for $Re<200$, asymmetric and steady flow in the range of Reynolds number $200 \leq Re \leq 280$ and unsteady with vortex shedding for $Re \geq 280$ were observed.

Wu and Faeth (1994) investigated the flow structure of wake flow of sphere within the range of $135<Re<1560$ when the turbulence intensity is 4%. They stated that an increase in the turbulent viscosity due to the turbulence contributing maintained the averaged velocities in streamwise direction laminar. They also stated that the effect of turbulence viscosity was independent from measuring point in the wake region and length scale. They devided the range of the Reynolds number into three ranges as low, transition and high ($300<Re<610$) and they also stated that an increase in turbulent friction is the highest in the transition region.

Zhu et al. (1994) measured the drag force representing the rare solid gas flow for different gap ratios of tandem spheres within the range of $20<Re<130$ in their computational and experimental studies. The drag resistance of rear sphere decreased with decreasing the gap ratio. It was found that due to the interaction between spheres, the wake region of the front sphere decreased. The Reynolds number effects not only ratio of drag resistance but also the length of wake region and the wake region of front sphere decreases with increasing the Reynolds number.

Barker et al. (1997) observed the near wake region of the spherical bluff body with 2D Particle Image Velocimetry (PIV). They determined the velocity and vorticity fields for Re= 202 and 403. The vortex shedding occurs for Re=403 and does not occur for Re=202 presenting the video recording and they supported their

results by taking streak photos and measurement with hot wire anemometer. Consequently, they proposed to make detailed research for their qualitative measurements.

Ryu and Lee (1997) made analytical study to observe effect of vortex corruption due to the interaction between recirculation and sphere in three dimensional incompressible flow. They calculated the instantaneous forces by using Bermoulli equations.

Williamson and Govardhan (1997) mounted a sphere in channel with uniform flow flexibly. They declared that the sphere vibrated due to the effects of uniform flow in streamwise direction and wake region in the upstream flow direction and moves in a range of twice of sphere diameter. By this way, experimental results of both vibrating and stationary sphere could be compared. It was observed that drag force increases in the case of free vibration. Natural frequency on the streamwise direction and perpendicular to streamwise direction were not equal, although the frequency on the streamwise direction was equal to frequency of the sphere the frequency on the other side was twice of the frequency of the sphere experimentally. Results showed that response magnitude of structure to very small damps could be supposed as the function of the Strouhal number, St and only mass ratio and length of the wake region effectted the natural frequency.

Alassar and Badr (1997) calculated the viscose flow problem around oscillating sphere by using Legendre series and functions of Navier-Stokes equations with asymmetric flow assumed the asymmetric flow in incompressible fluids. By investigation of effect of the Strıuhal number, St and Reynolds number on the flow characteristics, they compared these results with potential flow solutions. They presented the surface vortex and pressure distribution results of drag coefficient with separation length.

Numez and Voigth (1999) made trial measurements consist of the wake region of the sphere within the range of Reynolds number $100<Re<700$ to analyze dynamics of vortex structure and corresponding structures by using a three dimensional laser based Particle Image Velocimetry. Their study provides quantitative and qualitative results to determine the vortex circulation length and its dynamic characteristics.

Johnson and Patel (1999) computed the flow structure in the case of both steady and unsteady, incompressible, viscose flow up to Re=300 and they compared their results with dye injection experiments. Their computational studies focused on the steady asymmetric region, steady symmetric region and unsteady region and also transition region taken place between these regions. They emphasized that the firs separation was taken place at Re=20 and this result was agreed with previous studies. They determined that unsteadiness of the flow was increased.

Chen and Lu (1999) studied the drag and the fluid mechanic characteristics of two and three interactive spheres which were aligned side by side, streamwise and in a reversed L manner at a Reynolds number less then 200. They concluded that the size of the wake region of the trailing sphere was greatly reduced under the influence of the leading sphere when two spheres were aligned streamwise direction. The influence of the wake of the leading sphere and the existence of a liquid nearly-stagnant region located at the gap between two tandem spheres placed in streamwise direction caused a substantional reduction in the total drag. Drag was increased due to an increased in local Reynolds numbers caused by the nozzle effect when two spheres was arranged in order side by side. All the same, the influence was limited and the drag increase was minor compared with the case of two spheres aligned in streamwise direction. When three spheres were aligned side by side, for the center sphere, the wake size was enlarged and the vortex centers of wake were laterally shifted away from the rod as the flow becomed three dimensional. Finally, they stated that the drag and wake of spheres were influenced by the arrangement of spheres in the flow.

Chen and Wu (2000) studied the influences of a surrounding sphere of different size, located at various distances and angles, on the drag and the flow characteristics of a testing sphere at the particular Reynolds number less than Re=200 by using the LDA system. They concluded that the influences of inter-particle distance and the size of the surrounding sphere on the drag were more prominent when the surrounding sphere was placed upstream of the testing sphere and the interactive influence on the drag was moderated with an increase in the

Reynolds number. The size effect, especially at a small inter-particle distance became increasingly noticeable as the Reynolds number was increased.

Thompson et all (2001) studied the kinematics and dynamics of the sphere wake transition for only the first two transitions at Re =212 (a regular transition) and at Re =272 (Hopf bifurcation). They found that both the regular transition of Re =212 and the Hopf bifurcation at Re =272 were supercritical, as determined from the evolution of the cubic coefficients of the Londau model which contributed the validation of computational results.

Hadzic et al (2002) observed the flow around a sphere by using both experimental (hot-wire and laser-dopler anemometry technique) and numerical method (LES) at subcritical Reynolds number of 50000. They compared experimental and numerical results. It was found that LES results were in reasonable agreement with the experimental results.

Constantinescu and Squires (2003) simulated the flow over a sphere in the Subcritical regime in which the boundary layers at separation were laminar using LES(Large Eddy Simulation) and DES(Detached Eddy Simulation) for prediction of flow around a sphere at Re=10000. They found that both DES and LES represent same result for prediction of the primary Reynolds shear stress, turbulent kinetic energy, edy viscosity and turbulent distribution. DES and LES provide closure predictions of the wake structure, large-scale vortex shedding and Strouhal number, St associated with the low Frequency mode in the wake more over, both models successfully resolve the formation of the vortex tubes in the detached shear layers along with the value of the Strouhal number, St associated with the high Frequency instability mode.

Constantinescu and Squires (2004) investigated flow field around a sphere as a numerically at the supercritical (laminar separation) and supercritical (turbulent separation) regimes in the range of Reynolds numbers, Re (10^4-10^6). Their attention focused on predictions of the pressure distribution, skin friction and drag as well as to understanding the variation in the near wake region and vortex dynamics with the Reynolds number. For both the subcritical and supercritical solutions, the agreement with experimental measurements for the mean drag and pressure distribution over the

sphere is adequate; differences in skin friction exist due to the simplistic treatment of the attached boundary layers in the computations. Improved agreement in the skin-friction distribution was obtained for the supercritical flows in which boundary layer transition was fixed at the position observed in experiments conducted at same Reynolds numbers. For the subcritical flows the Strouhal number, St, associated with the large-scale shedding was predicted at St~0.195 along with a higher frequency component associated with the development of the Kelvin–Helmholtz instabilities in the detached shear layers.

Schouveiler et al. (2004) examined the wake of two stationary spheres the wakes of two stationary spheres placed side by side in a uniform flow for Reynolds numbers between Re=200 and Re=350, have revealed the existence of different regimes of interaction, as a function of the spheres' separation distance from h/d=1 to h/d>3(h= distance between the sphere centers). They focused on the important topic which explains the influence of the sphere arranged on the wake interaction of the spheres. When increasing separation distance from one diameter , they act as a single body, two coupled wakes with out-of-phase shedding, two wakes with in-phase shedding (mainly in the experiments), and independent shedding from both spheres. The critical Reynolds number for the onset of shedding decreases rapidly with decreasing separation distance, once the latter drops below two sphere diameters. At a given Reynolds number, the wake frequency varies smoothly with separation distance in the range where two separate wakes can be identified. Their study shows that the degree of interaction of two wakes depends mainly on the separation distance between the bodies.

Jeon et.al (2004) conducted experiments to be able to decrease the drag force of sphere by making blowing and suction from the gap on the surface of the sphere at $Re=10^5$. They kept the frequency of the blowing and suction one-third of natural frequency of vortex. By this way, they found that the drag force was decreased to 50 % of the normal case. At frequencies below than this value, they stated that there was no considerable decrease in the drag force. They also stated that reverse flow behind the sphere was decreased in size and there was a change in drag coefficient like golf ball.

Giwoong et al. (2006) investigated the flow structure over a sphere by using the Large Eddy Simulation (LES) technique for the values of Reynolds number of Re=3700 and 10000. They concluded that the flow right behind the sphere contained only a few vortices. On the other hand, at Re=104, the shear-layer instability occurred right behind the sphere in the form of vortex rings, and the flow becomes turbulent in the near wake. Therefore, at Re=104, the size of the recirculation region is smaller and the wake recovers more quickly than at Re=3700.

Yun et al. (2006) investigated the shear layer instability in the wake region of sphere and rotation of the vortex structure by using the LES technique. However, they had problems about confirmation of these computational results. They said that they needed experimental data to confirm their results. Because, they worked on the immediately lower values of subcritical Reynolds number as Re= 10000.

Resent years, Yang and Lee (2008) investigated the vortex structure of recirculation region immediately behind a sphere only for Re=11000 by using the PIV technique. They stated that vortices due to the sphere have fluctuating form They also stated that the turbulence structures are similar to the quantitative experimental data and these results can contribute the validation of computational results.

2.2. Flow structure around cylinders

Amongst the various investigations on two-dimensional bluff body flows, the circular cylinder geometry has received the most attention both because of the complex flow features it offers and practical relevance. Relevant investigations for cylinder using measurement techniques such as dye visualization, point-wise hot-wire, laser Doppler velocimetry (LDV), Particle İmage Velocimetry (PIV) for various Reynolds numbers summarized as follows.

Lin and Rockwell (1995) investigated flow structures around cylinder quantitatively. They employed the film based particle image velocimetry technique at three values of Re = 1000, 5000 and 10,000 for the Cylinder to obtain instantaneous flow patterns. They stated that representations of velocity, vorticity and streamlines showed a decrease in vortex formation length with increasing Reynolds number.

Balachandar et al. (1997) applied direct numerical simulations at the lower Re number and large-eddy simulation at the higher Reynolds number over several different 2-D bluff bodies for $250 \leq Re \leq 140{,}000$. They also performed experiments to support their numerical solutions. Properties of the time- and phase-averaged mean wake recirculation region in the separated flows were investigated in order to explain the distribution of Reynolds stress and pressure in relation to the mean wake recirculation region (wake bubble) and vortex formation length.

Noca et al. (1998) accomplished an investigation on the concept of vortex formation length in the wake of the cylinder by measuring the location of some easily identifiable flow features for $300<Re<4000$ and different aspect ratios.

Akıllı et al. (2004) experimentally investigated the flow around two and three side-by-side circular cylinders of equal diameter (Re_D=5000) in shallow water using the particle image Velocimetry (PIV) technique, over a transverse gap ratio in the range of G/D= 1.0-3.0 with an increment of 0.25 For the two side-by-side cylinder case, They found that the flow structure behind the cylinders is asymmetrical at small gap ratios as a result of jet-like flow between the cylinders. The jet-like flow tends to deflect toward the narrow wake region that has a higher vortex shedding frequency. In the case of three cylinders, they observed both an asymmetrical flow structure at small gap ratio (G/D= 1.25) and a symmetrical flow structure at intermediate gap r

atios ($1.5<G/D<2.0$). He also observed bistable wake regions for the asymmetrical.

Ozgoren (2006) examined flow characteristics in the downstream of single circular, sharp-edged square and 45^o orientated square cylinder in a uniform flow using DPIV. He investigated the generation of vortical structures of the near-wake region for $550 \leq Re \leq 3400$ by using PIV. Strouhal numbers, as well as the wake patterns, are functions of the cross-section of the cylinders and Reynolds numbers. Strouhal numbers for the circular, sharp-edged square and 45^o orientated square cylinder are found to be around 0.21, 0.13, and 0.17, respectively.

Sahin et al. (2007) concentrated on the flow structure around the base of the vertical cylinder mounted on a flat plate for the Reynolds number of Re = 4000 by using PIV technique. They made measurement in four different measuring planes

across the boundary layer in order to observe the effect of three-dimensional junction flows arising from the base of the cylinder on the flow structures downstream of the cylinder in the boundary layer. They pointed out that the structure of turbulent flow, the size of the wake flow region, the location of singular points, the peak values of turbulent quantities such as Reynolds stress correlations, $<u'v'/U_\infty^2>$, and the root mean square of the velocity components, $<u_{rms}/U_\infty>$ and $<v_{rms}/U_\infty>$, vary as a function of elevation of laser sheet location (measurement station) in the region of the boundary layer.

Sahin and Ozturk (2009) has studied on the characteristics of the flow field in the base of the vertical cylinder mounted on a base plate investigated experimentally both in plan-view and side-view planes plate in deep water via PIV measurement. They stated that horseshoe vortex systems immerging from the upstream base of the cylinder wrap the cylinder and travel in the direction of the main flow along the shear layers. During the immigration of these swirls in streamwise direction and horseshoe vortices flap in lateral direction giving rise to the entrainment between core and wake-flow regions and stimulating the scour to a higher level.

Ünal and Rockwell (1988) examined the separated shear layer over the range of Reynolds number $440 \leq Re_d \leq 5040$ using combinations of hydrogen-bubble and dye injection visualization, along with hot-film measurements. They observed the onset the Kelvin-Helmholtz vortices are associated with a decrease of the formation length of the large-scale Karman vortices.

Bloor (1964) addressed the three-dimensional aspects of this transition process using point velocity measurements obtained from hot-wire anemometry. She observed that the region of transition to turbulence moves upstream towards the cylinder with increasing Reynolds number.

Gerrard (1978) asserts that there is an interaction between the formation of the large-scale Karman vortices and transition waves in the Reynolds number range from 350-2000. His flow visualization photos show that in some cases the transition wave and the roll-up occur in such a fashion that the ant-symmetrical formation of the large-scale Karman vortices is not altered. On the other hand, other photos suggest

that the symmetrical formation of the transition waves (i.e., Kelvin-Helmholtz vortices) can actually inhibit the onset of the Karman vortices.

Wei and Smith (1986) addressed such waves, manifested in the form of discrete Kelvin-Helmholtz vortices, over the range of Reynolds number extending from Re_d=1200 to 11000 using both hydrogen-bubble and flow visualization hot-wire anemometry. They pointed out that the Kelvin-Helmholtz or" secondary" vortices are detected in the near wake of the cylinder are identical to the transition waves reported by Bloor (1964), because both phenomena occur immediately downstream of the separation point and appear to have similar unsteady characteristics. They described the origin of the Kelvin-Helmholtz or secondary vortices as instability of the free shear layer separating from the surfaces of the cylinder.

3. MATERIAL and METHOD

3.1 Experimental Arrangement

Increasing technological developments, especially in electric and electronic engineering, provide new measuring techniques. All measurement techniques have some advantages and disadvantages associated with the specific method. It is increasingly important not only to measure the mean values at a point in space, but also to measure and characterize turbulent and instantaneous values in the investigated flow field. Particle Image Velocimetry, PIV, is a non-intrusive technique used to measure two dimensional instantaneous velocity vector fields.

3.1.1 Water Channel System

Both PIV and dye visualization experiments were performed in a large-scale water channel located in the Fluid Mechanics Laboratory at Cukurova University. The water channel (see Figure 3.1 a and 3.1 b) test section which has the following dimensions: a length of 8000 mm, width of 1000 mm, and a depth of 750 mm was constructed of transparent Plexiglas with upstream and downstream fiberglass reservoirs. The water channel also has honeycomb screen arrangement, which is located at the entrance of contraction. These reservoirs and honeycomb screen arrangements are used to maintain the turbulence intensity in the section below 0.5 %. All instruments and set up are placed in the test section from the top of the test chamber. The width of the channel is large enough to avoid the effect of the side walls on the observed flow field. The flow is produced by a 15 cm (6”) diameter radial water pump driven by a 15 kW electric motor with a variable speed controller was used to create the mean flow in the test section. The water channel is filled with water nominal depth of 450 mm. Flow speed vary linearly according to free stream velocity ranging from 0 to 236 mm/sec and calibrated for a test section water depth of 450 mm for all experiments. The water channel facility uses several devices to reduce flow disturbances in the test section. Besides the a honeycomb section and a two-to-one channel contraction, a horizontal perforated cylinder pipe in the settling

chamber allows the water coming from the pump to be dispersed along its entire depth. The cylinder is wrapped with another pipe to pressurize the fluid in the cylinder and thus even out its exit velocity. A plunger is located inside the perforated cylinder to absorb the vortical momentum from the inrushing water. The temperature of the Fluid Mechanics Laboratory was kept constant of 22^{o}C through out the experiments.

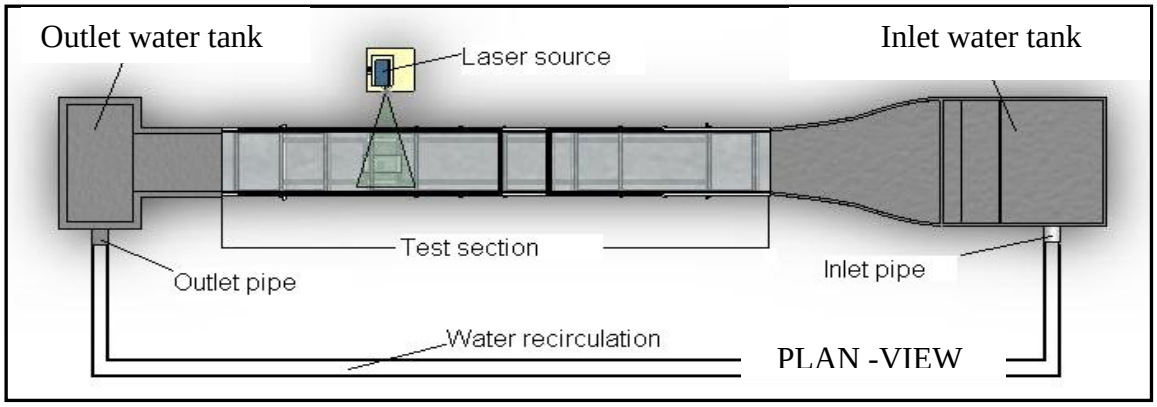


Figure3.1.a. Representation of Plan-view setup

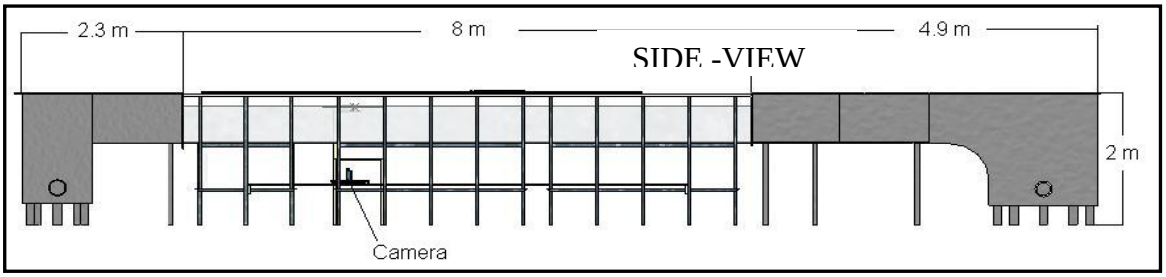


Figure: 3.1.b. Representation of Side-view setup

3.2. Measurement Techniques

3.2.1. Flow Visualization Techniques

The dye-injection flow visualization experiments were conducted in a large-scale water channel. The cylinder models were constructed of Plexiglas (D=50 mm) material. Dye came from a container, which were located 75 cm above the free surface of the water channel and went through the plastic tube. Dye visualization technique aims to visualize flow by spreading some amount of Rhodamine type dye that shines under the laser light exposure in the desired flow field. The dye visualization technique offers no numerical analysis or data to use, but shows a brief demonstration of the flow that gives an idea about the flow field and the vortices. The video camera which was SONY HD-SR1 was used to capture the instantaneous video images of the vortex flow structures. The images were analyzed with frame grabber. Digitized images were enhanced for analysis using Adobe Photoshop software. A brief demonstration of the dye visualization setup is shown in figure 3.2.

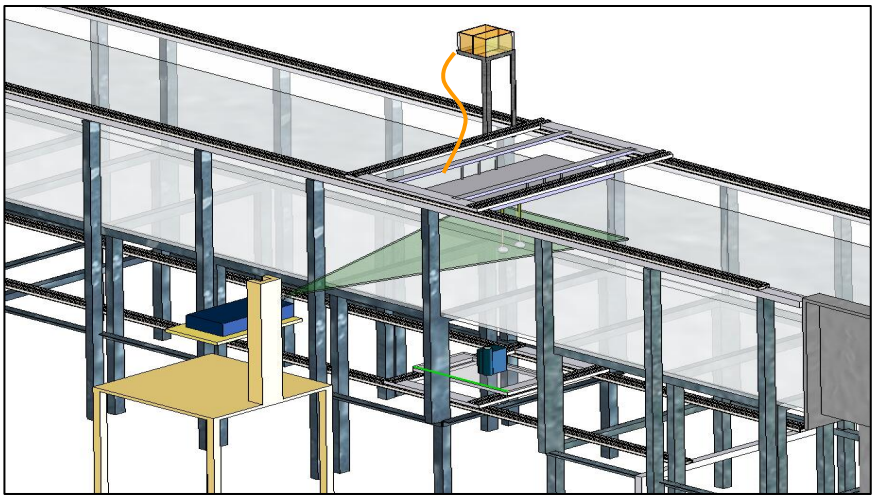


Figure 3.2. Overview of dye visualization technique around side-by-side sphere

3.2.2. Particle Image Velocimetry (PIV) Techniques

The Particle Image Velocimetry (PIV) technique, which allows instantaneous, non-intrusive and quantitative measurement of two dimensional flow field is an important achievement and a well established technique in many areas of modern experimental fluid mechanic applications. PIV also provides sufficient spatial resolution such that an instantaneous vorticity field may also be calculated. PIV has been used to measure velocity vector fields from slow flows to supersonic flows during past two decades (Adrian, 1991; Raffel and Kompenhans, 1995; Raffel, et al, 1998).The technique involves seeding the flow field, illuminating the region under investigation and capturing two images of that region in rapid succession. From the displacement of the tracer particles, provided that the time interval between image captures is known, a velocity vector map can be calculated in the flow field.

The theory of PIV was introduced by Adrian (1988) in the late 1980s with the first experimental implementations following shortly afterwards (Kean et al. 1990 and Kean et al. 1991). At the stage, due to hardware limitations, a single photographic frame was multiply exposed and analysed using an auto-correlation technique. However, improved speed of photographic recording soon allowed images to be captured on separate frames for analysis by cross-correlation (Kean et al. 1992).

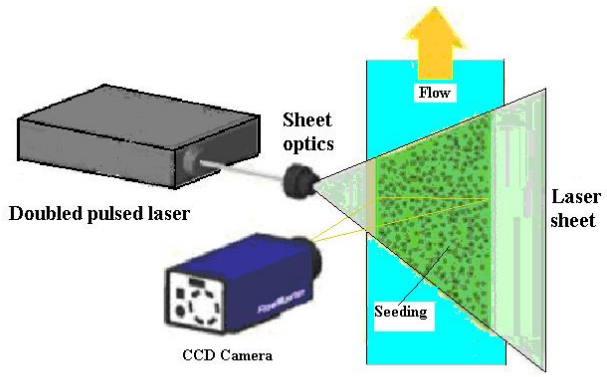


Figure 3.3. A typical PIV experimental set-up (McLean, 2007)

The introduction of digital camera technology to the PIV technique enabled the direct recording of particle images (Willert et al. 1991), at the expense of reduced resolution, resulting in the development of digital PIV Westerweel, 1997). As well as these hardware advances, many new algorithms have been developed in the last decade, increasing the accuracy and speed of PIV analysis. One key advantage of the PIV technique over other conventional techniques such as LDV or hotwire anemometry is ability to obtain instantaneous flow-field information which is important for probing the structure of turbulent flow fields without disturbing the flow structure (Westerweel et al. 1996; Meinhart and Adrian 1995). A brief demonstration of the PIV visualization setup is shown in figure 3.4.

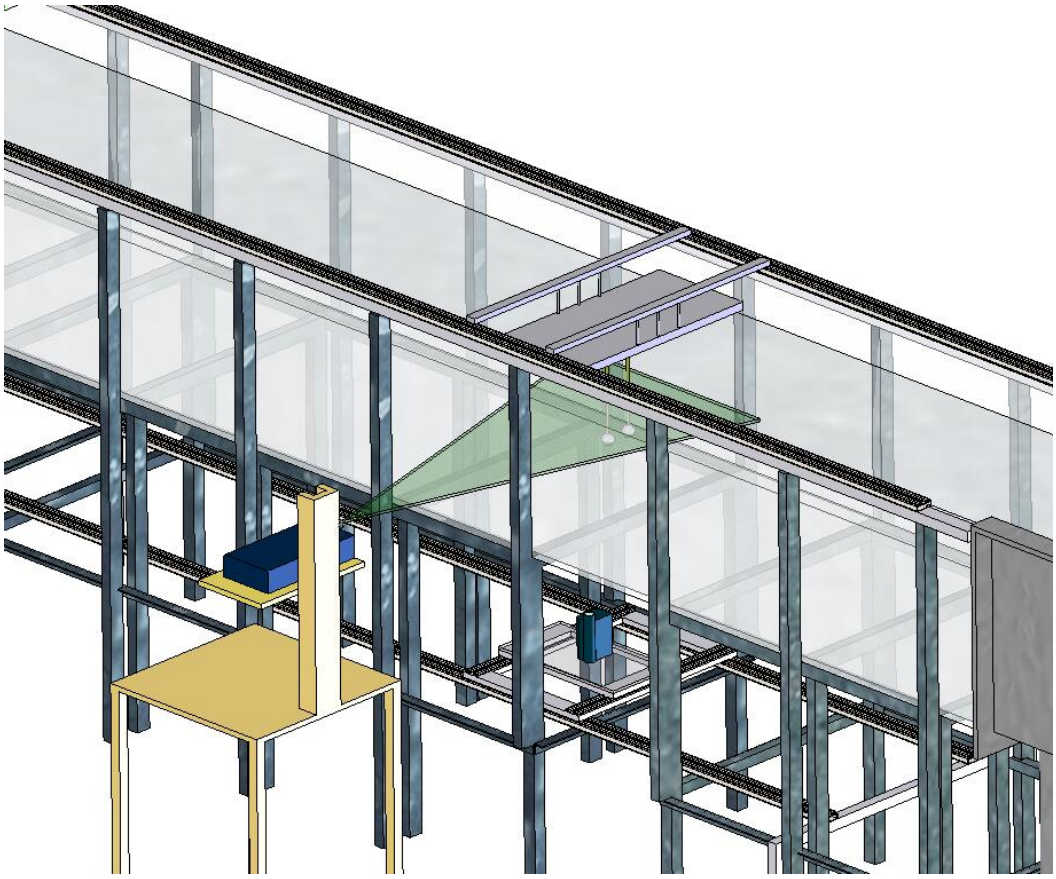


Figure 3.4 Overview of (PIV) visualization technique around side-by-side spher

3.2.2.1. Principles of PIV

Particle Image Velocimetry (PIV) is a measurement technique for obtaining instantaneous whole field velocities. It is based on the well known equation

Speed =Distance / Time

In the PIV technique the property actually measured is the distance between two images of particles that travels in the flow field within a known time interval. These particles are added to the flow and known as seeding. Different types of seeding particle are used depending on the nature of the flow for PIV experiments. The type of seeding particle is chosen to follow the flow, and in order to detect their movement, an area of the flow field is illuminated by a laser light-sheet. The light-sheet, which is generated by a laser and a system of optical components, is not continuous/permanent, but pulsed to produce a stroboscopic effect, freezing the movement of the seeding particles. The time between the light pulses is the denominator in the equation above. To detect the position of the illuminated seeding particles, a CCD-camera (CCD = Charge Coupled Device) is positioned at right angles to the laser light-sheet, and particle positions will appear as light specks on a dark background on each camera frame. The pulsing light-sheet and the camera are synchronized so that particle positions at the instant of light pulse number 1 are registered on frame 1 of the camera, and particle positions from pulse number 2 are on frame 2. (Older generations of CCD cameras couldn't switch frames fast enough, so both the first and the second pulse of the light sheet was recorded on the same camera frame).

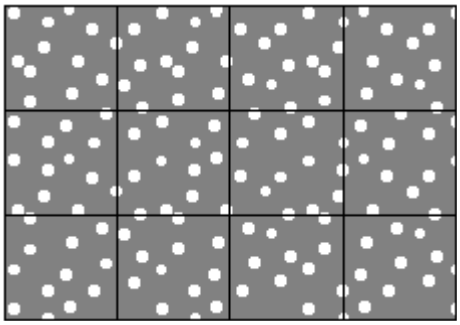


Figure 3.5 Interrogation areas

The camera images are divided into square regions called interrogation areas or interrogation regions, and for each of these interrogation areas the image from the first and the second pulse of the light-sheet are correlated to produce an average particle displacement vector. Doing the same process for all interrogation regions produce a vector map of average particle displacements. Dividing with the known time between the two images captured, the displacement vectors are converted into a map of so-called raw velocity vectors. Then validation algorithms can be applied to the raw vector maps, so that outliers, the term for erroneous vectors, can be detected and removed. In the FlowMap PIV system, for reasons of experimental reproducibility, the raw vector map is archived and a new validated vector map is output, and further analysis can produce streamlines, vorticity and so on.

From the basic principles the following main topics of PIV emerge:

• Seeding
• Illumination
• Cameras
• Synchronization
• Correlation
• Validation and further analysis

3.2.2.2. Image Acquisition

Figure 3.6 shows a typical experimental arrangement for carrying out PIV measurements. Tracer particles added to the flow under investigation are illuminated by laser sheet and images of the illuminated flow field are captured and stored for later analysis.



Figure 3.6. Schematic of experimental apparatus and digital PIV instrumentation

3.2.2.3. Seeding

In a few case it is possible to make sure measurement using what is naturally present as impurities in the fluid, but usually, successful seeding can require considerable effort and ingenuity.

Factors that have to be considered are:

- Flow medium (air/water)
- Volume to be seeded

- Flow velocity
- Light scattering
- Particle image size Safety considerations (ingestion, risk of explosion)

Cost

Particle size and density, and fluid density and viscosity determine the effects of buoyancy and inertia. Exact neutral buoyancy is difficult to achieve, but particles must remain suspended throughout an experiment.

The light scattered from the particles is only a fractions of the light introduced into the flow. This scattered light, only that within the solid angle defined by the lens aperture of the imaging system will be collected to form an image. Conventional PIV set-ups record side-scattered light, which can be orders of magnitude weaker than forward-scattered light. The size and material of the seed particles can affect scattering efficiency and small particles also affect particle image intensity. The average particle image should exceed the fog level of photographic emulsions or the noise level of solid-state detectors.

3.2.2.4. Illumination

In PIV, the displacement field is determined as average displacements within so-called interrogation areas of the image plane. A typical size of these interrogation windows is 32x32 pixels, which means that a gets about 7300 vectors from an image with a resolution of 1600×1186 pixels. For single exposed images, the displacement is determined by forming an adaptive cross-correlation of corresponding interrogation areas in the first and second images. The location of the highest correlation peak in the correlation plane corresponds to the most likely average particle displacement in the interrogation area. Sub-pixel accuracy of the displacement is obtained by fitting a Gaussian distribution to the correlation peak, and finding the exact peak location. Since the cross-correlation method uses all information within the interrogation area for finding the displacement, the method is

robust and often provides reasonable results even for non-ideal conditions. Another advantage is that the displacement field is obtained on a regular grid.

For the illumination, it is preferable to use a laser, since the laser beam is easy to form into a sheet by a cylindrical lens. A pulsed laser is to prefer, since one obtains a high light energy during a very short time interval (typically 5 ns for a YAG-laser), which means that the particle images will be practically frozen even for high velocities (> 100 m/s). The repetition rate of a YAG-laser is typically 10-30 Hz, which is too low except for very low velocities (< 1 cm/s). One therefore needs two lasers to get full freedom in terms of time separation between the pulses. Special PIV YAG-lasers are available that combine two laser cavities with a common beam outlet.

3.2.2.5. Cameras (Image Capturing)

To be able to acquire two single exposed images with a time separation of the order of microseconds, one uses a so-called full-frame interline transfer progressive scan CCD camera, also called a cross-correlation CCD-camera. The basic idea is that the image exposed by the first laser pulse is transferred very rapidly to light-hidden areas on the CCD-chip. This is done on a pixel-by-pixel basis, i.e. each pixel has its own storage site in immediate vicinity of the light sensitive pixel area. After the second exposure, both images are transferred to the computer. Since a lot of data has to be transferred, it is only possible to take a few double-images per second. The temporal resolution of the flow is thus in general very poor with this technique.

A very important issue for obtaining accurate PIV measurements is the appropriate seeding of the flow with tracer particles. To closely follow the flow the particles should be as small as possible, but on the other hand they may not be too small, because then very small particles will not scatter enough light, and hence produce too weak images.

3.2.2.6. Correlation (Image Evaluation)

Since the introduction of the first PIV image evaluation methods, alternative analysis algorithms have been developed as well as error correction and post-processing procedures designed to improve speed and accuracy of the PIV method. However, the classical PIV analysis method is still the most frequently used and forms the basis of many other algorithms. (Figure3.7).

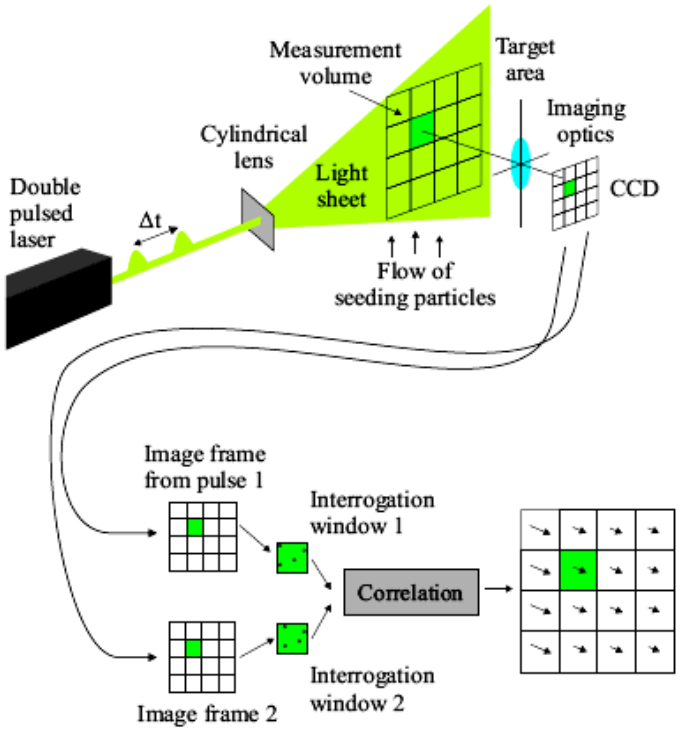


Figure 3.7. PIV overview (Schiwietz, T., Westermann, R., 2004)

The heart of the PIV analysis is the correlation of regions of the input images (known as interrogation areas) with each other to determine the displacement vector of the flow in that part. Knowing the time interval between the image captures enables a velocity vector to be calculated from the displacement vector. The correlation technique can be used for a single frame multiple exposed (auto-correlation) or multiple frames singly exposed (cross-correlation). To speed up the convolution process, correlation of each pair of interrogation areas is carried out in

Fourier space. After interrogating the images in this way and generating the vector map, post-processing is carried out to validate the data and to improve the vector map resolution and accuracy. Using this vector map, vorticity and Reynolds stress contours and streamline topology can be obtained.

3.2.2.7. Validation and further analysis (Image Post-Processing)

Images were received from CCD camera that has resolution 1,600 ×11.186 pixel at a rate of 15 frames per second. The time delay changes from 1.7 ms and 4.5 ms between frames depending on the flow conditions and camera location. Digital image was analyzed using FLOWMAP software. The image was recorded on a CDD array. A frame grabber in the computer read the camera image from CCD camera and stored it as the digital image file format (TIFF) in the RAM. This digital image was processed and analyzed using the FLOWMAP software. During each continuous run, a total 390 images were taken. In order to determine the velocity field, a cross-correlation technique, with 32×32-interrogation window, was employed, with an overlap of % 50.

The resulting vector field obtained from FLOWMAP software and the corresponding boundaries of objects were then viewed using program V3 to determine incorrect vectors from interrogation. These types of vectors can result when an incorrect particle correlation is made near boundaries or within shadow regions, when the particle images are too widely spaced for interrogation window side specified, pr the power of laser sheet is poor.

Vector validation software called CLEANVEC was used to remove incorrect vectors.

The software CLEANVEC contains four statistical filters designed for incorrect vectors removal:

- Absolute range filter
- RMS tolerance filter
- Magnitude difference filter
- Quality filter

Three of these four filters were used for the purposes of eliminating incorrect vectors. Here the quality filter requires a correlated data, which are supposed to be done by interrogation and this data, was not provided by this software.

In the absolute range filter, all streamwise and spanwise velocity components that lie outside of given range were removed. With this filtering method, one can identify a moving reference frame in order to save real vectors that are numerically specified and eliminated incorrect vectors on the main frame. Although very trivial, this filter might be very useful in removing the most tedious incorrect vectors, and hence improves the performance of the other filtering tools.

The RMS tolerance filter removes incorrect vectors those lay outside of given range. This filter must be applied to a velocity field in a reference frame moving with the mean velocity components in both directions, since it is involved with the fluctuating components only.

Finally, the magnitude difference tool removes unnecessary vectors based on the difference in magnitude between a vector and its neighborhood median. This is the local-median test defined by Westerweel (1994). This filter is the most effective among the available filters, as indicate by Westerweel (1994). However, it should be handled carefully, because it may lead to an excessive vector in a certain type of flows.

4. RESULTS and DISCUSSUION

4.1. Experimental investigation of flow structure around a sphere and Cylinder via flow visualization

4.1.1 Introduction

Symmetric objects defined in two dimensions such as cylinder create three dimensional unsteady flows. There dimensional flows create unsteady, more complex kinematic and vortical interactions compared with two dimensional flows. When the flow and body are three dimensional, the flow around three dimensional bodies could not be determined by both experimentally and computational methods (commercial programs). Therefore, more experimental results are needed to develop new methods or improve existing methods. Periodic vortex shedding patterns and fluctuating velocity fields behind the bluff bodies can cause structural damage as a result of periodic surface loading, acoustic noise and drag forces. Most work has been done on the flow passing a circular cylinder rather than a sphere. Even though their near wake flow structures are expected to be topologically similar to one another, the reasons for flow separation and wake structure on the surfaces are different. Therefore, these two bluff bodies mutually compared in the present research.

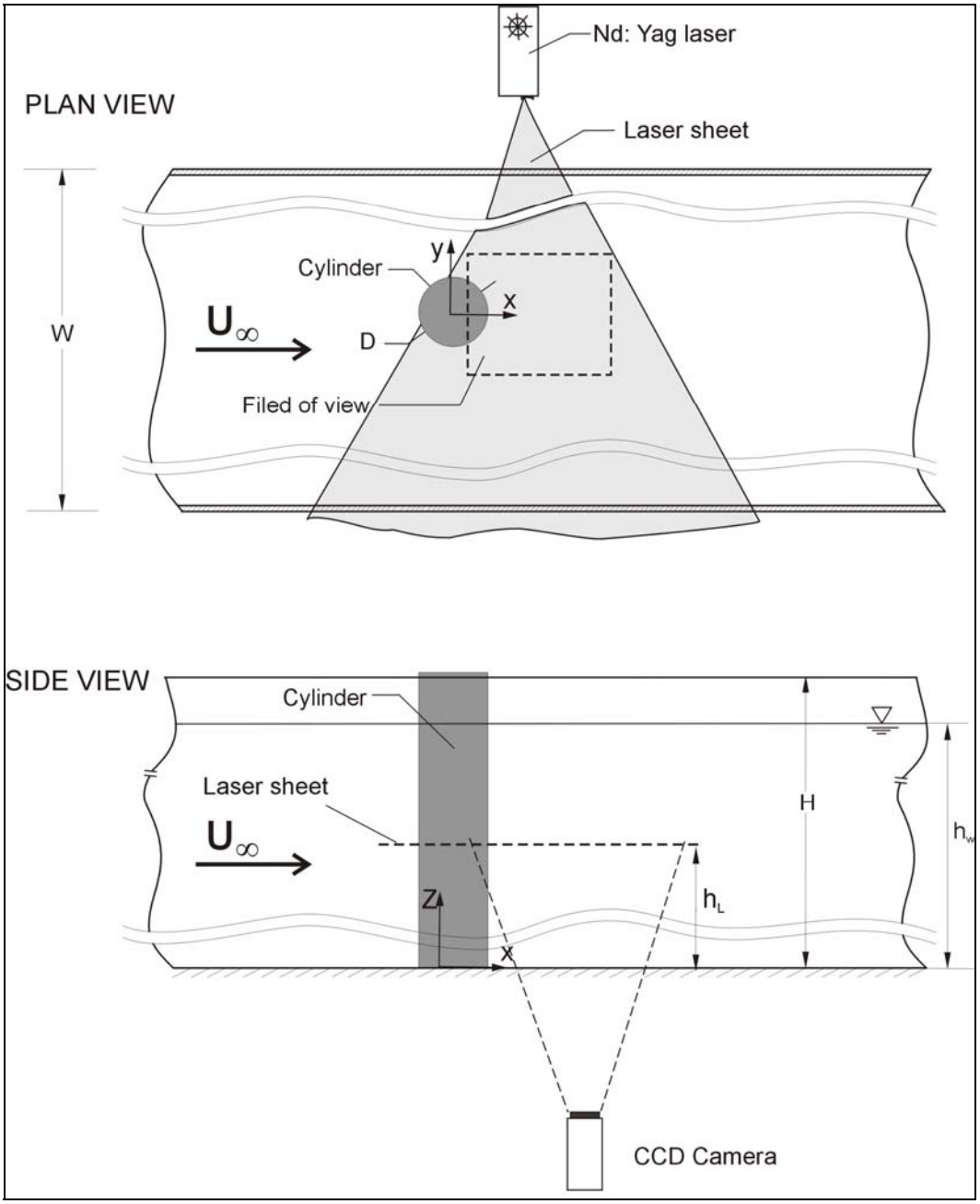
Motivation of this research can be explained as follows. Most previous experimental works on sphere and cylinder wake have been carried out mainly using point-wise measurement methods and conventional flow visualization techniques to investigate the flow characteristics of the wake region. Recently, many numerical simulations have been conducted to investigate the cylinder and sphere wake with improved turbulence models. However, the numerical simulations have a difficulty in validating their predicted results such as flow separation angle, recirculation length, and turbulence statistics due to lack of comparative experimental data at a higher Reynolds number of Re=5000. This implies that there are strong demands for reliable experimental data of the cylinder and the sphere wake to approve CFD module and results. The purpose of this study is to investigate and compare the flow pattern of the sphere and cylinder

by using a global visualization technique of PIV and dye experiments in moderate Reynolds number Re=5000 in terms of instantaneous and time-averaged velocity, vorticity, streamline topology, and Reynolds stress correlations along with root mean square (rms) velocity.

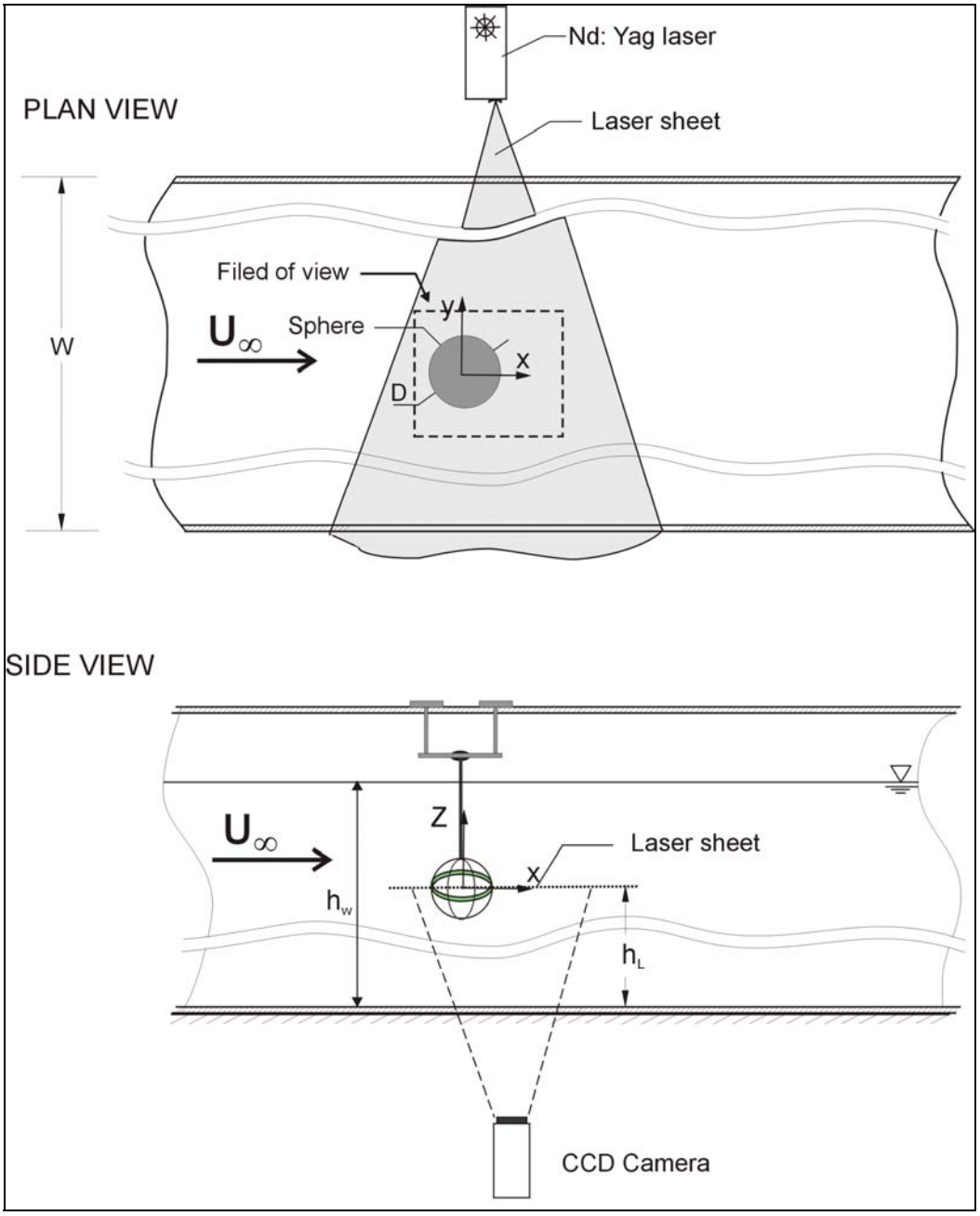
In the literature search, it is not encountered any research that directly compares the flow characteristics of these two main bluff bodies. Informative data for both numerical simulations and designers have been provided.

4.1.2. Experimental Arrangement

An overview of experimental system of the sphere and the cylinder was shown in Figure 4.1 The cylinder with a diameter of 50mm was made of Plexiglas so that the laser light propagates easily from cylinder. In addition, water cell segment of the sphere equator having a diameter of 38.5mm and a wall thickness of 2.0 mm are created. It was filled with distilled water and had a total length of 8 mm in order to reduce largely the laser light deflection on the sphere. The surface of the sphere is highly polished to avoid effects of surface roughness. The laser sheet was located at 230 mm above the bottom surface of the channel while the water height hw was 450 mm in all cases. . The solid blockage ratio of the sphere including support and the cylinder are respectively 1.3 % and 5%. Nd:Yag laser was used to generate a laser sheet that is perpendicular to the axis for the cylinder and the symmetry axis (i.e. equator of the sphere) is passed through them. A CCD camera having a resolution of 1,600 x 1,186 pixels was used to record the images. The output of the laser was transmitted through a cylindrical lens, which generated the planar laser to illuminate metal coated small particles in the water flow. The seeding particles with a diameter of 10 μm in the flow were silver metallic coated, hollow plastic spheres. The specific gravity of the seeding particles. The densities of the particles and water were equal so that the distribution of particles in suspension remained uniform for several hours.


Nd: Yag laser
PLAN VIEW
Laser sheet
y
Cylinder
x
W
U∞
D
Filed of view
SIDE VIEW
Cylinder
Laser sheet
H
hw
U∞
Z
hL
x
CCD Camera

a) cylinder



b) sphere

Figure 4.1. Schematic of the experimental system and presentation of measuring sections

The high-image-density criterion was satisfied by ensuring that a minimum of approximately 20-30 particles was contained within the interrogation area. The illuminating laser sheet thickness in the flow field was approximately

1.5 mm. As shown in Fig. 4.1., the camera was mounted in a fixed position beneath the water tank. As shown in Fig. 4.2. Dantec Flow Grabber digital PIV software employing the cross-correlation algorithm was used to compute the raw displacement vector field from the particle image data. An interrogation window of 32x32 pixels in the image was selected and converted to grid size approximately 2.162x2.162 mm^2 (0.043DX0.043D) for the cylinder and 1.488x1.488 mm2 (0.035DX0.035D) for the sphere. The overall field of physical view was 211.9x155.66 mm2 (4.24Dx3.11D) for the cylinder and 145.8x107.2 mm^2 (3.43Dx2.52D) for the sphere, yielding to 7,227 (99x73) velocity vectors. During the interrogation process, an overlap of 50% was employed in order to satisfy the Nyquist criterion. Patterns of instantaneous particle images (total of 350 images for a continuous series) were taken at the rate of 15 Hz, thereby spanning 23.27 sec. Averaged patterns of the flow structure were calculated from all of the instantaneous images. After having been vector field, the vorticity patterns of the wake flow were determined from the velocity field using a finite difference scheme with an in-house software.

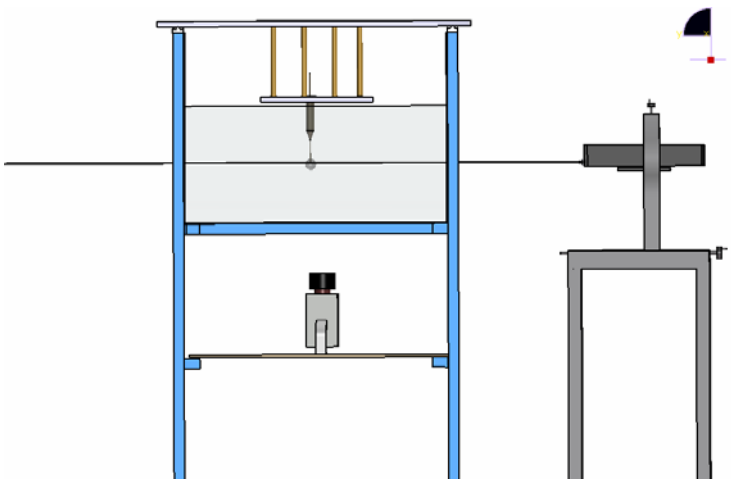


Figure 4.2. The scheme of experimental arrangements which includes positions of camera and laser.

4.1.3. Results and Discussion

4.1.3.1 Dye visualization Results

Typical visualization images of instantaneous flow field around a sphere and cylinder model are shown in figures 3, 4, 5 at Re=5000. The separated and recirculating flow in the near wake region with the help of visualizing is clearly seen for the sphere and cylinder. Small scale vortices around the wake region are formed in a wavy appearance due to Kelvin Helmholtz (KH) instability. As seen image (i-ix) of Figure 3, evolution of the spiral vortices begins to occur in the very close region of the sphere, as the flow travels in the downsteam flow direction, dimensions of the vortices increase. Then these vortices shed from the periphery of the sphere directly to the inward wake region but they do not come–close to each other in the wake region right behind the sphere due to the momentum transfer. Karman vortex streets (KVS) form in the far wake region in Figure 5. On the other hand, well-known Kármán vortex shedding in the case of cylinder begins to occur immediately by the separation phenomena as demonstrated in Figure 4, which is recorded by Akilli et al (1994). As seen in the rear side, the wake is highly unsteady and large eddies or vortices are shed from the downstream region of the cylinder. The large eddies are formed at a regular frequency and they produce pressure disturbances in the flow. In the top image, there is a dominant large-scale Kármán vortex occurs in the upper side of the cylinder whereas in the bottom image it occurs in lower side of the cylinder. In Fig. 4.3 and 4.5, the laminar flow separation is developed near the equator of the sphere model. The recirculating flow region is formed downstream of the sphere is clearly visualized by dye filaments convected upstream by reverse flow and downstream by momentum transfer. The laminar shear layer continues approximately one diameter further downstream of the sphere in Figures 4.3 and 4.5. Thereafter, the laminar shear layer turns into turbulent flow structure. Several vortex-ring shaped protrusions are appeared as an indication of the shear-layer instability along the borders between the wake and free stream region. The flow patterns in Figures 4.3. and 4.5. show that at Re=5000 the boundary layer

separates at around θ=85^{o}, where θ is measured form the front stagnation point. In figure 4.4., it is seen that the near wake recirculating region is large and the wake performs a progressive wave motion.

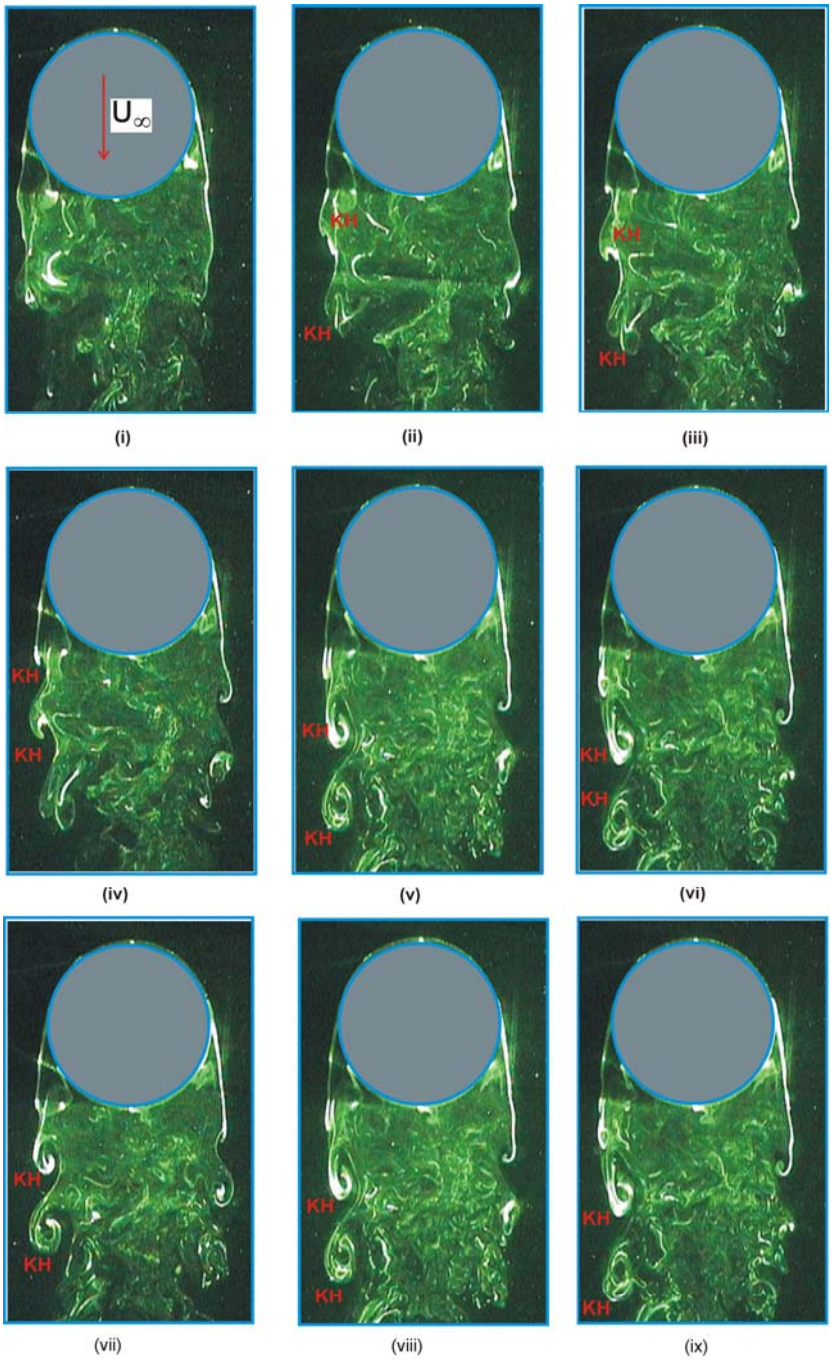
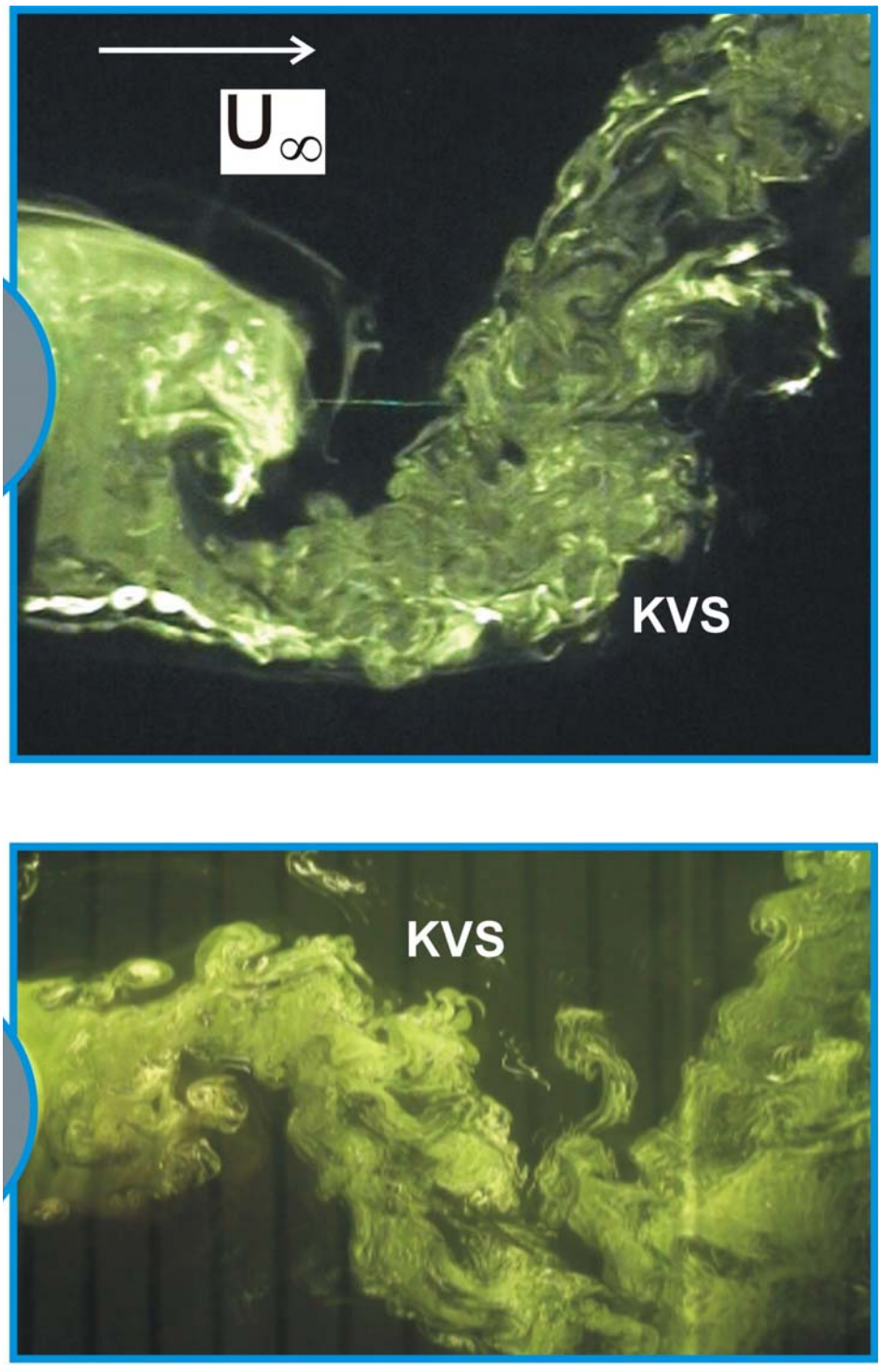


Figure 4.3. Instantaneous flow visualization with laser illumination of Rhodamine dye injection technique in near wake region around a sphere is illustrated. Evolution stages of the flow structure are shown at Re=5000.



(b)

Figure 4.4. Instantaneous flow visualization with laser illumination of Rhodamine dye injection technique around a cylinder for Re=5000 in shallow water is displayed (Akilli et al.,2004)

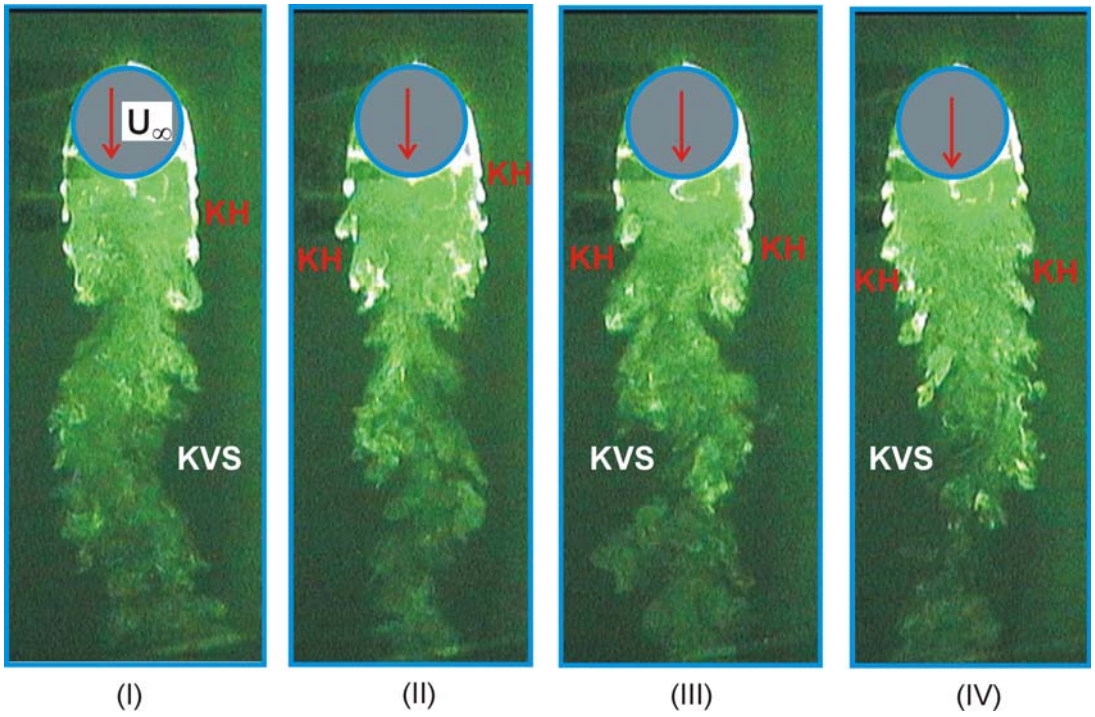


Figure 4.5. Instantaneous flow visualization with laser illumination of Rhodamine dye injection technique in far wake region around a sphere for Re=5000 is shown.

4.1.3.2 Spectral analysis and calculation of vortex shedding frequency

It is seen that well-known Karman vortex street is formed in the cylinder wake region whereas shedding vortices are attached circumferentially on the sphere surface. The frequency of vorticity pairs is a function of velocity, cylinder diameter and Reynolds number Lin et.al.(1995). The frequency of vorticity pairs is a function of velocity, cylinder diameter and Reynolds number. Figure 4.6 shows the dominant vortex shedding frequency *f* which is determined from power spectra of recorded DPIV data in the near wake region of the cylinder and sphere, particularly inside free shear layer region, at the various selected points. FFT analysis in the wake of the body which reveals significant quasi-periodic flow oscillations. As it is known, the most powerful spectral peak reflects vortex shedding frequency in the spectra. Frequency spectrums were accomplished by the time-averaged velocity padding to the 350 DPIV data in consecutive in order

to extend input data number at a value of 512 samples, power of 2, for each spectrum analysis in Fig. 4.6.

Spectral peaks do have different dominant frequencies and magnitudes due to the 2D and 3D bluff body geometry as displayed in Fig. 4.6.

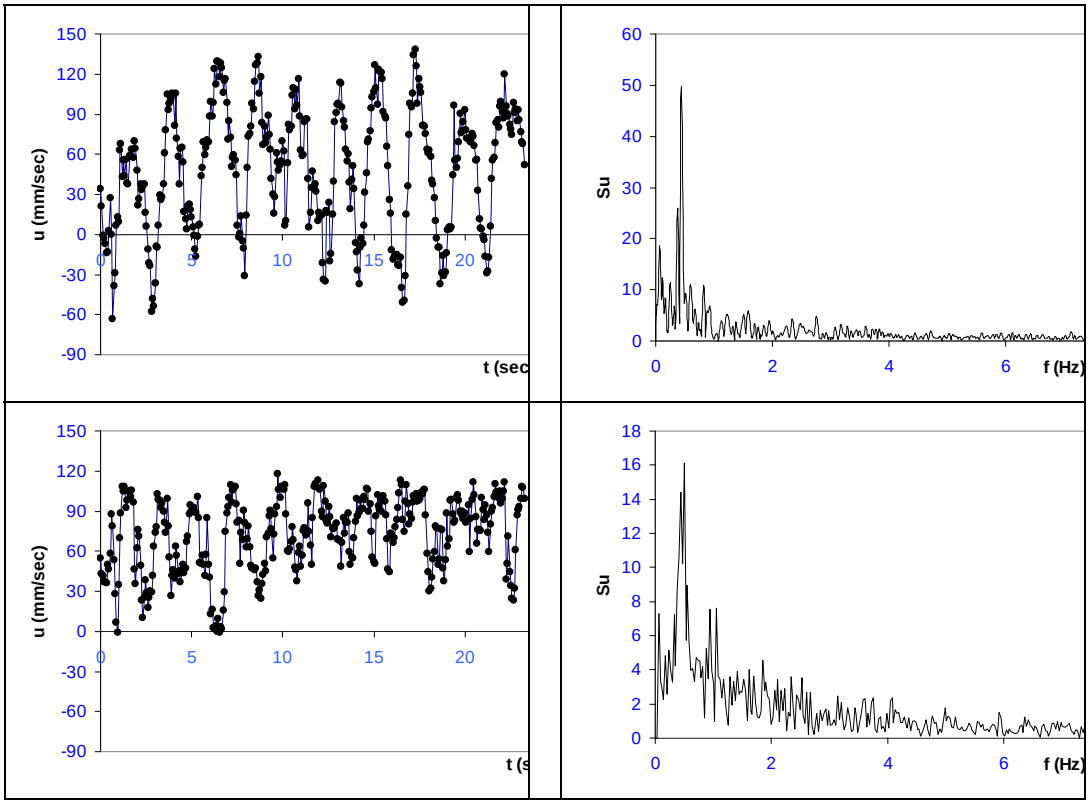


Figure 4.6. Time history of instantaneous streamwise velocity component u (mm/s) against time t (s) and spectrum analysis St for the cylinder (top two graphics) and the sphere (bottom two graphics) at Re = 5000.

Representative streamwise velocity component u was given for the cylinder and the sphere. Variation of the u component velocity and its spectrum in the cylinder wake region is higher than in the sphere due to the alternating KVS. The peak frequencies of vortex shedding are calculated as 0.42 Hz and 0.49 Hz for the cylinder and sphere, respectively. Strouhal numbers for the cylinder and the sphere are found to be 0.21 and 0.18 respectively. The value of St number agrees well with the results of Jang and Lee (2008), Suryanarayana and Prabhu

(2000) and Sakamoto and Haniu (1990). King (1979) reported that the non-dimensional wake Strouhal number for the CC was St≈0.21 over a wide range of Reynolds numbers, for example, $10^2<Re<10^5$.In the present study, Strouhal numbers obtained for the cylinder almost matched the value 0.21, generally found in literature.

4.1.3.3 Particle Image Velocimetry (PIV) Results

Representative instantaneous vorticity contours of the wake structure for the cylinder and sphere geometries at Re=5,000 are illustrated in Fig. 4.7. Results of many qualitative and quantitative investigations explain the well-known Kármán vortex shedding for the cylinder. In the image from top to bottom, there is dominant vortex shedding variation of a large-scale Kármán vortex in the upper side of the cylinder to the alternated direction. Viewing the vortex street in cross-section plane, concentrated vorticity layers are shed into downstream flow from alternate sides of the body, giving the appearance of upper row of negative vortices (dashed lines) and lower row of positive vortices (solid lines). Flow at the rear of the body coming from the upper side of the cylinder reverses clockwise whereas lower side of the cylinder rotates anticlockwise direction. These are known as shear layers which alternately roll up to form vortices in the wake. One of these shear layers coming from the opposite side of the wake entrains into the growing shear layer of the other side of the cylinder. This induces the detachment of longer shear layer vortex from the cylinder. Shorter vortex shedding located near the cylinder has a rotating reverse flow towards the cylinder, which detaches the vortex from the cylinder surface and initiates production of the next vortex. Bloor and Gerrard (1966) postulated that the vortex continued to grow, fed by circulation from its connected shear layer, until it was strong enough to draw the opposing shear layer across the near wake.

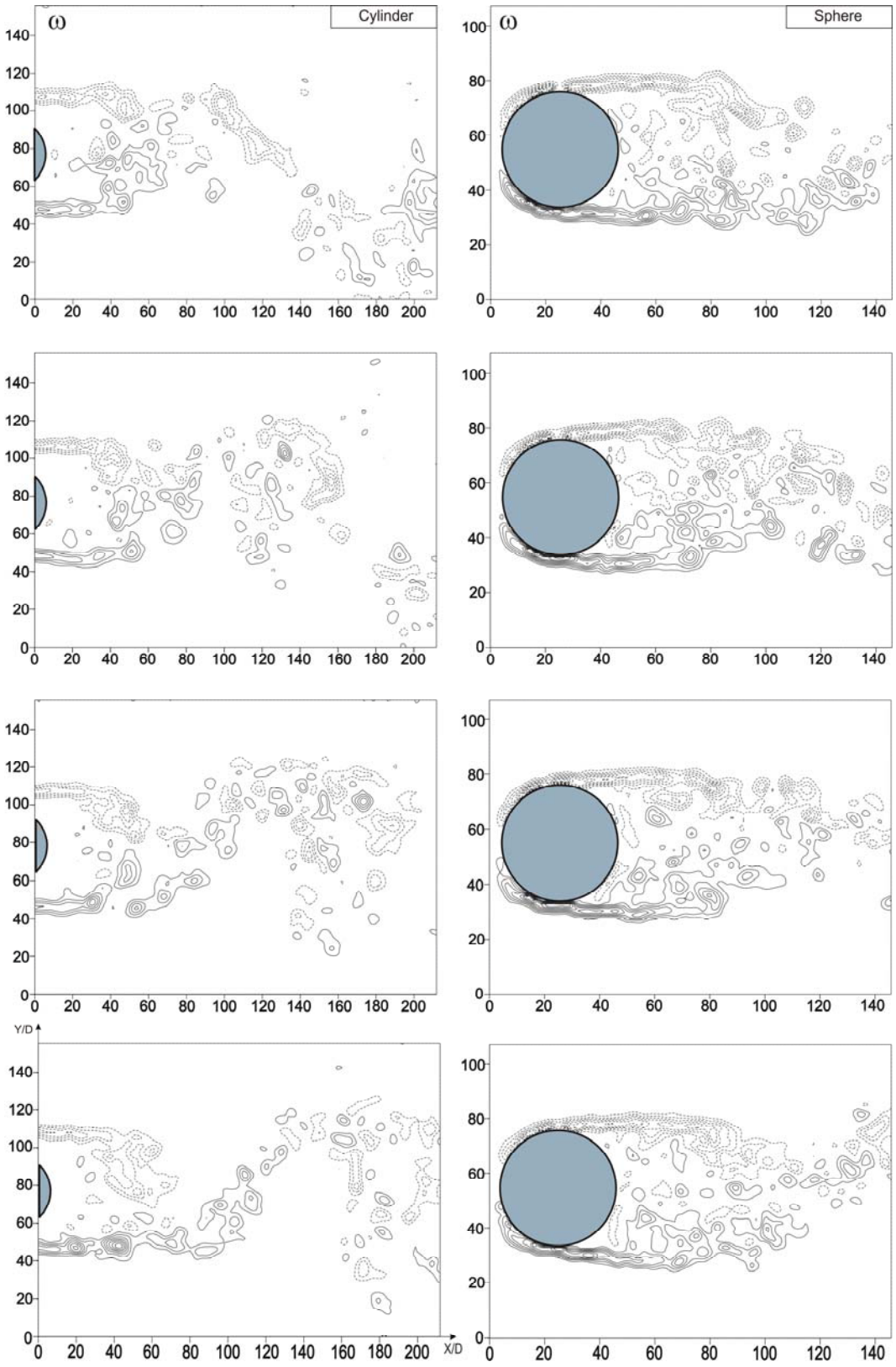

ω
Cylinder
ω
Sphere
Y/D
X/D

Figure 4.7. Comparison of patterns of instantaneous vorticity ω for the cylinder (left column) and the sphere (right column) is presented at Re=5000. Both minimum and incremental contour levels of positive (solid line) and negative (dashed line) instantaneous vortices in all images are 6 (1/sec). All patterns are scaled with respect to the bluff body size

Instantaneous vorticity patterns clearly present the interaction between the shear layers formed both sides of the cylinder and the sphere. The cylinder wake is wider than the sphere wake for all presented flow patterns because of having different diameters and earlier occurrence of the KVS. The vortices produced from flow separation around the periphery of the sphere have a tendency to displace inwards direction because of lower pressures prevailing within the wake. This is counter-balanced by the growing wake size, which shifted the vortex centerline outwards. It is evident that the flow characteristics downstream of the sphere are more complicated than the cylinder. In fact, the large-scale cluster of vorticity induces a negative layer of vorticity immediately adjacent to the base of the cylinder as seen in the left column of Figure 4.7. Regarding the onset and development of small-scale vortical structures in the separating shear layer, regions of low-level vorticity concentration are discernible in the pattern of instantaneous vorticity for the cylinder and the sphere. Large-scale Kármán vortices form in the near-wake region due to the abrupt coalescence of small-scale shear-layer vortices that developed in the separating shear layers similar to the work of Ozgoren (2006) and Lin et al. (1995). Instantaneous vorticity patterns showed the irregular vorticity shapes and the shear layers tends to break up easily into small concentrations of vorticity related to Kelvin-Helmholtz (KH) instabilities for both geometries. They seem to combine into larger vortices during the process of formation and shedding, as shown in Figures 4.7. At Re=5,000, these concentrations become more pronounced, and small-scale structures are clearly evident inside and at the periphery of the large-scale vortex. Concentrations of the small-scale vortices for the sphere are more stronger than the cylinder.

Comparison of dimensionless flow patterns of the cylinder (left column) and the sphere (right column) for time-averaged velocity field <V>, streamline

topology Ψ, streamwise velocity <u> cross-stream velocity <v>, time-averaged vorticity <ω>, streamwise Reynolds normal stress $< u'u'/U_\infty^2 >$, transverse Reynolds normal stress $< v'v'/U_\infty^2 >$, Reynolds stress correlations $< u'v'/U_\infty^2 >$ rms (root mean square) contours of the streamwise velocity $< u_{rms}/U_\infty >$, cross-stream velocity $< v_{rms}/U_\infty >$ and vortcity $< \omega_{rms}/U_\infty >$ are presented in Figures. 4.8, 4.9 and 4.10. For these figures, minimum and incremental values of the patterns are given on each image. All patterns are scaled with respect to the bluff body size.

The time-averaged vorticity images of the sphere and the cylinder reveal that the detailed instantaneous structure of the small-scale vortices and far downstream part of the Kármán vorticity street are lost due to unsteady flow structure and alternating direction of the shedding vorticity from both sides of the cylinders. The streamwise separation of successive vorticity peaks in the near wake region for the cylinder is larger and longer than that of the sphere. The shape of vortex contours in the near wake is similar for both geometries. Two large scale recirculation vortices formed behind the sphere are nearly symmetrical with respect to the wake centerline, even though instantaneous vortex structures are unsteady and irregular. These clear recirculating large-scale vortices are the dominant flow pattern in the near-wake behind a sphere and in a good agreement with those of other previous studies (Jang and Lee 2008, Ozgoren 2006, Constantinescu and Squires 2003, Hadzic et al. 2002, Leder and Geropp 1993.)

Time-averaged velocity field obtained by ensemble averaging 350 instantaneous velocity fields is shown at the top row of Figure 4.8. The time-averaged streamline topology are interpreted in terms of foci and saddle points. Comparison of he time-averaged patterns show that flow structures of the wake are almost equally symmetrical with respect to the centerline of the cylinder and sphere in Figure 4.8. Patterns of time-averaged streamline topology <Ψ> identify the major changes of the near-wake behind the cylinders. They exhibit well-defined critical points, e.g. foci (centers of vortices) designated as F_1 and F_2 and

saddle points (apparent intersection of streamlines) denoted as S, as shown in Figure 4.8

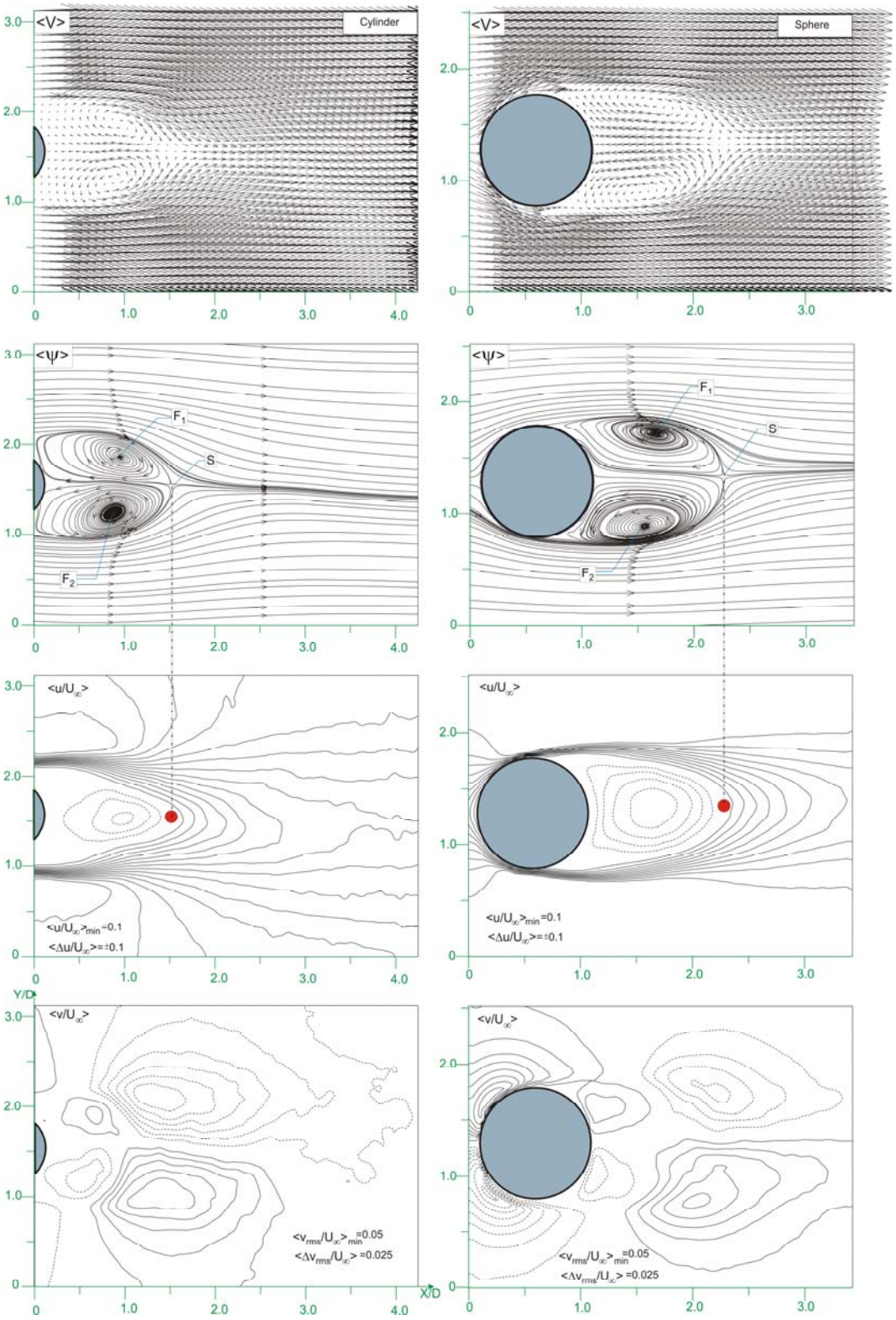


Figure 4.8. Comparison of flow patterns of the cylinder (left column) and sphere (right column) for dimensionless time-averaged velocity field <V>, streamline topology, < Ψ> streamwise velocity <u> cross-stream velocity <v> is shown for Re=5000.

Averaged streamline patterns in Figure 4.8, streamline shapes extended upstream to the near base region of the sphere and cylinder are elliptical and have a limited spiral cycle. The saddle point on the time-averaged streamline topology forms earlier for the cylinder. Whole field representations of streamline patterns along with the identification of the locations of these types of critical points could provide an insight into the effective formation length of large-scale vortices and the degree of symmetry of either side of the near-wake. The non-dimensional wake lengths (*L/D*) measured from the central point of the cylinder and the sphere to the saddle point in the averaged streamline topology <Ψ> for Re=5000 are approximately 2 and 1.65, respectively.

Representations of the streamwise velocity component <u> over the entire field of view are also given in the third row of Figure 4.8. From these images, definition of the location of the stagnation point along the plane of symmetry of the wake is also possible as designated by a red dot. The distance from central point to the stagnation point is approximately 2.03D and 1.65D for the cylinder and sphere, respectively. At these locations, as well as at locations downstream, local bulges of the cross-sectional patterns of the wake are evident; they are consistent with regions of abrupt wake widening observed in the sectional patterns of the flow structure for the cylinder and sphere as seen in Figures 4.7 to 4.1. 9. Patterns of time-averaged cross-stream velocity <v> are given in the fourth row of Figure 4.8. The patterns of cross-stream velocity are detectable near the interface between the separating shear layers. These contours indicated that the cross-stream velocity is oriented in the direction of each respective shear layer which is separated from the shoulder of the cylinders. Large-amplitude cross-stream velocity <v>, at Re=5000, might indicate that the developing shear layer, which originally separates from the cylinder and sphere entrained a significant mass flow in the base region through both sides. A possible explanation for this phenomenon is an increase in the level of Reynolds stress in the separating shear layer as seen

in the bottom row of Figure 4.9. It might be concluded from pattern concentrations that Reynolds stress correlation contours have considerably enhanced values for the cylinder comparing to the sphere.

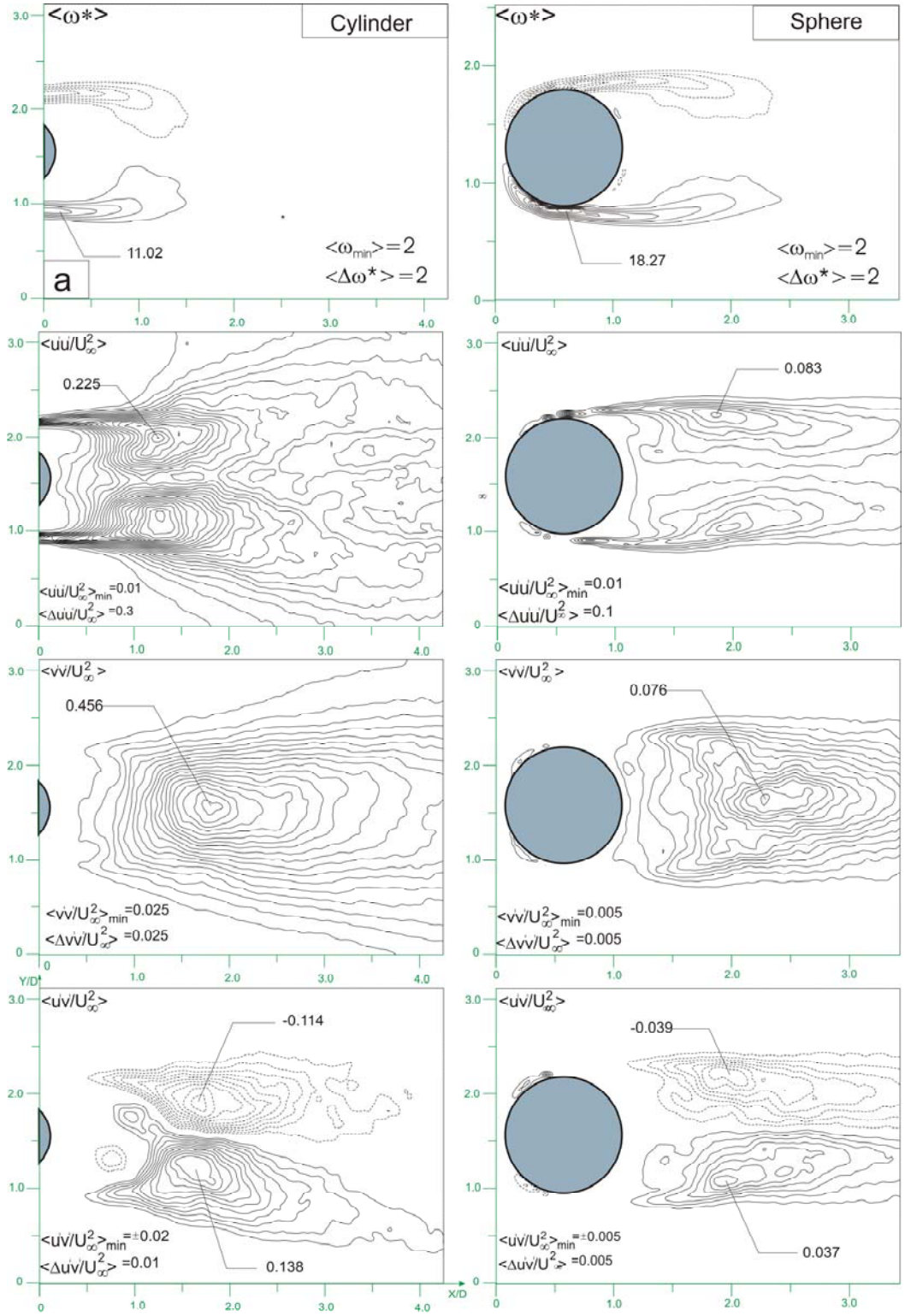


Figure 4.1. 9. Comparison of dimensionless time-averaged flow patterns of vorticity <ω>, streamwise Reynolds normal stress $< u'u'/U_\infty^2 >$, transverse Reynolds normal stress $< v'v'/U_\infty^2 >$ and Reynolds stress correlations $< u'v'/U_\infty^2 >$ is given for Re=5000 for a cylinder (left column) and sphere (right column).

The rms flow patterns display similar behavior for the cylinder and sphere whereas they have discrepancies from the point of the flow pattern concentrations and vortex formation length as seen. In the wake region of the cylinder, higher values of fluctuation levels and irregularities are evident in the separating shear layer. The rms streamwise velocity patterns $< u_{rms}/U_\infty >$ have easily detectable double peaks at almost equal location in the upper and lower wake region of the centerline for the cylinder and sphere in Figure 4.10, which are placed around 1.15D and 0.87D downstream from the body rear for the cylinder and sphere, respectively. For the contours of $< v_{rms}/U_\infty >$, the cross-stream fluctuations are associated with the process of formation of the large-scale vortical structures. The maximum contour values of $< v_{rms}/U_\infty >$ for Re=5000 in the centerline of the wake take place nearly 1.65D and 1.37D for the cylinder and sphere respectively. The cross comparison of the results reveals double peaks for $< u_{rms}/U_\infty >$ while single peak is seen in $< v_{rms}/U_\infty >$ with a maximum.

Reynolds stress correlations $< u'v'/U_\infty^2 >$ depict a set of extrema on either side of the wake centerline for the cylinder and sphere in the bottom row of Figure 4.9, which provide direct comparison of patterns for the cylinder and sphere from the point of bluff body shape and momentum transfer. The patterns of the Reynolds stress correlations for the cylinder consist of small-scale clusters located in the vicinity of the base of the cylinder and large-scale clusters located just downstream of the small-scale clusters. However, there is only large-scale cluster for the sphere. Well-defined Reynolds stress patterns due to fluctuations in the shear layers produce a weaker Reynolds stress region very close to the base of the cylinder which occurs as a result of the entrainment of free stream flow into

this wake region. This behavior of the flow provides the momentum transfer from the free stream flow into the wake region owing to pressure difference between the wake and free stream. The upstream extension of each large-scale cluster of $< u'v' / U_\infty^2 >$ migrates further upstream and the tip of the large-scale clusters is located closer to the base of the cylinders for Re=5,000 in Figure 4.9. Same signed Reynolds stress correlation patterns $< u'v' / U_\infty^2 >$ and cross-stream velocity components <v> extend one side of the centerline to the other for the cylinder. Peak values of Reynolds stress correlations increase in the base region and then decay sharply in the wake region as seen from concentrations of the flow. Reynolds stress correlation $< u'v' / U_\infty^2 >$ is zero around the axis as a result of symmetrical flow structure and attains its highest magnitude in the upper and lower region of the centerline although peak values of $< v_{rms} / U_\infty >$ occurred at the axis itself. Thus, velocity fluctuations penetrate deeper into the outer flow and finally caused an increase on the drag coefficient as a result of increased wake size. The Reynolds stress correlations in and around the mean wake recirculation region are primarily due to the time-dependent nature of vortex shedding. In this limit, it is observed that the Reynolds stress correlation is relatively small in the outermost region of flow patterns as displayed in the bottom images of Figure 4. 9. Despite the significant differences in the geometry of the bluff body, the distribution of Reynolds stress patterns around the wake bubble is quantitatively similar to the corresponding distributions for the cylinder and sphere. However, the measured values of the peak Reynolds stresses are somewhat higher for the cylinder than those of the sphere. Furthermore, the peak values of normalized Reynolds stresses $< u'v' / U_\infty^2 >$ for the cylinder and sphere are 0.138 and 0.039, respectively. The reason of the smaller peak values for the sphere is that the degree of fluctuations and random flow movements is very much higher than the cylinder case.

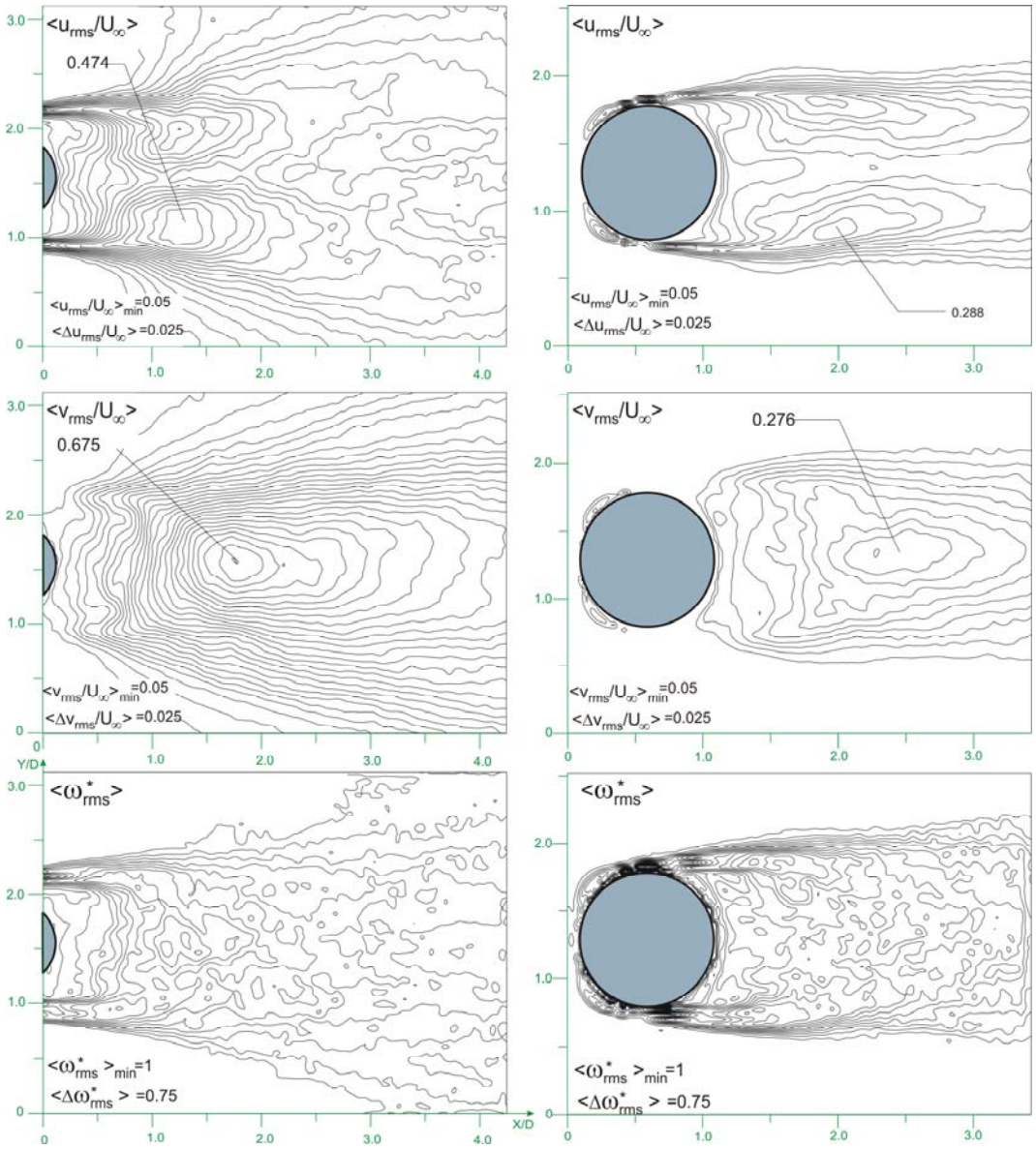


Figure 4.10. Comparison of dimensionless time-averaged flow patterns of rms contours of the streamwise velocity $< u_{rms}/U_\infty >$, cross-stream velocity $< v_{rms}/U_\infty >$, vorticity $< \omega_{rms}/U_\infty >$ is displayed for Re=5000 for a cylinder (left column) and sphere (right column).

4. 2. Investigation of three Dimensional Flow characteristics around side by side spheres

4.2.1. Introduction

The understanding of flow around spherical objects, which are the best example of three dimensional symmetric solid bodies, is considerably important for design of low drag vehicles, dry process of some products and industrial applications which includes pneumatic transport effected by multi-phase flow. The flow structure around sphere is assumed as a simple situation of submerged body in fluid flow.

There are many examples for spherical objects in nature such as; balloons, bombs, storage tanks of petrol and similar products and submarines etc. There are many studies in literature which investigate the flow structure over sphere and interaction of flow and sphere.

On the other hand, these studies were limited with either small particles and low Reynolds number or qualitative results. Certain reasons of this limitation are complexity of the flow structure which is caused by the three dimensional structure of sphere and supporting difficulty of a sphere in water channel or wind tunnel test section, large area of separated flow and strong time dependency. Bluff bodies generally cause flow separation, unsteady flow and complex vortex shedding. The knowledge about forces due to the flow around spherical object and frequency of vortex shedding occurred downsteam of spherical object are very important to conduct static and dynamic load calculations of forces acted on the spherical object. Dynamical behavior of spherical objects due to their flow structure is determined only with determining the optimum design conditions of real flows. Observation of the interaction between sphere and flow reveals the general characteristics of the flow structure. This interaction leads a complex and unsteady flow characteristics which is a function of arrangements of spheres. Instantaneous vorticities around sphere cause dynamic loadings and vibrations. These vibrations could cause fatigue and noise pollution. Detailed measurements and analyses of fluid-body interaction should be performed to determine the source of these adverse effects. It is very hard to evaluate the flow structure around sphere qualitatively due to the complexity and

three dimensional characteristic of the flow structure. However, the PIV technique which allows to measure quantitatively provides researchers both practical and design parameters.

Importance of this study is that in literature there is no detailed observation of the three dimensional flow structure around single sphere and side-by-side spheres using the PIV technique.

To be able to understand the comparison of flow structure of both single sphere and two spheres with different arrangements, flow patterns given in the first chapter were reprocessed with new values in this section.

4.2.2. Experimental Arrangement

Experiments were conducted in a low-turbulence water channel. The experimental set-up consists of a closed-loop open-surface water channel. Spheres used in the experiments were made of transparent material with D=42.5mm. Spheres used for dye and PIV experiments were shown in Figure 4.11. a and b. The test chamber was large enough to prevent the effect of the channel side walls. Spheres were constructed a space in it. This empty space filled with water to avoid the reflection of the laser light.

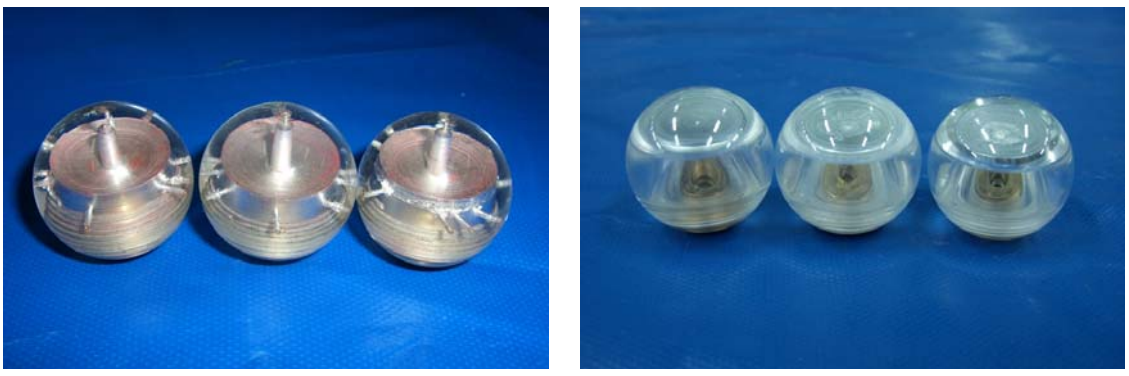


Figure 4.11. a) spheres used for dye experiments b) Spheres used forPIV experiments

The laser sheet passed through the central plane (equator) of the sphere. The thickness of the sphere is 2.5 mm at the central plane which is located at H_L =230 mm above the bottom surface of the channel. The surface of the sphere is polished to avoid effects of surface roughness. To support the sphere in the water channel, a circular bar connected to the sphere from the top has 5 mm diameter A special aperture shown in Figure 4.12 were used in all experiments. This airfoil edged rod has 3 mm width and 5 mm length as a maximum dimensions. Therefore, There was no effect of the rod on the flow structure over the sphere. The solid blockage ratio of the sphere including support is 1.3 %. The depth of water in the test section was adjusted to Hw = 450 mm for all experiments. An overview of experimental system of the sphere was shown in Fig. 4.13.

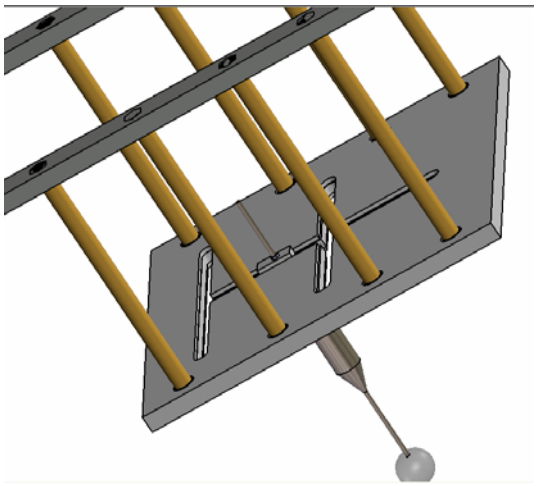


Figure 4.12. Sketch of the special aperture

Free stream turbulence intensity of the flow is less than 0.5% in the range of the present Reynolds numbers range, $\mathrm{Re} = (U_\infty D)/\nu$, based on the sphere diameter. Here, ν and D is the kinematic viscosity and the diameter of spheres, respectively. U_∞ is the free-stream velocity. Experiments were performed into two stages. Initially, dye experiments were performed. A fluorescent dye was used to visualize the flow around spheres developing color change in the flow when it encounters with the laser sheet. Dye was diluted with water and held in a small container above the channel. The dye passed through in a plastic pipe and injected into the water from surface of

the sphere. A laser based high-image-density particle image velocimetry (PIV) was used to determine the instantaneous and averaged flow data. The PIV experiments were conducted in two different planes called as a plan-view and end-view. Test section was illuminated by using a double-pulsed Nd: YAG laser. The laser sheet thickness was 1.5 mm for all experiments. To be able to perform PIV experiments, silver metallic coated spherical shaped particles seeded into water. These naturally buoyant particles have 10 μm diameter and the same density of water. A high resolution camera (1600*1186 px) was used to capture the instantaneous images. With the present system, maximum 15 images can be taken to capture the flow field images, the laser pulse and camera must be incorrect sequence and timing.

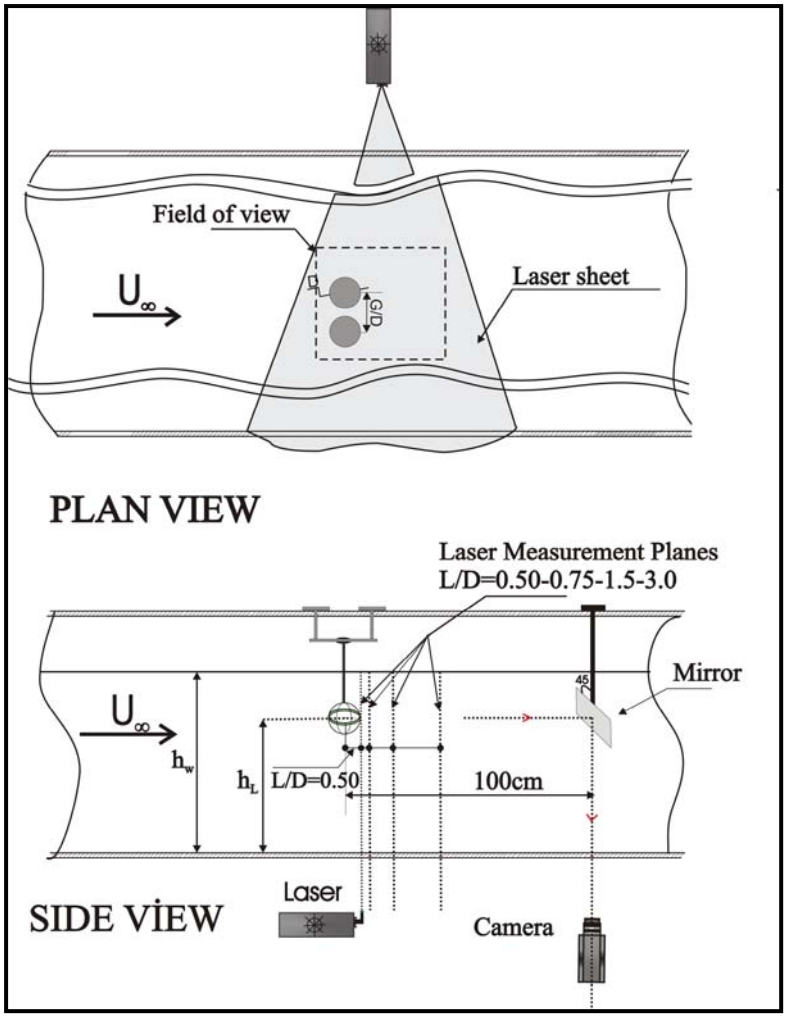


Figure 4.13. Schematic of the experimental system and definition of parameters for the sphere.

By this way, successive images can be taken in a short time with high precision and reliability. Adaptive correlation with 32*32 pixels interrogation window was used to obtain the instantaneous velocity fields. Fast Fourier analysis also were done. To increase the number of vectors and satisfy the Nyquist criterion 50% overlap was used for interrogation window. In the present study, 350 instantaneous images were taken for one set of experiments. The instantaneous velocity vectors were calculated from these images and used for to obtain time-averaged vorticity contours, streamlines, Reynolds stresses, Patterns of root mean square of both streamwise, U_{rms}, and transverse, V_{rms}, velocity fluctuations. For plan-view, an interrogation window of 32x32 pixels in the image was selected and converted to grid size approximately 1.488x1.488mm^2 (0.035Dx0.035D), whereas 1.059x1.059mm^2 (0.024Dx0.024d) for end-view plane. For both plan and end view, 72227(99x73) vectors were obtained over the entire field of images. The overall field of physical view was 145,8x107.2 mm^2 (3.43Dx2.52D).

In the present study, two dimensionless lengths were provided as a gap ratio G/D and length ratio L/D where G is the distance between centers of two spheres for plan-view experiments Whereas L is the distance between measurement plane and sphere surface for end-view experiments. Experiments performed for G/D=1.0, 1.25, 1.5 and 2 for plan-view and L/D=0,5 0.75, 1.5 and 3.0 for end-view planes as shown in Figure 4.13 .For experiments performed in the end-view planes a mirror which was located in water with 450 angle between streamvise flow direction. Initially the effect of the mirror on the flow structure over spheres was investigated and it had no effect on the flow.

4.2.3. Results and Discussion

4.2.3.1. Dye visualization Results

In the first part of the experiments, the flow structure around spheres was visualized by using fluorescent dye which shined under laser light. Dye was injected

from ports which were located on the central plane of the sphere with a certain increment angle. The dye visualization results for Re=5000 both short wake region and long wake region were given in Figures 4.14.(a-e) and 4.15.(a-f), respectively. As seen in Figures 4.14.a and 4.15.a of single sphere results, shear layer between separated flow and wake region has wavy form. On occasion, vortices have taken place at both side of the central axis of sphere symmetrically and simultaneously. These small size vortices rotate about their axis and move on in a wavy form over the sphere. Shear layers emanating from the both side of the sphere merge at a location approximately 2D from the centeral point of the sphere and instability rises ever since this event has been realized. These instabilities and disorderness in the flow retain further downstream in the free stream flow direction having an "S" form like Von Karman vortex streets approximately after a distance of 2.5D from the central point of the sphere. The case of touching of two spheres (G/D=1.00) is seen in Figures 4.14.b and 4.15.b both for short and long wake region.

As fairly seen in Figure 4.14.b, the flow characteristics in the case of the touching of two spheres resembles considerably similar flow characteristics of the case of single sphere as seen in Figure 4.14.a in the region of small eddies which occur over the shear layer downstream of the sphere. But, the circulatory flow region downstream of the two spheres has lower velocity values compared with the case of single sphere as seen from both dye visualization results and time-averaged velocity vectors presented in Figure 4.18. As presented in Figures 4.14(b-e), the merging point of the shear layers downstream of the sphere could not be visualized clearly in the case of short length wake region and besides merging point wake flow moves downstream with "S" form. The jet-like flow occurs between spheres reaches to near region of the merging point of the shear layers as seen in Figures 4.14.c and 4.15.c for the case of G/D=1.25. However, examining all experiments it can be seen that this jet-like flow moved towards the sphere on the left-hand-side and because of this reason, the wake region of the sphere at the left hand side is smaller than the wake region of the sphere at the right hand side. The influence of the wake regions of spheres gets lower and the effect of the jet-like flow on the wake region increases when a distance between spheres is increased as seen in Figures 4.14.d and 4.15.d

for G/D=1.50. As seen in Figure 4.15.d, the separated flow regions merge at a location approximately 2D in the downstream direction from the central point of spheres. The flow around each sphere resembles same structure with the case of a single sphere considerably as seen in Figures 4.14.e and 4.15.e and 4.15.f. However, wake regions of spheres continue to interact with each other. In Figures 4.15.e and 4.15.f, present images are given for the experiments having same conditions. The wake regions of spheres expand further downstream in the freestream flow direction as an "S" form like Von Karman vortex streets approximately after 2.5D from central point of the sphere like the case of single sphere. Examining all images, these "S" forms have same phase or 90º phase time to time.

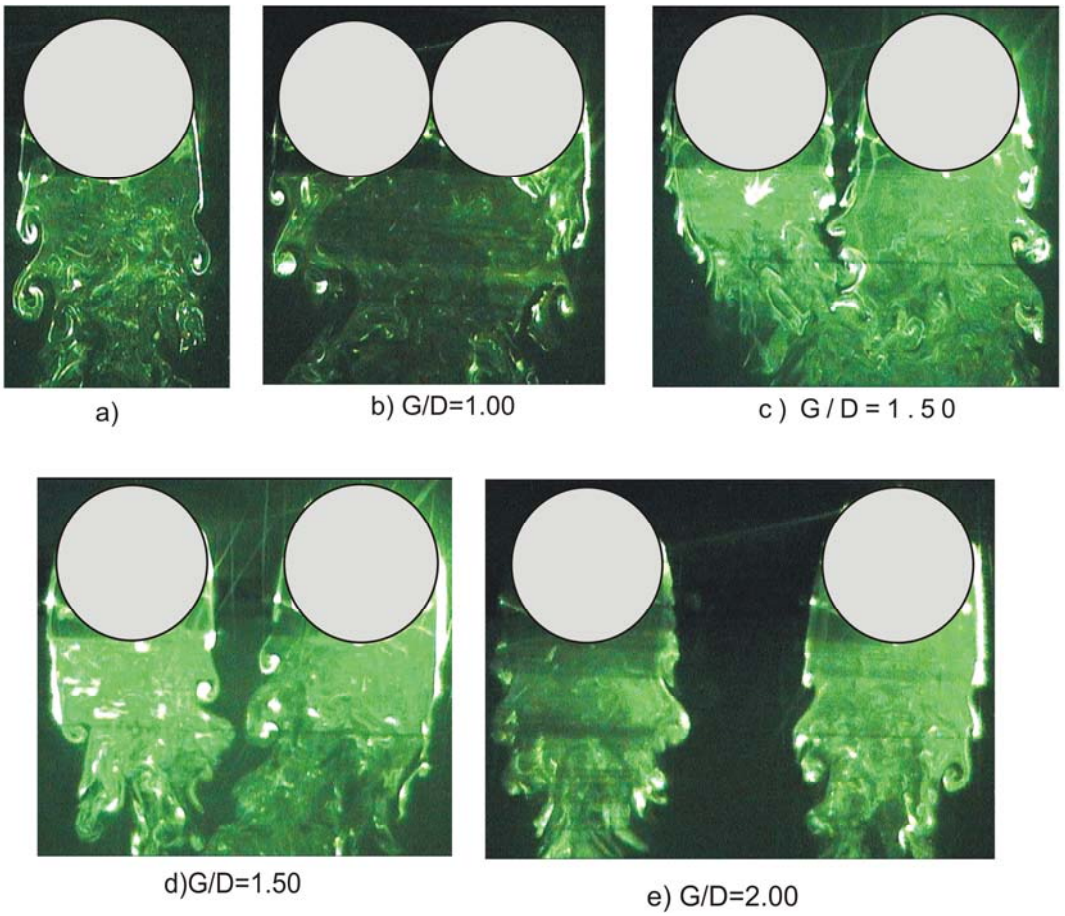


Figure 4.14. Dye visualization results for single and side by side sphere with various gap ratios for small wake region, Re=5000, G/D = b)1.00, c)1.25, d)1.50, e)2.00

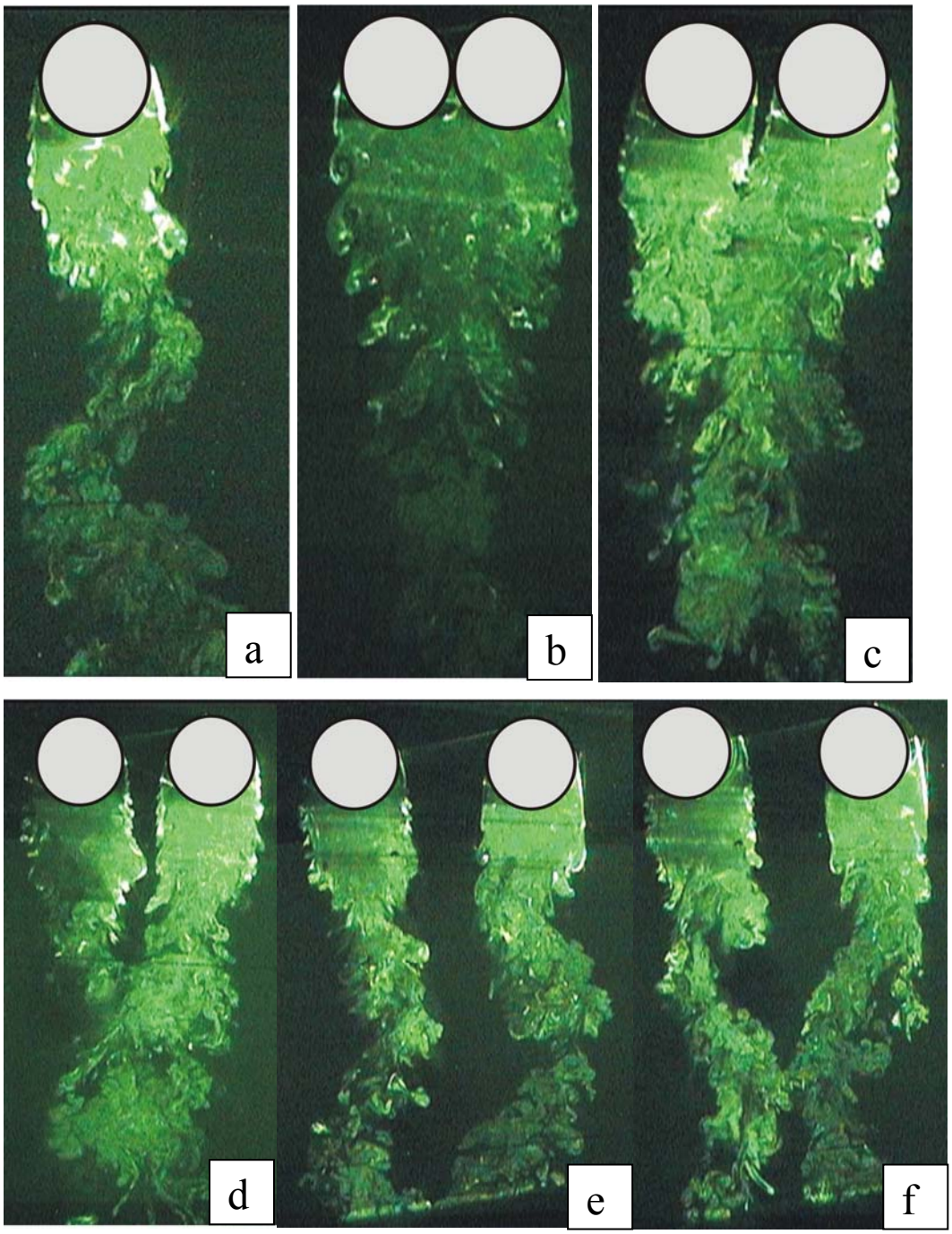

a
b
c
d
e
f

Figure 4.15. Dye visualization results for single and side by side sphere with various gap ratios for large wake region, Re=5000, G/D = b)1.00, c)1.25, d)1.50, e)2.00

4.2.3.2 Particle Image Velocimetry Technique (PIV) Results

Figures 4.16.a and 4.18 shows the dimensionless time-averaged velocity vectors which are obtained by ratio of velocity vectors and uniform velocity for the cases of single sphere and two side-by-side spheres. As seen in Figures, separated flow region moves towards the low velocity region downstream of spheres. It can be seen in Figure 4.16.b and 4.19 images of instantaneous velocity vectors, vortices developed by instable shear layer between recirculating flow region and free stream flow region towards the wake region contribute to produce new small eddies while they collide to surface of the sphere. These vortices increase the friction coefficient of the surface of spheres and dynamic loading to the sphere. It is known that the lifetime of spheres is going to decrease due to the dynamic loading. As stated in dye visualization results, the wake region of spheres move further downstream in the flow direction as an “S” form like Von Karman vortex streets approximately after 2.5D from central point of the sphere like the case of single sphere.

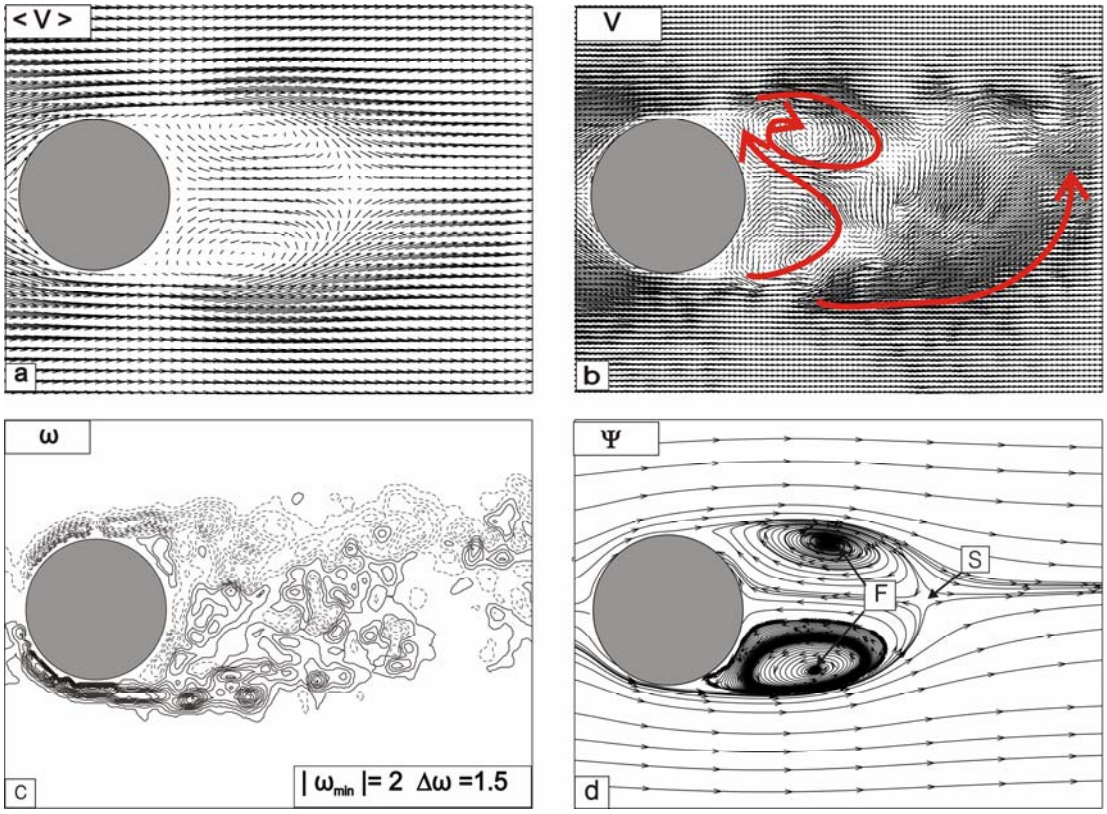


Figure 4.16. Patterns of a) time-averaged velocity vector <V>, b) instantaneous velocity vectors V, c) instantaneous vorticity contours ω, $|\Delta_{min}|=2$ d) time-averaged streamlines $<\psi>$, for the case of single sphere, Re=5000.

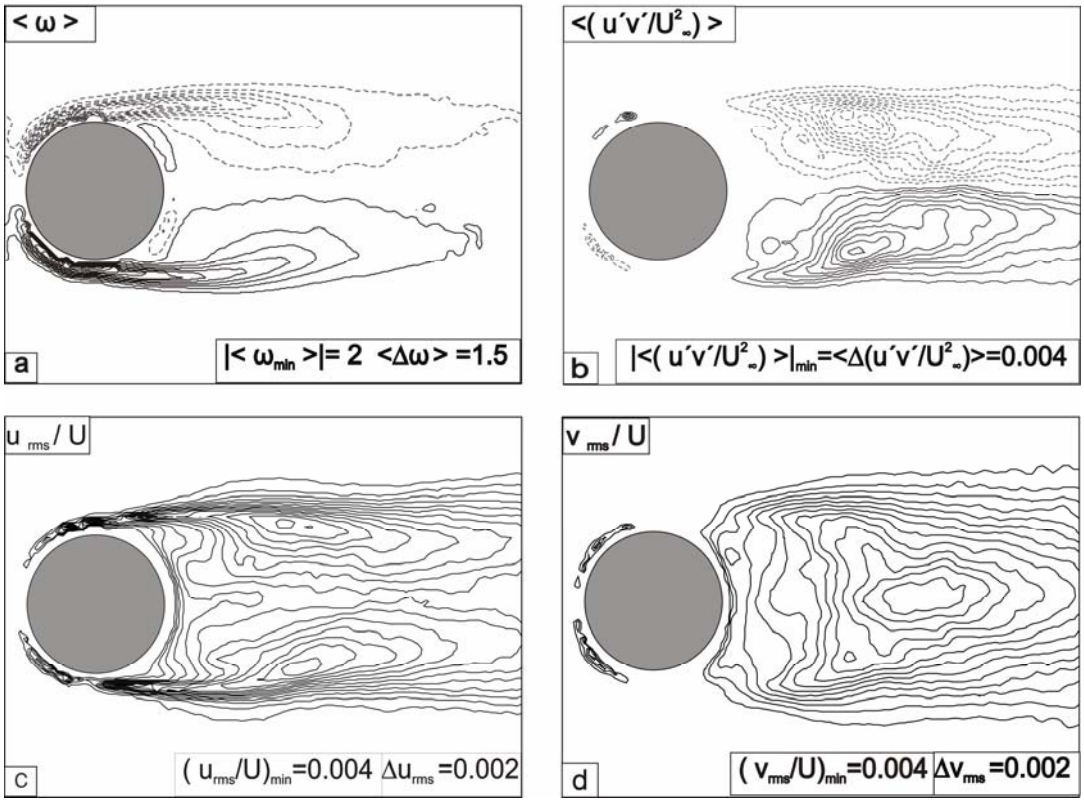


Figure 4.17. Patterns of a) time-averaged vorticity contours $|<\omega_{min}>|= 2$, $<\Delta\omega>=1.5$ b) Reynolds stress contours, $|< (u'v'/U^2)_{min}>| =0.004$ $<\Delta(u'v'/U^2)>=0.004$ c) square root of streamwise velocity, $<(U_{rms}/U)min>= 0.004$, $\Delta U_{rms}=0.002$ d) square root of transverse velocity$<(V_{rms}/U)min>= 0.004$ and $\Delta V_{rms}=0.002$ for the case of single sphere, Re=5000.

Examining all images, indicates that, these "S" forms in the behavior have the same phase or 90º phase. The instantaneous and time-averaged dimensionless vortices normalized by the sphere diameter, D, and free-stream flow, U_∞. Instantaneous vorticity contours indicate a high rate of fluctuating in the wake region due to the instability. The solid and dashed lines show the positive and negative time-averaged contours, respectively. Due to the high rate of variations in velocity magnitude in the separated flow region between wake and main flow regions, small and large size eddies occur. The magnitudes of fluctuating velocity increase with increasing gap between two spheres and it causes mass and momentum transfer from main flow region to the wake flow region. This situation causes the production of small eddies both in the inner side and outer side of the large vortices. It can be seen

from instantaneous velocity fields, the interaction between flow structure over two spheres gets lower with increasing gap between spheres and this interaction is almost over after G/D=2.00. Examining the cinema of instantaneous data indicates that fluctuations are quasi-periodic for the case of single sphere, but for the side-by-side arrangement especially in low gap cases these fluctuations are considerably unstable.

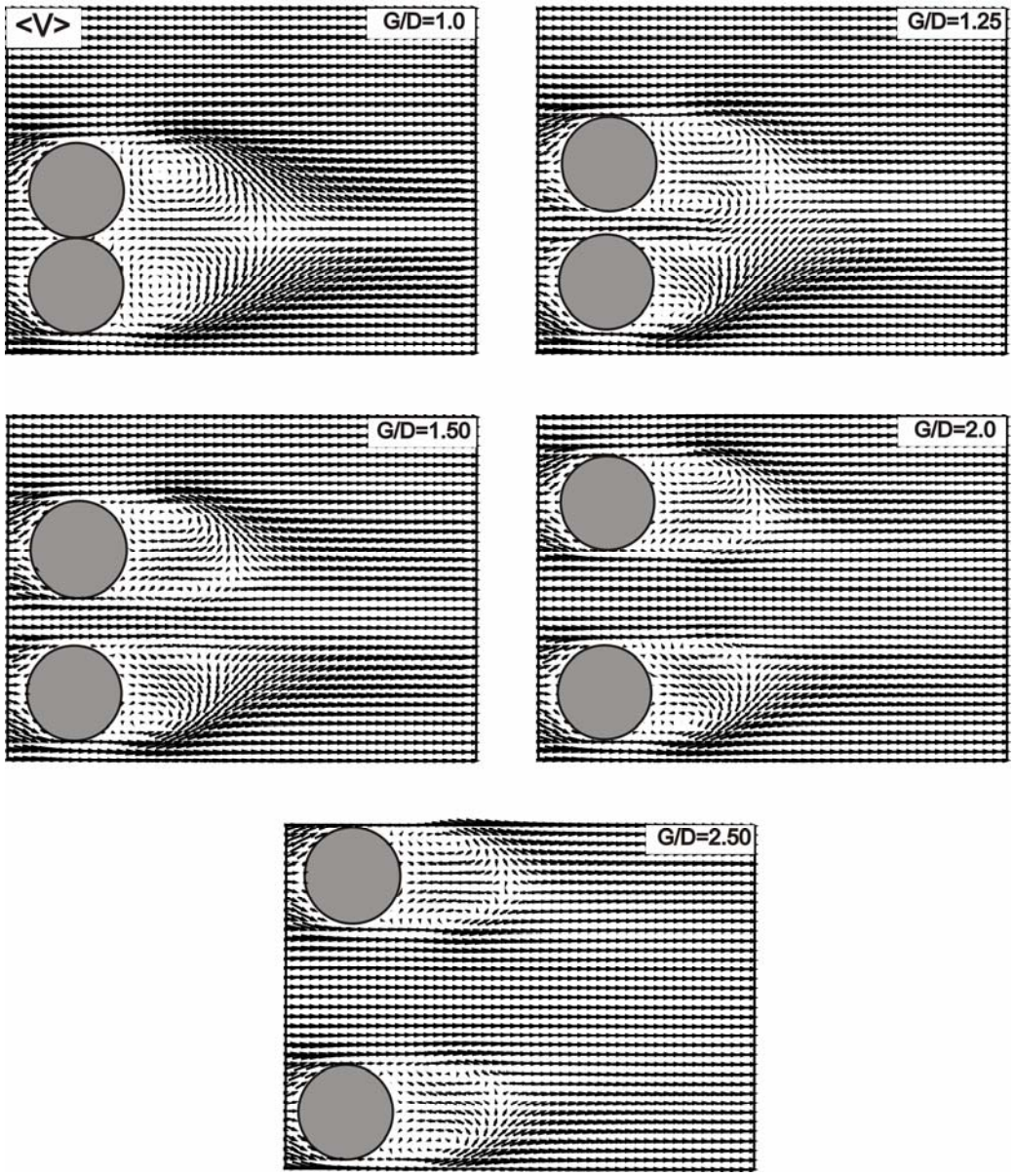


Figure 4.18. Patterns of time-averaged velocity vector, <V> of two side by side spheres for the gap ratios of G/D=1.00, 1.25, 1.50, 2.00, 2.50, Re=5000.

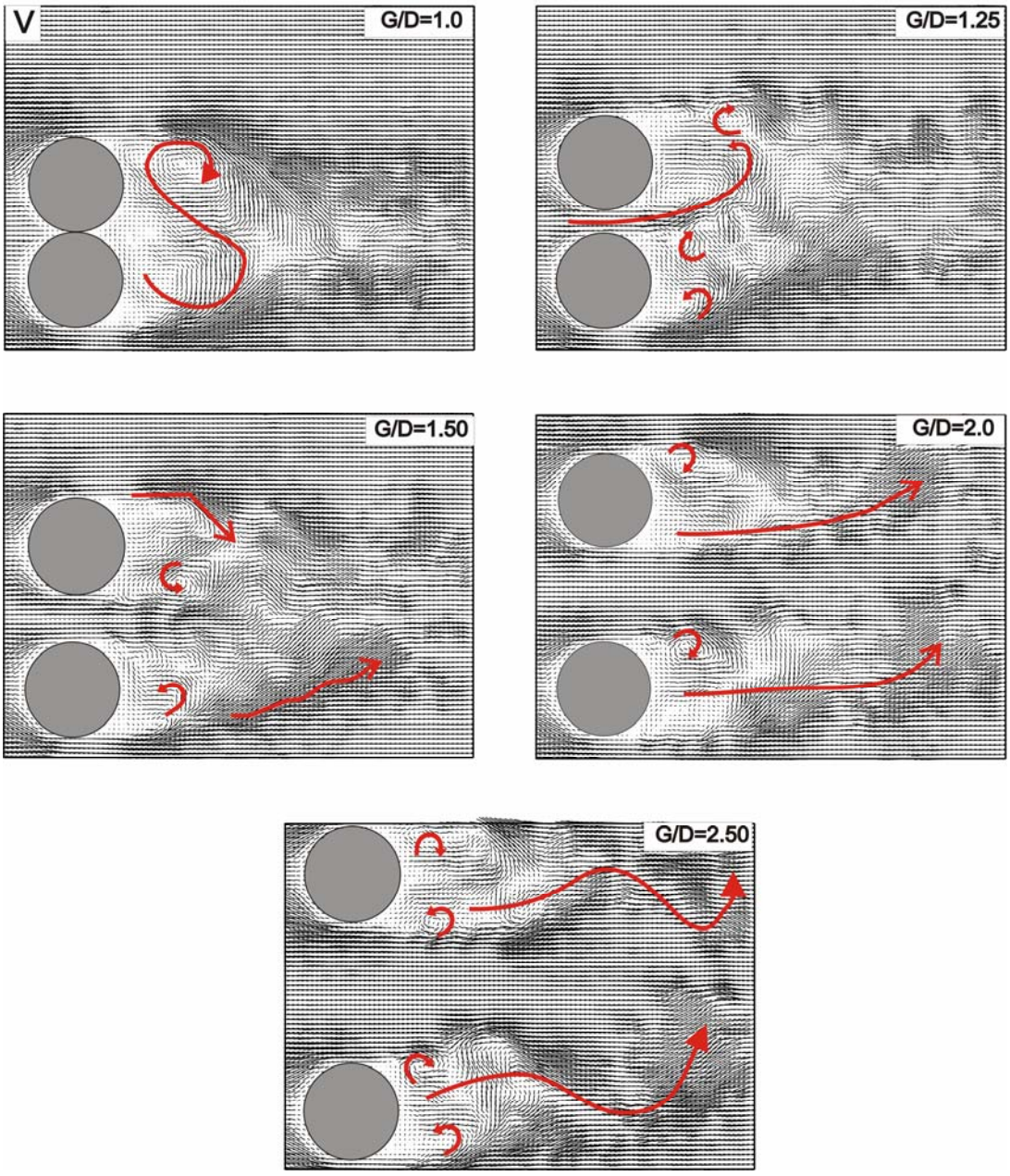


Figure 4.19. Patterns of instantaneous velocity vector, V of two side by side spheres for the gap ratios of G/D=1.00, 1.25, 1.50, 2.00, 2.50, Re=5000.

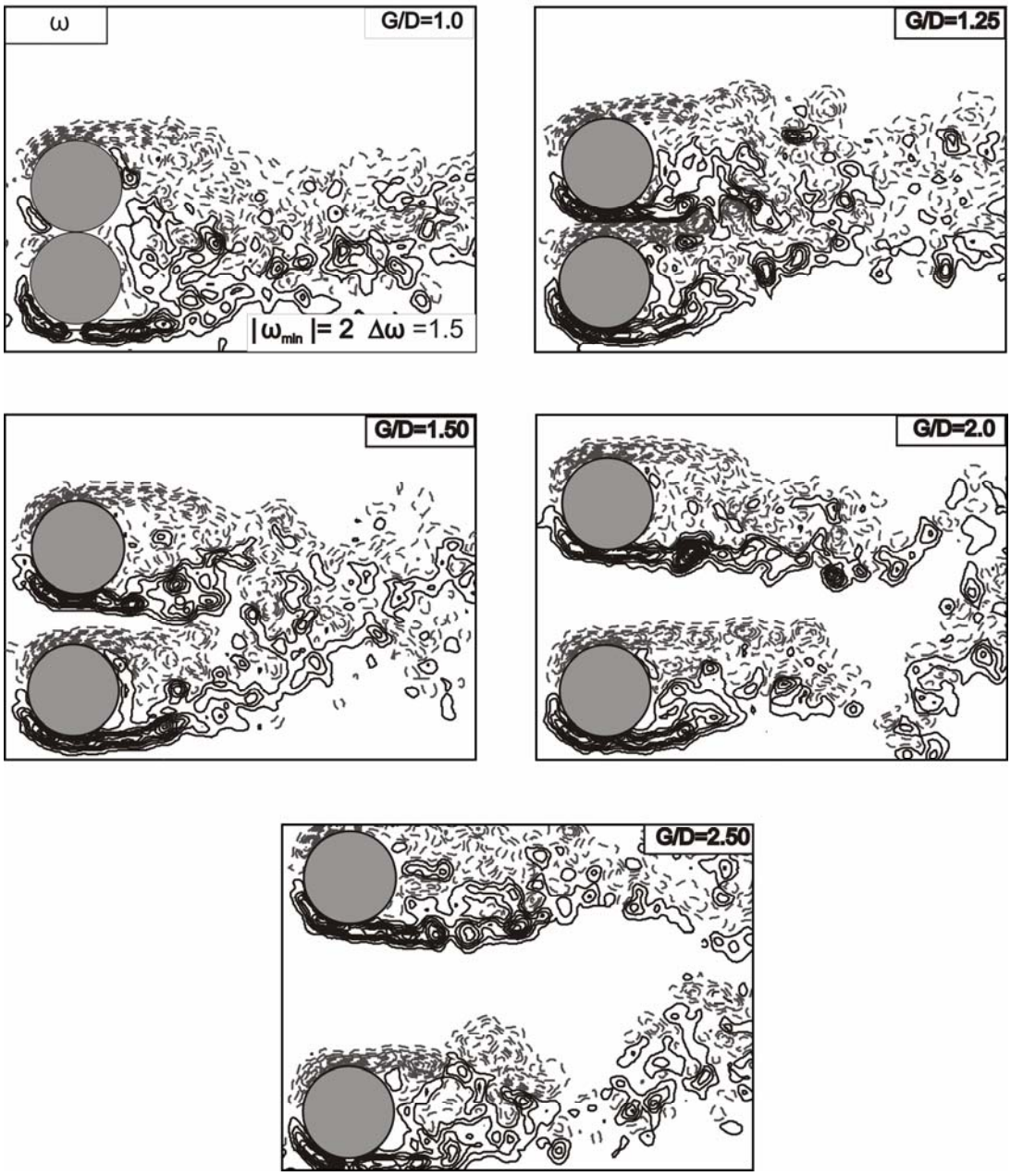


Figure 4.20. Patterns of instantaneous vorticity contours ω, $|\Delta_{min}|$=2 of two side by side spheres for the gap ratios of G/D=1.00, 1.25, 1.50, 2.00, 2.50, Re=5000.

Patterns of the time-averaged streamline, $\langle\psi\rangle$ presented in Figure 4.21 and fourth image of Figure 4.16 reveal information about size of wake region. However, these figures show the oblique angle of jet-like flow between two spheres, saddle points, S and foci, F of the vortex. The junction point of the streamlines separated from the surface of the sphere represented with "S". This junction point is called as

Saddle point, S which shows the merging point of shear layers emanating from both sides of sphere. Locations of foci which represented with "F" show that there is a focus point which rolled in the clockwise direction on upper side of the sphere central axis whereas focus located on the bottom side of the sphere central axis rolled in counter clockwise direction. It can be concluded that the flow around spheres is three dimensional.

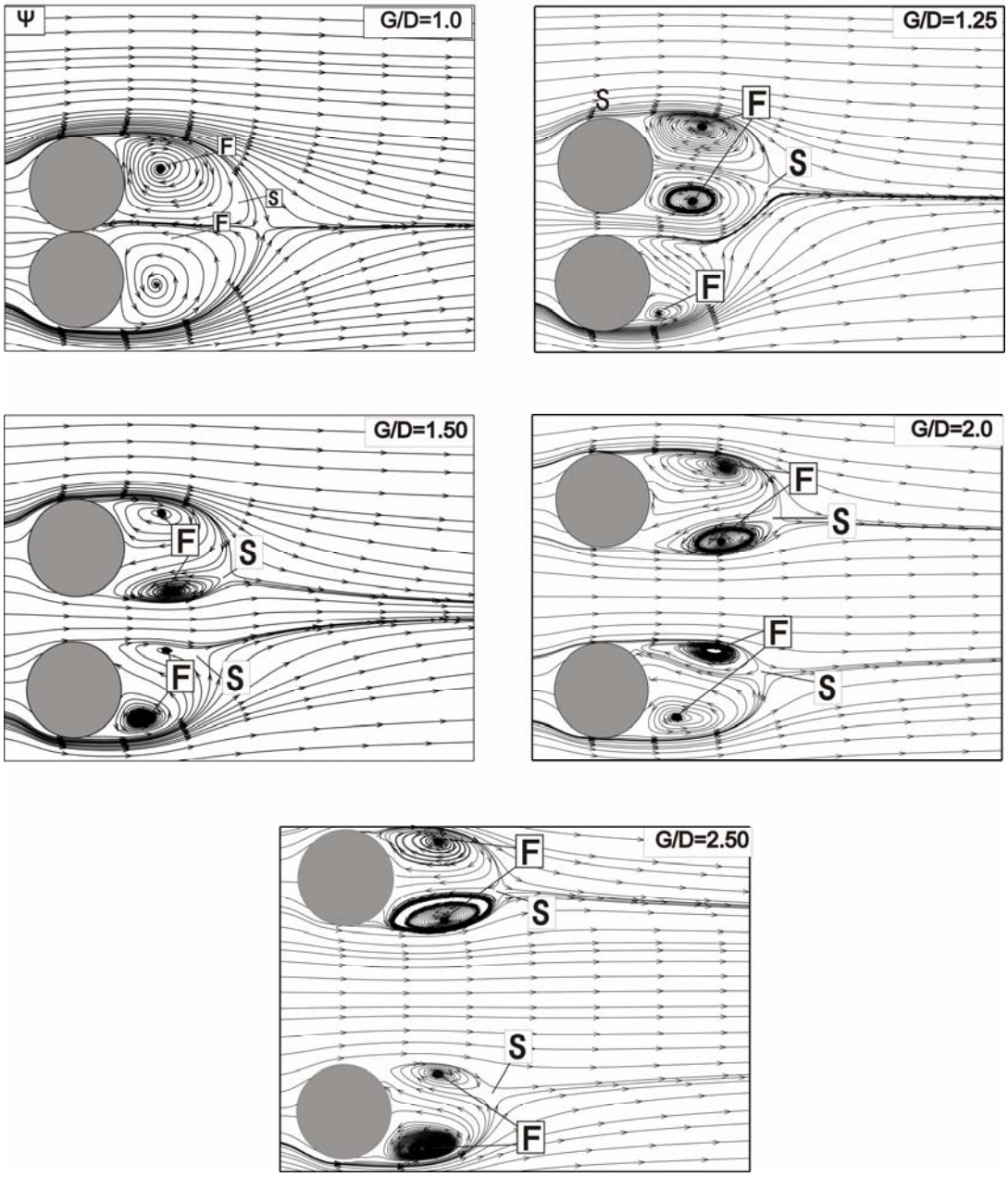


Figure 4.21. Patterns of time-averaged streamlines, <Ψ> of two side by side spheres for the gap ratios of G/D=1.00, 1.25, 1.50, 2.00, 2.50, Re=5000.

As seen in Figure 4.21, in the case of G/D=1.0, there is a symmetrical flow over spheres similar to the case of single sphere. This symmetrical flow structure deteriorates with the effect of the jet-like flow between spheres after G/D=1.00 and in the cases of G/D=1.25 and G/D=1.50 the larger wake region is developed on the upper side sphere compared with lower side one. The time-averaged Reynolds stress contours, $u'v'/U_\infty^2$ presented in Figure 4.22 and the second image on the first row Figure 4.17 indicate that there is no symmetrical flow structure over spheres due to the $u'v'/U_\infty^2$ effect of high rate of fluctuations caused by three dimensional flow structures in the wake region of the sphere. The alteration of the time-averaged contours of Reynolds stress correlations increase in the side by side arrangement and their symmetry also deteriorate. Since the value of Reynolds stress is zero on the central axis of sphere(s) both for cases of single sphere and two attachment spheres G/D=1.00, but this symmetry is altered after G/D=1.25. In the case of G/D=1.25, the values of negative stresses considerably increase compared with positive ones. These values are approximately same for the cases of other gap ratios.

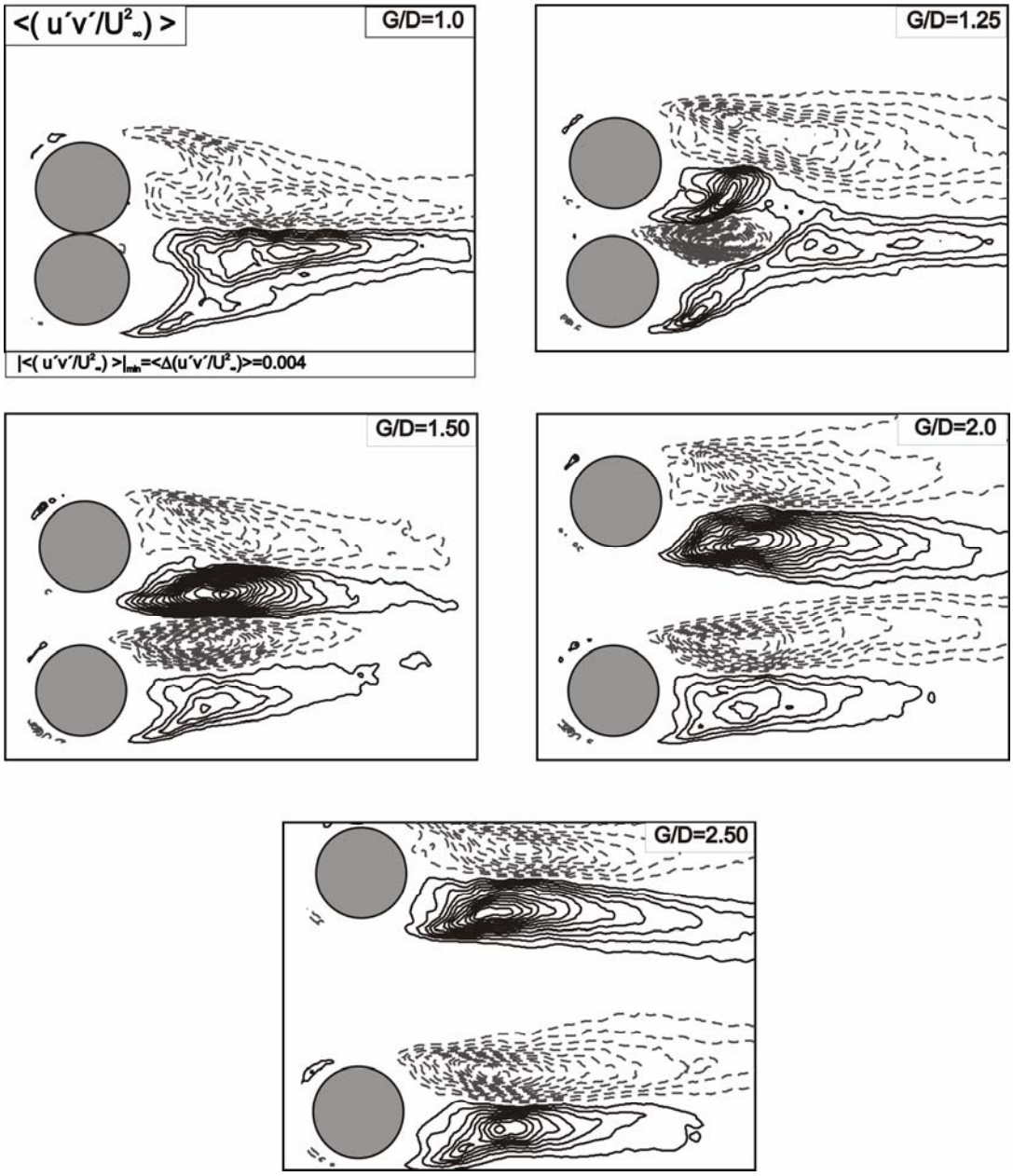


Figure 4.22. Patterns of Reynolds stress contours, $| < (u´v´/U^2)_{min}>| = 0.004$ $<\Delta(u´v´/U^2)>=0.004$ of two side by side spheres for the gap ratios of G/D=1.00, 1.25, 1.50, 2.00, 2.50, Re=5000.

The patterns of root mean square of the streamwise velocity component, $<u_{rms}/U>$ are given in Figure 4.23 and in the third image of Figures 4.16. Since the maximum value of fluctuation is 0.3, it decreases to a value of 0.26 in the case of touching spheres and because of the effect of the jet-like flow between spheres when the gap between spheres is expanded this value is measured as 0.44 for example in

the case of G/D=1.25. It can be seen that the $<u_{rms}/U>$ attenuates with increasing the G/D. The patterns of root mean square of the transverse velocity component, $<u_{rms}/U>$ are given in Figure 4.24 and in the fourth image of Figures 4.17. The maximum value of fluctuation is determined as 0.3. Although, the value of fluctuation of streamwise velocity component is decreased the maximum value of fluctuation of transverse velocity reaches to a value of 0.36 in the case of G/D=1.0. It can be stated that the transverse velocity fluctuations do not vary with the gap ratio anymore based on contours of transverse velocity component.

The patterns of time averaged dimensionless vorticity contours, <w> are shown in Figure 4.24 and in the first image of Figures 4.17. It is seen that there is uniform and symmetrical flow structure in the case of single sphere due to the balancing of the time-dependent small positive and negative eddies in the wake region of the sphere. Especially immediately after the sphere, since positive and negative eddies are in strong interaction with each other the time averaged vorticity values are approximated zero. The positive and negative contours exhibit symmetrical flow structure in the case of touching spheres, together with that the maximum value of positive and negative contours decrease compared with the case of single sphere. After G/D=1.25, symmetry of the flow structure deteriorate and the size of wake region of the lower side sphere decreases compared to upper one's. In the images of G/D=2.50, It can be seen that there is a similar flow structure of the case with single sphere for G/D=2.50

It can be seen that there are small scale Kelvin Helmholtz vortices in the wake region of the sphere. But, there is a momentum transfer towards to the wake region of the sphere because of the low pressure characteristics of the wake region far from the sphere. This physical structure causes the velocity difference between uniform flow region and wake region, especially instabilities in the free shear layer. These unstable structures are clearly seen in the dye visualization results in Figures 4.14 and 4.15 and instantaneous velocity results in Figures 4.16 and 4.18. The fluctuating form of small scale instantaneous vortices and velocity vectors indicate that the wake region behind sphere is 3 dimensional. To obtain this type of flow structure from computational studies and ability to prove their reliability could be possible only to

compare corresponding experimental results. This unstable flow structure develops Karman vortex streets which can be frequently seen in the wake region of the cylinder, whereas in the wake region of the sphere Karman vortex streets can be seen after twice sphere diameter approximately. Strouhal number (St) which is defines as the non dimensional value of the vortex frequency is determined approximately St=0.18 for Re=5000.

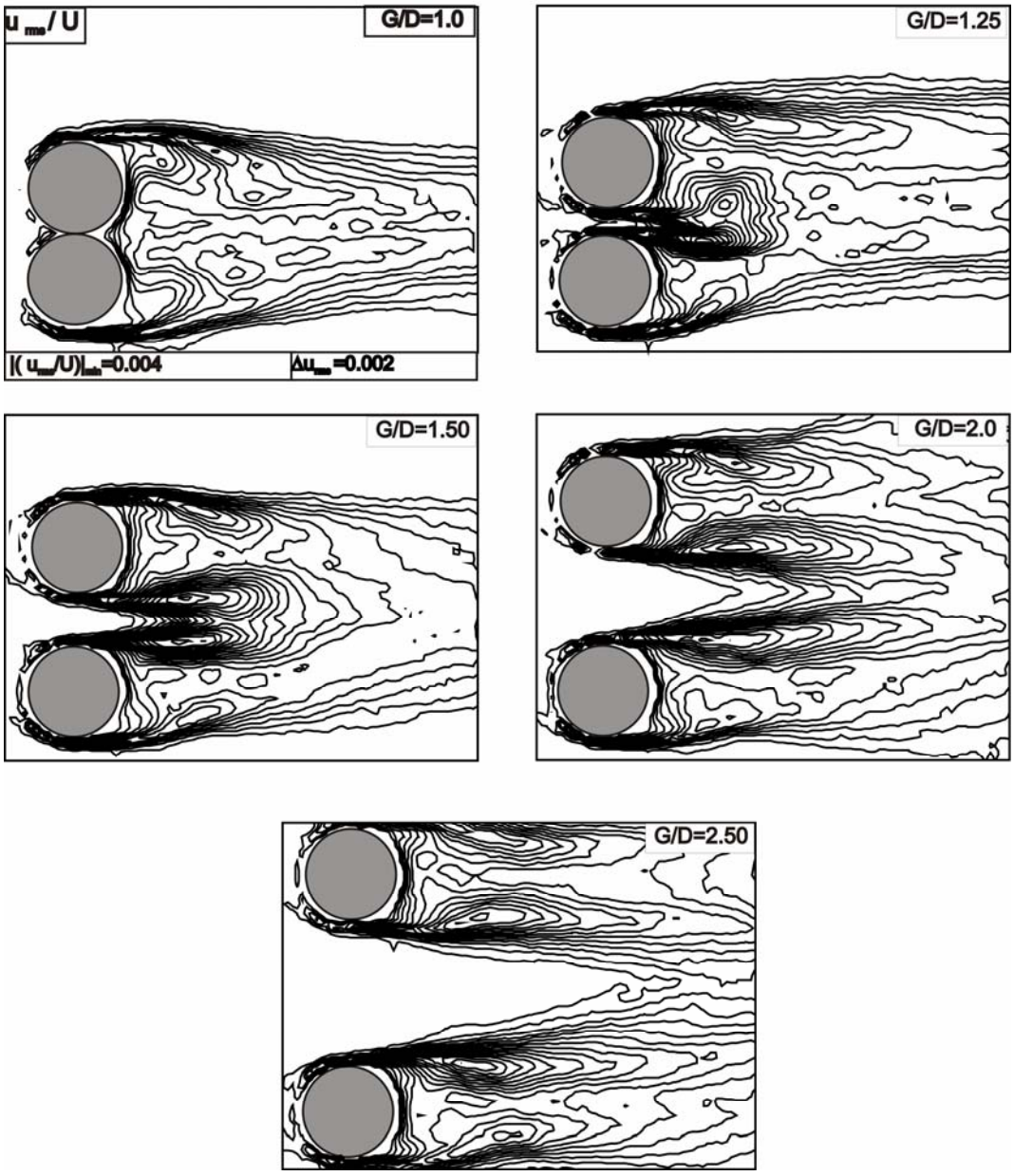


Figure 4.23. Patterns of square root of streamwise velocity, $<(U_{rms}/U)_{min}>$= 0.004, ΔU_{rms}=0.002 of two side by side spheres for the gap ratios of G/D=1.00, 1.25, 1.50, 2.00, 2.50, Re=5000.

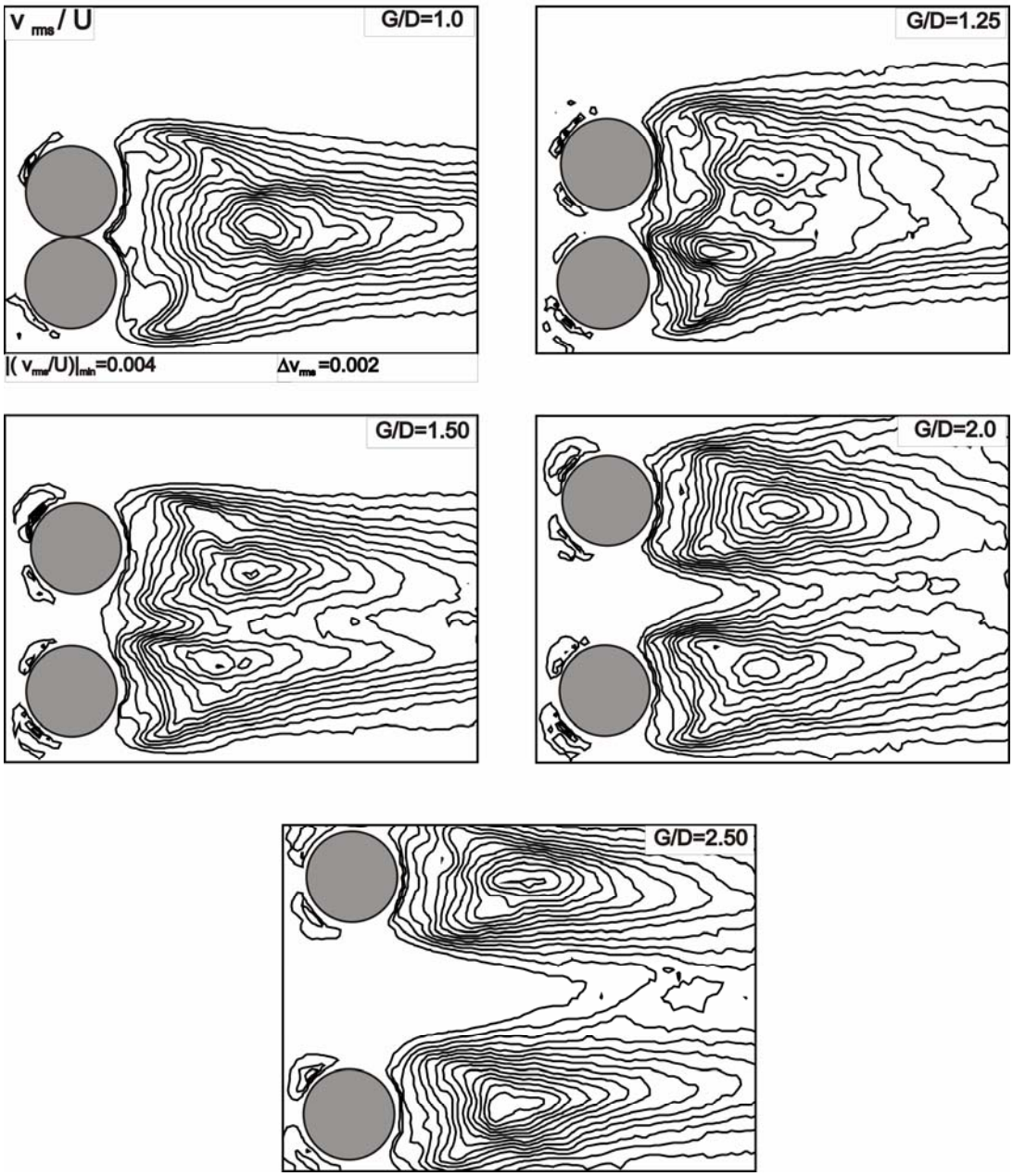


Figure 4.24. Patterns of square root of transverse velocity, $<(V_{rms}/U)_{min}>$= 0.004, ΔV_{rms}=0.002 of two side by side spheres for the gap ratios of G/D=1.00, 1.25, 1.50, 2.00, 2.50, Re=5000.

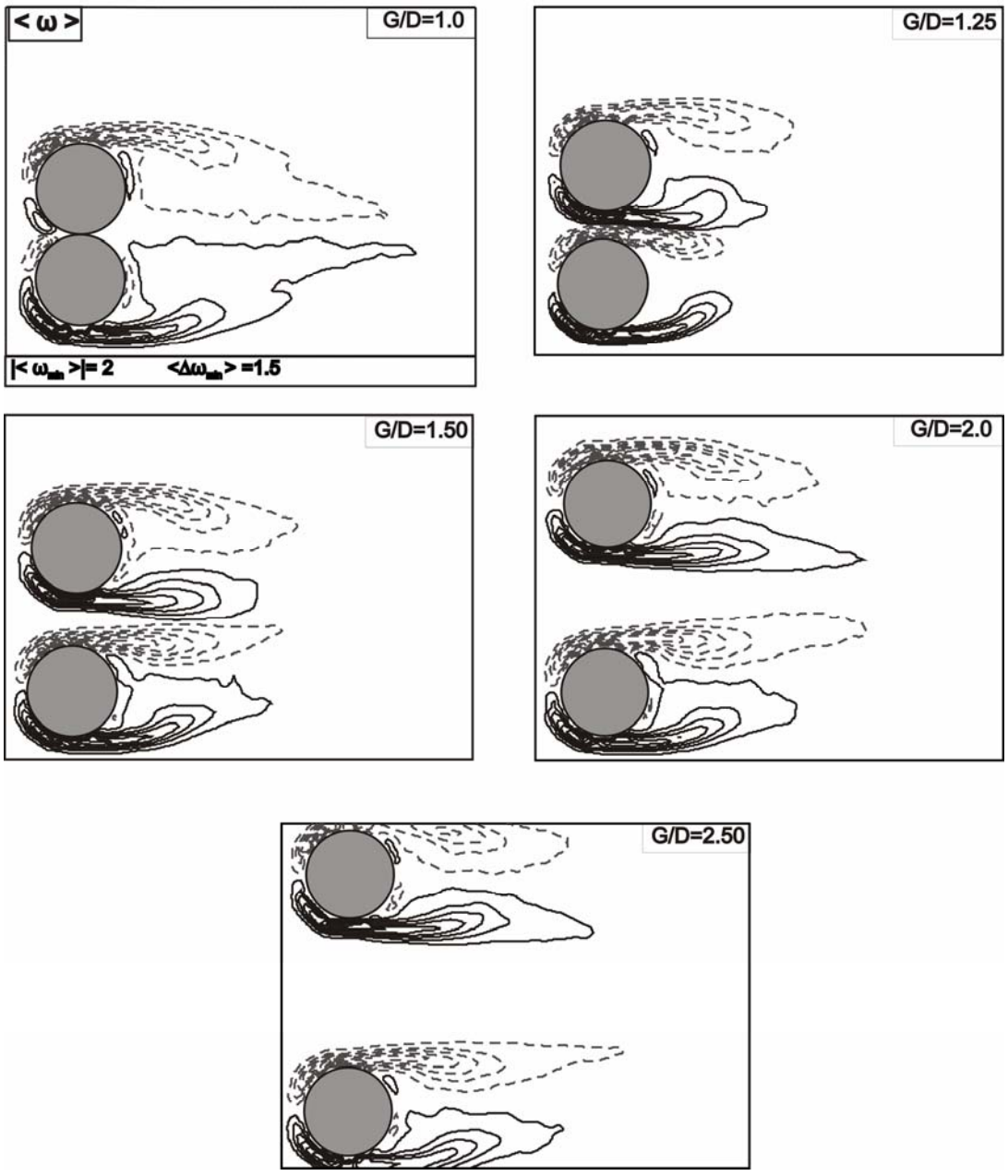


Figure 4.25. Patterns of time-averaged vorticity contours $|<\omega_{min}>|= 2$, $<\Delta\omega>=1.5$ of two side by side spheres for the gap ratios of G/D=1.00, 1.25, 1.50, 2.00, 2.50, Re=5000.

The results of end-view experiments which were performed to be able to understand the three dimensional flow around sphere and instabilities in the wake region in detailed are given in Figures 4.26-19 for the case of single sphere and in Figures 4.30 and 4.37 for the case of two spheres. Examining the cinemas of the instantaneous vorticity contours shown in Figure 4.27, it is observed that these

vortices rotate about both their axis and measurement axis in counter clockwise direction. Small scale and high fluctuating vortex structure herein show the source of Kelvin Helmholtz instabilities. The magnitude of the small scale positive and negative vortices vary with time. It is observed that density and magnitude of the small scale positive and negative vortices decrease along the streamwise direction (from L/D=0.5 to L/D=3.0) in the wake region of sphere. It is understood from comparison of the images in Figure 4.26 and on the first row of Figure 4.16, the reason of reduction in the magnitude of vortices is the mass transfer between main flow region and wake flow region. The sphere is represented by dashed line on images which are given on the left hand column. As seen in the first two rows of the figure, time-dependent positive and negative vortices balance each other. Due to vortices emanating from the periphery of the sphere exhibit vortex shedding, time-average of these positive and negative vortices turn into two large vortices. Examining the time-averaged velocity vectors in Figures 4.26 and 20-23, reveals that the separated flow moves from inboard to outboard of the wake region up to L/D=1.5 and separated flow moves from outboard to inboard of wake region at L/D=1.5. Examining the images in Figures 4.27 and 18 for variation of time averaged and instantaneous vorticity contours with L/D, indicate that the structure at wake region does not change up to L/D=3.00, but after L/D=3.00 the size of wake region gets smaller. The patterns of streamlines in Figures 4.29 and 20-23 for L/D=0.5 and 0.75, spiral flow demonstrates that the flow downstream of the sphere is three dimensional. When images for L/D=1.5 are compared with plan-view images, this plane coincide with saddle point “s” which represent the merging point of the shear layers.

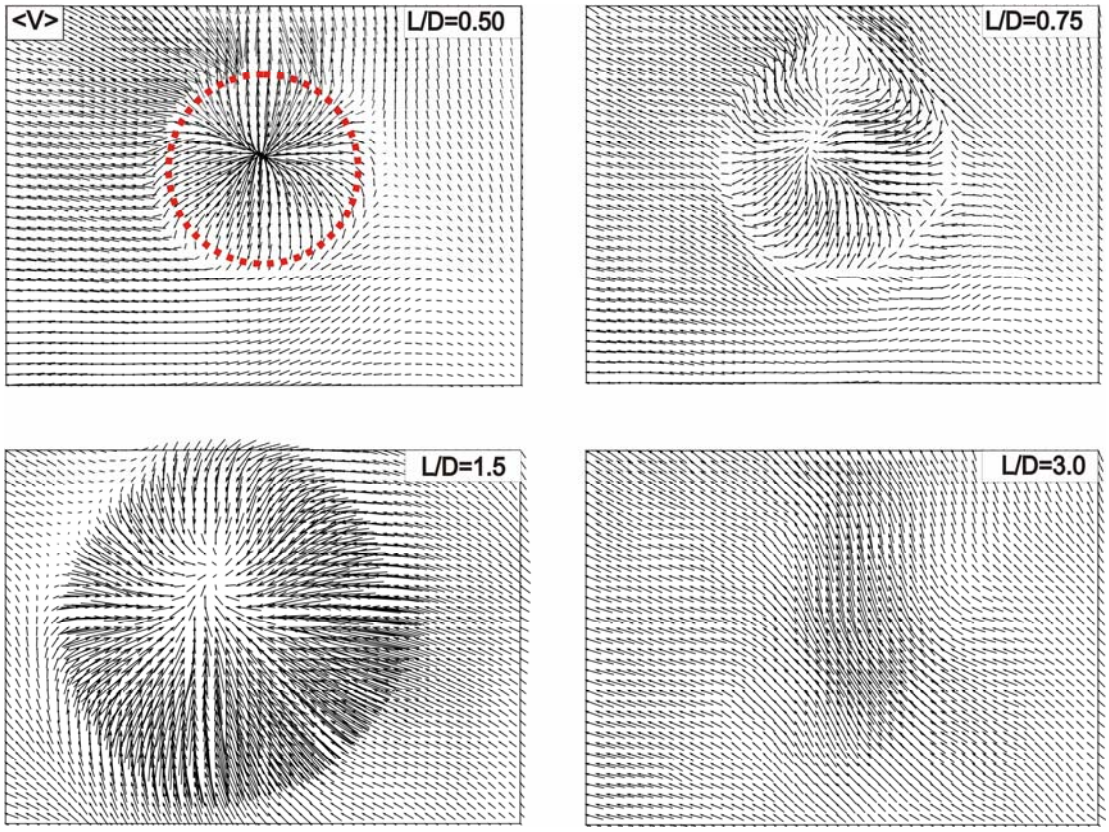


Figure 4.26. Patterns of time-averaged velocity vectors, <V> of the single sphere in end-view plane for length ratio of L/D=0.50, 0.75, 1.50, 3.0, Re=5000.

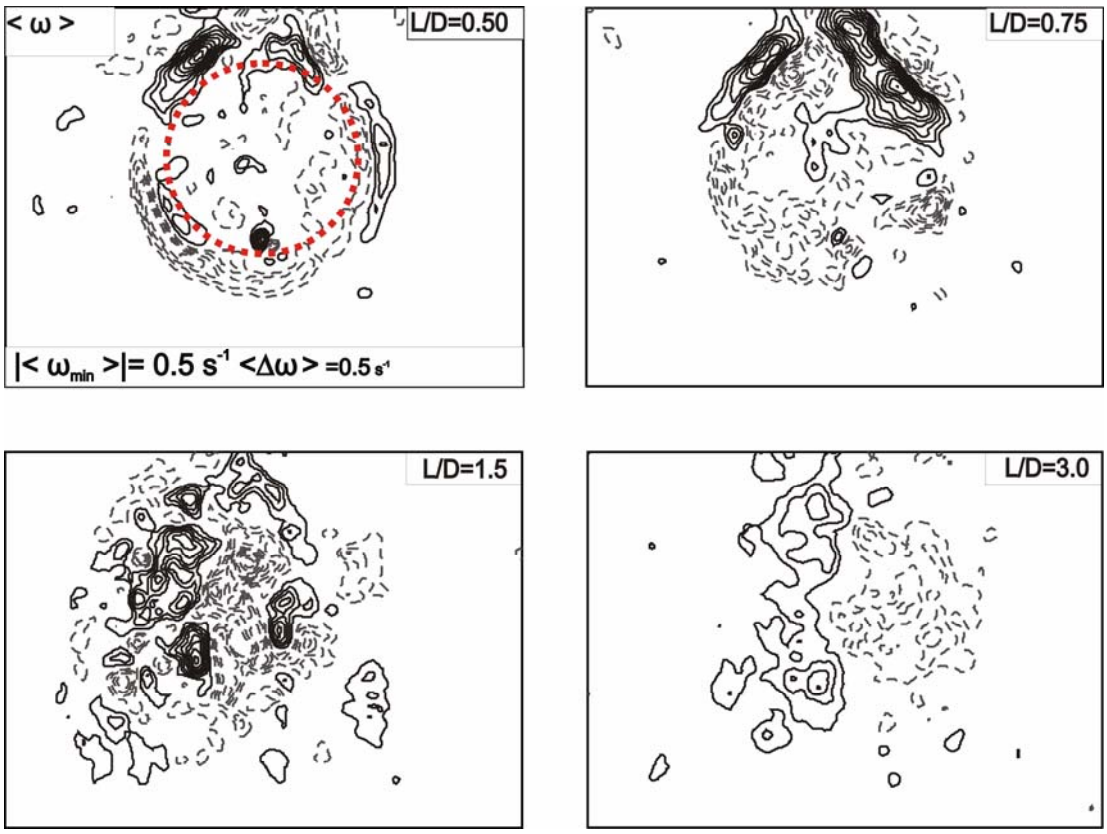


Figure 4.27. Patterns of time-averaged vorticity contours $|<\omega_{min}>|= 0.5$, $<\Delta\omega>=0.5$ of the single sphere in end-view plane for length ratio of L/D=0.50, 0.75, 1.50, 3.0, Re=5000.

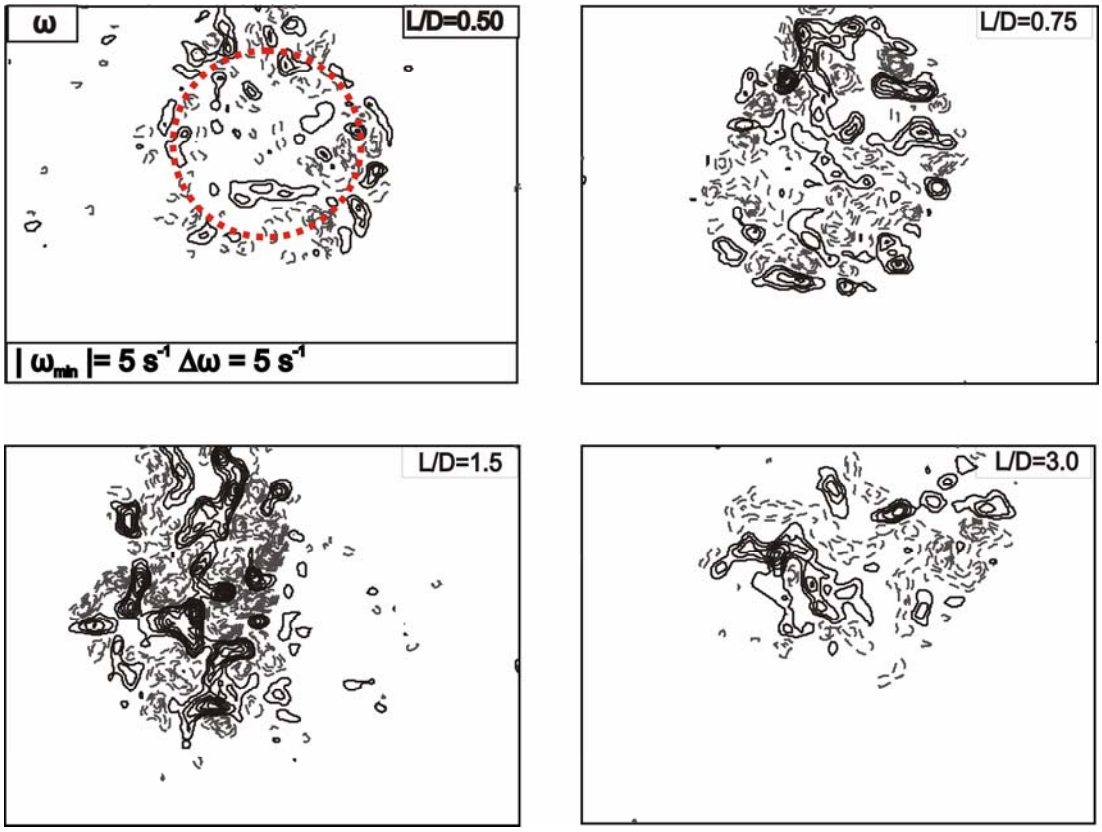


Figure 4.28. Patterns of instantaneous vorticity contours $|\langle\omega_{min}\rangle|= 5$, $\langle\Delta\omega\rangle= 5$ of the single sphere in end-view plane for length ratio of L/D=0.50, 0.75, 1.50, 3.0, Re=5000.

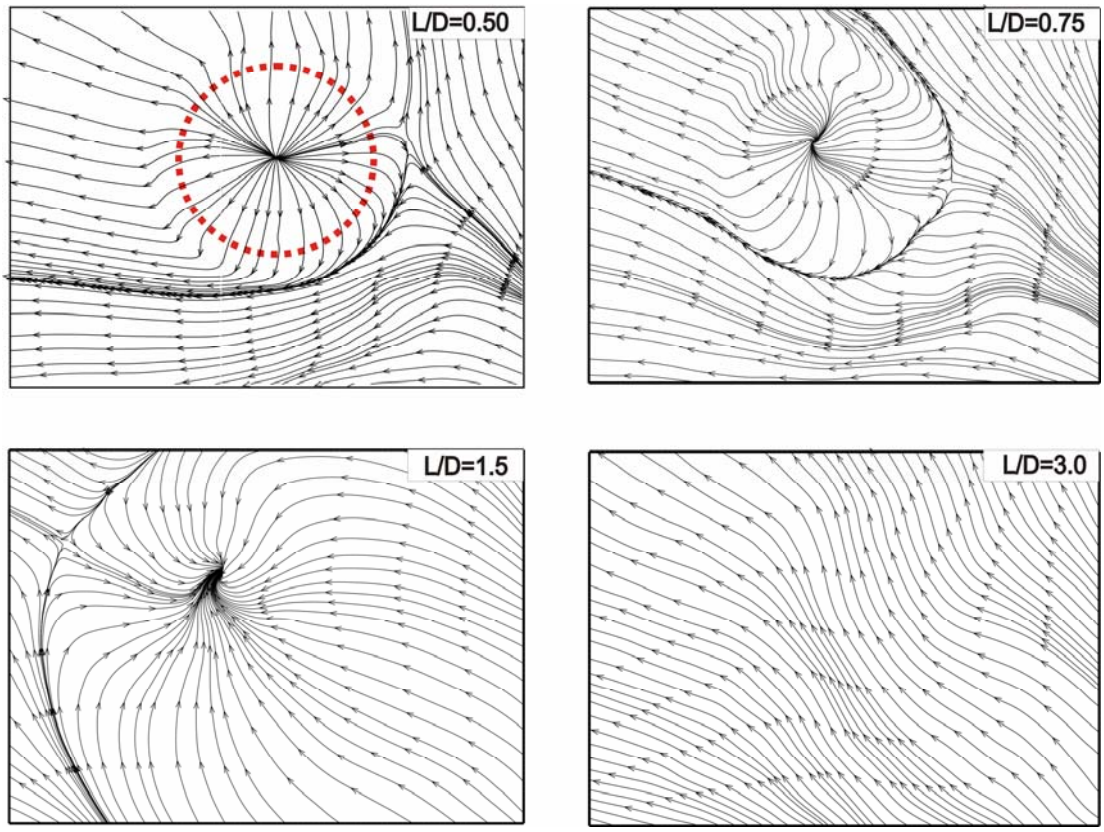


Figure 4.29. Patterns of time-averaged streamlines, Ψ of the single sphere in end-view plane for length ratio of L/D=0.50, 0.75, 1.50, 3.0, Re=5000.

It is seen that the spiral form of the wake region of two spheres in the case of the G/D=1.00 which resembles the wake region of single sphere maintains its structure approximately up to the value of L/D=1.50 which coincide with the saddle point, S. This spiral form of the wake region of spheres begin to attenuate after L/D=1.50 for all cases of gap ratios. Because of the jet-like flow between spheres, one of the wake regions of the sphere is greater and dominant comparing to the other one. As both mentioned in the dye visualization and PIV experiments in the plan-view plane, after G/D=1.50 each sphere have its own independent wake region which can be clearly seen in the end-view results. The magnitude of interaction between spheres gets lower for all cases of gap ratios after L/D=3.0. As seen in Figures 4.27 and 18, positive and negative vortices at immediately after sphere in the wake region interact and merge as they move through their wake region and produce

small scale vortices with low velocity after merging point. The reason is the velocity of the wake region reaches to free stream velocity as it moves further downstream.

At G/D=1.25, mass transfer due to the jet-like flow between spheres makes one of the wake region of the sphere greater and dominant comparing to the other one. This situation produces small wake region for lower sphere and larger wake region for upper sphere as seen in Figures 4.18-15. Because of variation of flow structure with time, the flow structure downstream of spheres has an unsteady motion. Comparing the end-view results in Figures 4.26-23 with the plan-view results in Figures 4.26-23 the small and large wake regions change their locations. This shows the time dependence and instability of the flow.

As seen in the patterns of streamlines, there is a nodal point on the surface of the sphere in the case of L/D=0.75. This situation is also true for cases of L/D=0.75 and 1.50, but interaction between spheres weakens at a value of L/D=3.0 due to existence of low pressure region in the wake flow region of spheres. Due to the side force of main flow region, the size of the wake flow region gets lower.

Images presented in Figures 4.26-19 and Figure 4.19 for G/D=2.0, L/D=3.0 are similar. Examining the experimental results for all cases of L/D, interaction between wake flow regions get lower as seen in images of G/D=2.0.

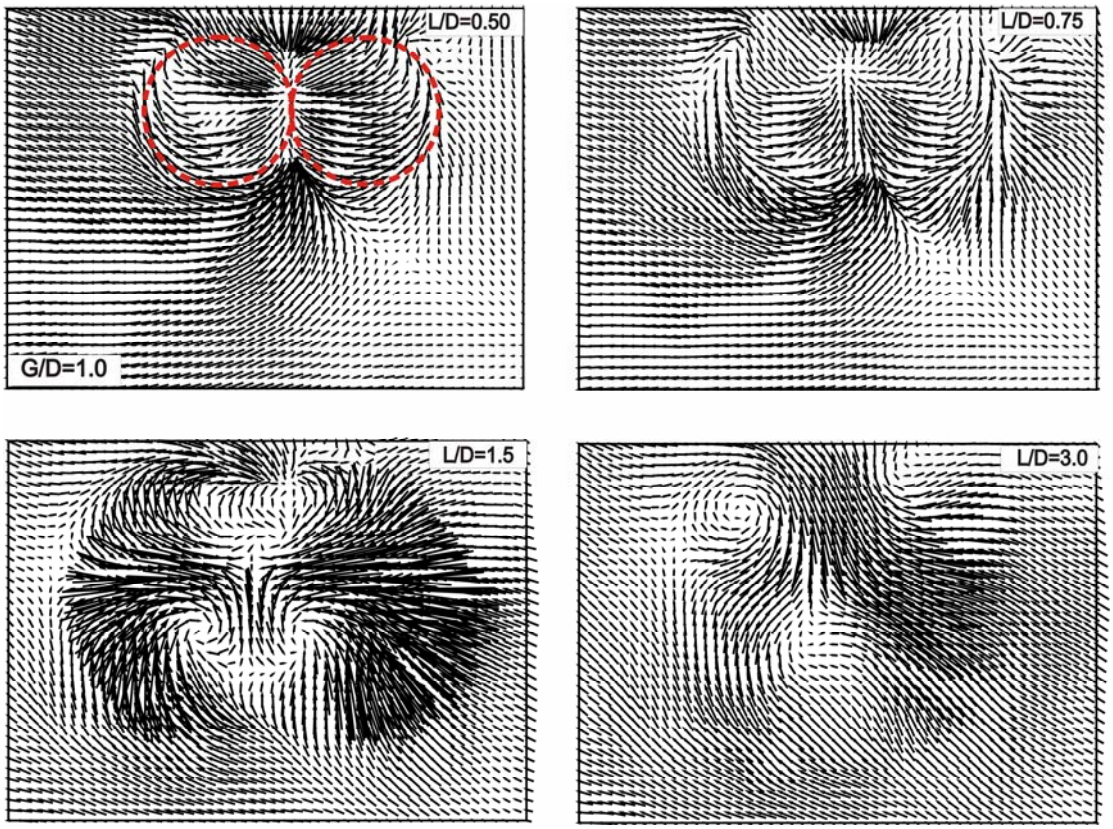


Figure 4.30. Patterns of time-averaged velocity vectors, <V> of the two side-by-side spheres in end-view plane for length ratio of L/D=0.50, 0.75, 1.50, 3.0 and gap ratio of G/D=1.0, Re=5000.

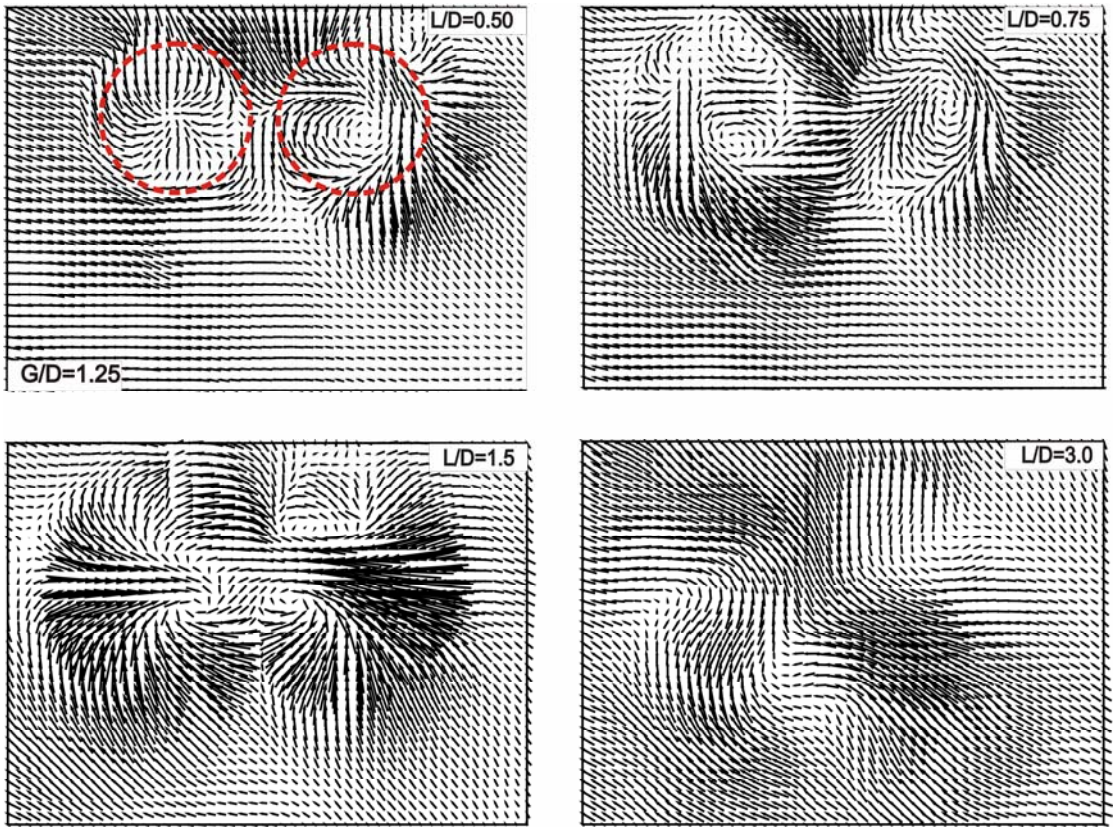


Figure 4.31. Patterns of time-averaged velocity vectors, <V> of the two side-by-side spheres in end-view for length ratio of L/D=0.50, 0.75, 1.50, 3.0 and gap ratio of G/D=1.25, Re=5000.

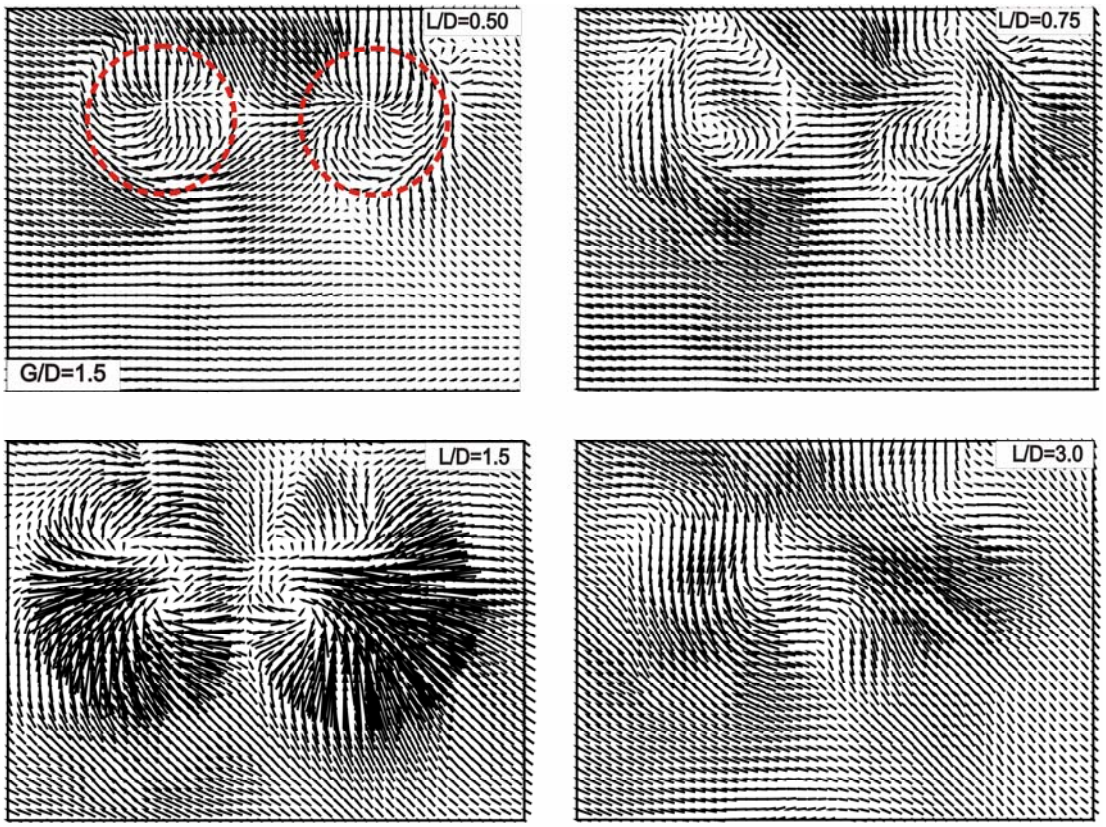


Figure 4.32. Patterns of time-averaged velocity vectors, <V> of the two side-by-side spheres in end-view plane for length ratio of L/D=0.50, 0.75, 1.50, 3.0 and gap ratio of G/D=1.50, Re=5000.

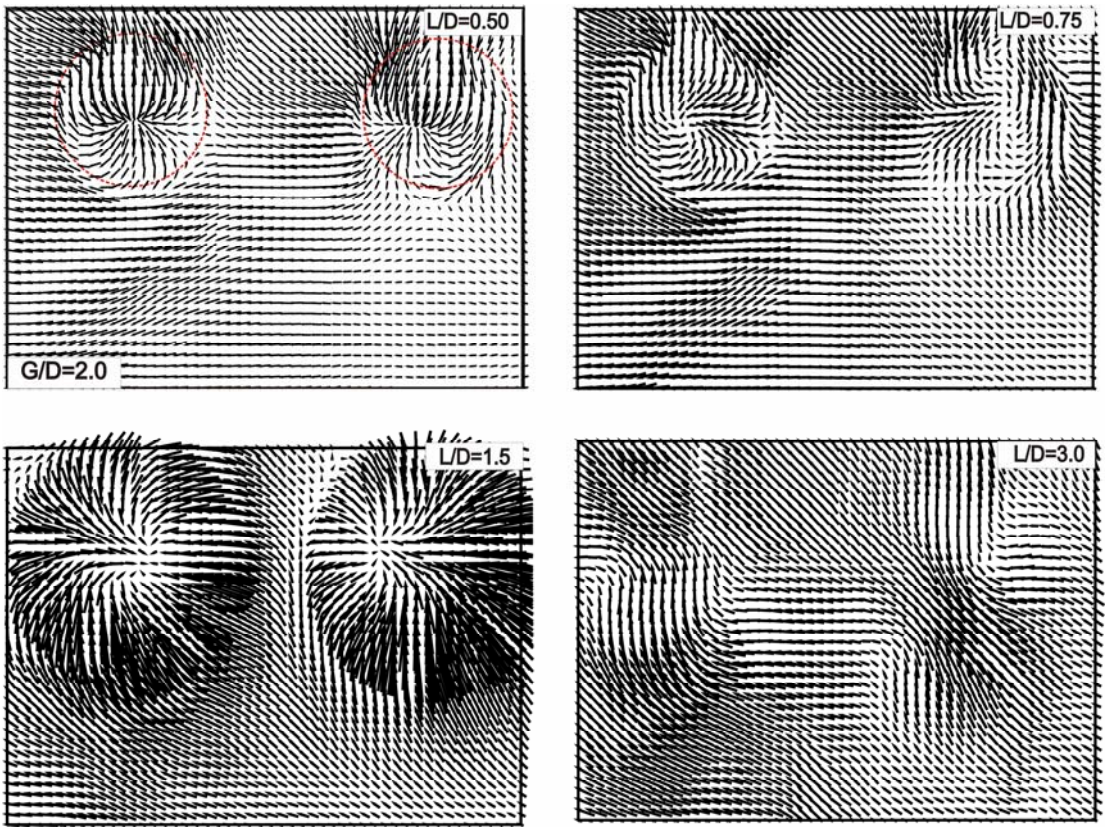


Figure 4.33. Patterns of time-averaged velocity vectors, <V> of the two side-by-side spheres in end-view plane for length ratio of L/D=0.50, 0.75, 1.50, 3.0 and gap ratio of G/D=2.00, Re=5000.

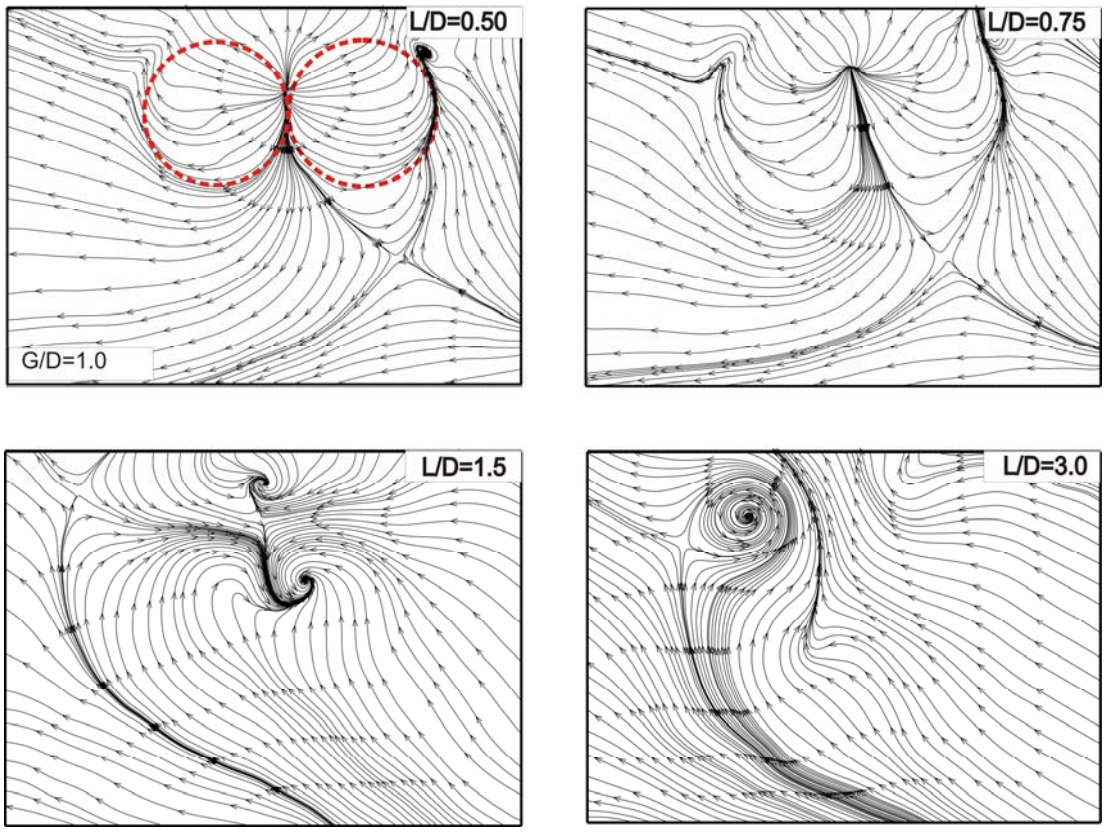


Figure 4.34. Patterns of time-averaged streamlines, Ψ of the two side-by-side spheres in end-view plane for length ratio of L/D=0.50, 0.75, 1.50, 3.0 and gap ratio of G/D=1.00, Re=5000.

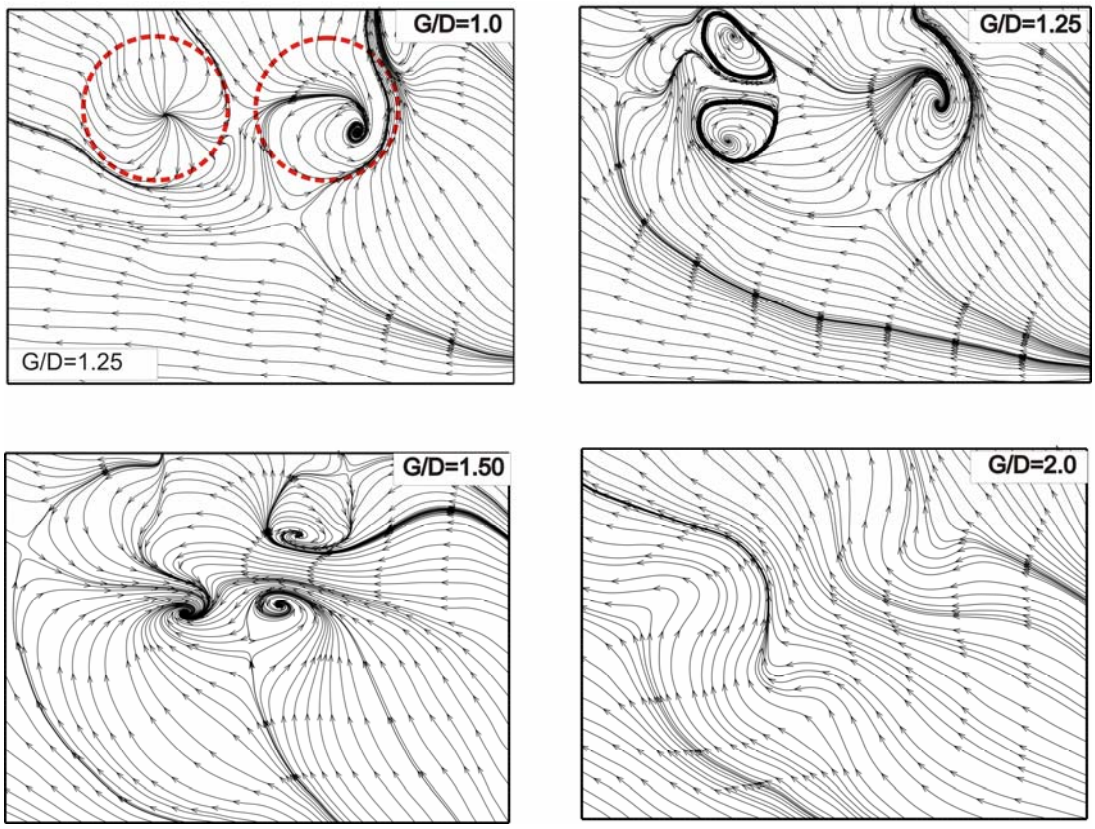


Figure 4.35. Patterns of time-averaged streamlines, Ψ of the two side-by-side spheres in end-view plane for length ratio of L/D=0.50, 0.75, 1.50, 3.0 and gap ratio of G/D=1.25, Re=5000.

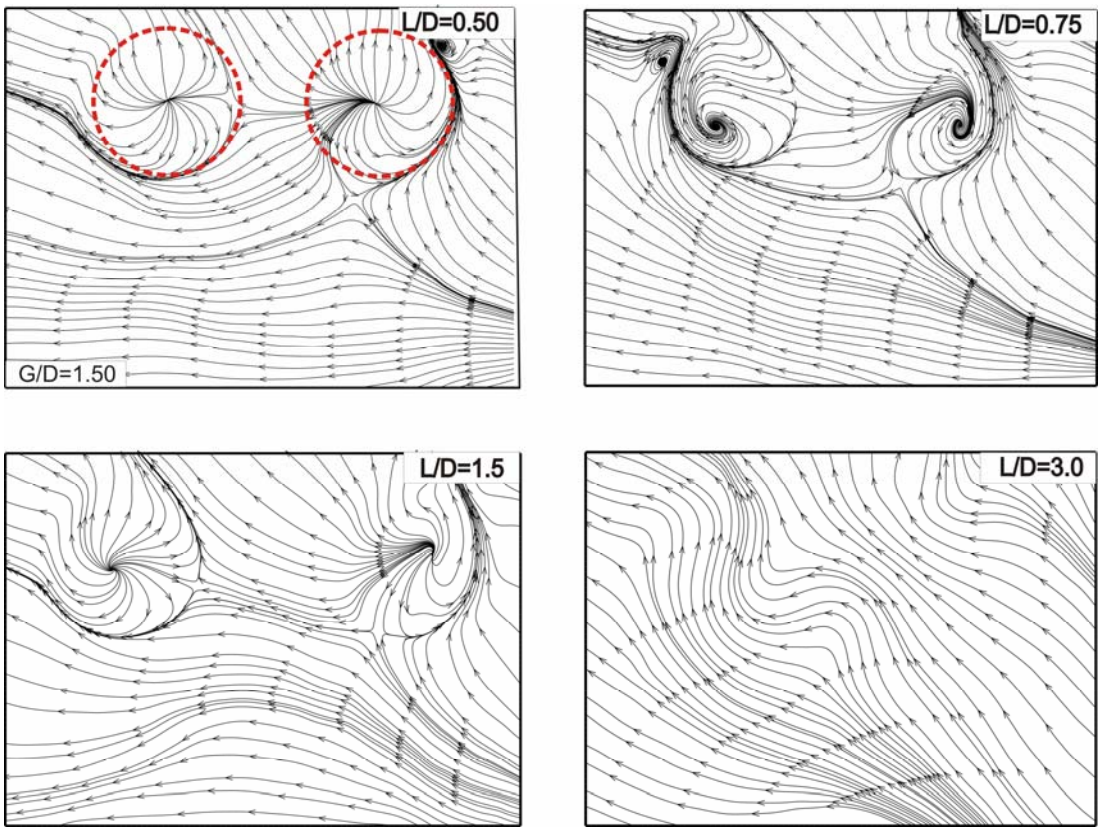


Figure 4.36. Patterns of time-averaged streamlines, Ψ of the two side by side spheres in end-view plane for length ratio of L/D=0.50, 0.75, 1.50, 3.0 and gap ratio of G/D=1.50, Re=5000.

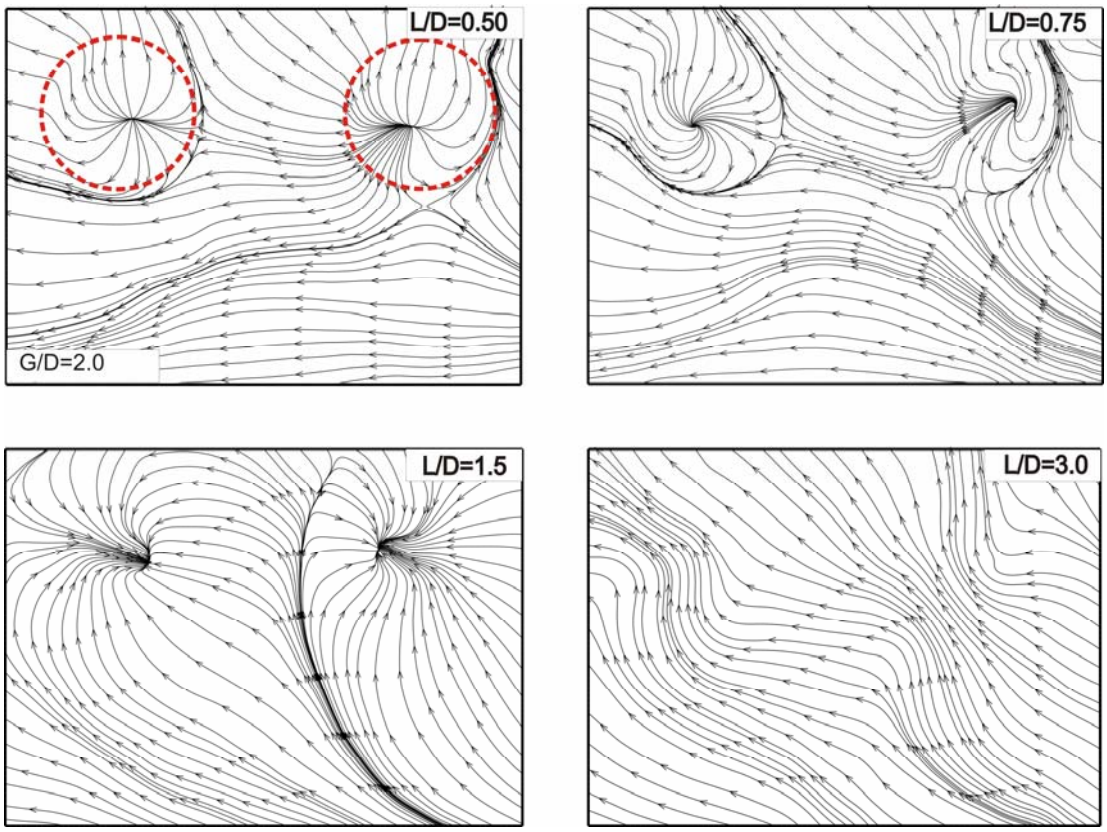


Figure 4.37. Patterns of time-averaged streamlines, Ψ of the two side-by-side spheres in end-view plane for length ratio of L/D=0.50, 0.75, 1.50, 3.0 and gap ratio of G/D=2.00, Re=5000.

5. CONCLUSIONS

Many studies both numerically and experimentally have been conducted to investigate the cylinder and sphere wake. However, the numerical models have a difficulty in validating their predicted results such as flow separation angle, recirculation length, and turbulence statistics due to lack of comparative experimental data. Therefore, more experimental results are needed to develop new numerical methods or improve existing numerical methods.

Interaction between sphere and flow alters the general characteristics of flow structure. This interaction cause more complex and unsteady flow characteristics in the case of side-by-side spheres. Instantaneous vorticities around sphere cause dynamic loadings and vibrations. There are many studies in the literature which investigate the flow structure over sphere and also interaction of flow and sphere. On the other hand, these studies were limited because of difficulties in studying the flow characteristics of wake flow region. Same reasons of this limitation are complexity of the flow structure which is caused by the three dimensional structure of sphere and supporting difficulty of a sphere in water channel or wind tunnel test section, large area of separated flow, and strong time dependency.

The first part of the present study focused on the generation of vortical structures of the near-wake region arising from the flow passing separately the cylinder and the sphere for Re=5000 in order to explain differences of the physical mechanisms of the flow structure between cylinder and sphere. The results are summarized as follows: PIV results of instantaneous velocity fields of the sphere and cylinder wake showed an unsteady vortex formation mechanism, that is, recirculation vortices were formed alternatively and were discharged downstream progressively. The present study has supported the previous works by providing detailed qualitative and quantitative experimental information in the near wake region of the aforementioned bluff bodies. It is observed that the wake is unstable with vortex shedding. The mean velocity field showed two peculiar large-scale recirculation vortices downstream of the sphere model, of which the length of the recirculation region was approximately one diameter in wake region. In the cross-sectional planes, a number of small longitudinal vortices with opposite signs were distributed

circumferentially around the sphere periphery and near the center of the recirculation vortices. The instantaneous vorticity fields revealed an unsteady wavy structure of the sphere wake. In the cross-sectional planes, the flow moving inward in radial direction was dominant, and the maximum strength occurred around the end of the recirculation region. The vortical flow structure in the near-wake of the sphere showed a wavy flow structure and the onset of shear-layer instability. Strouhal numbers for the cylinder and the sphere are determined as 0.21 and 0.18. The flow patterns are considerably symmetrical about the centerline of the cylinder and sphere of the flow patterns, as seen in all time-averaged images. Contours of the time-averaged streamwise velocity demonstrate that the stagnation point around the symmetry plane moves further upstream for the higher Reynolds number. The shear layer surrounding the recirculation bubble downstream of the cylinder has a region of intense velocity fluctuations with high values of Reynolds stress correlation because of the possibly 2D vortex interactions. However, concentration of small scale vortices (eddy) is more dominant in the wake of the sphere than that of the cylinder. In general, vortex formation lengths decrease with increasing the Reynolds number. Experimental data obtained in this study would enhance the understanding on sphere and cylinder wake and can be used for validating numerical simulations. Present results can provide sufficient information about the details of the foregoing flow features to develop a strategy for the validation of numerical models in future.

The second part of the present study focused on the vortical structure of the wake flow region of two side by side spheres both in plan-view and end-view plane for Re=5000 in order to understand formation and development of the flow structure. The results are summarized as follows: The flow characteristics due to the hydrodynamic interaction between sphere and free stream flow are investigated for Re=5000. It is found that increasing the gap ratio has profound effect on the wake region of spheres and symmetrical flow structure for the case of single sphere turns into asymmetric structure for the case of side-by side spheres. It is recorded that one of the wake region of sphere is larger than the other in an uncontrolled mode. The reasons for that situation are the three dimensional flow structure around sphere, the velocity of the jet flow between spheres is unstable and greater than the free stream

velocity. For the case of G/D=2.0, the flow around spheres are too similar to the case of single sphere. For all gap ratios, the spiral flow structure begins to deteriorate after L/D=0.50 and the interaction between flow over each sphere gets lower after L/D=3.0. By adjusting the gap between spheres, especially for drying process, the jet flow can be refreshed rapidly and this contributes the drying efficiency. Both the cases of single sphere and side by side sphere include small scale eddies. This eddies rotate about their axis and because of the instabilities in wake region they are highly in interaction mode. Small scale eddies and high rate of fluctuations in velocities which are developed over the equatorial plane of sphere presented in the end-view plane indicates interactions between fluid and sphere. It is considerably hard to predict these vortices using numerical methods and confirm reliability of obtained results. The present study provides data for the confirmation of the computational results and industrial applications.

REFERENCES

ACHEBACH, E., 1972. “Experiments on the flow past spheres at very high Reynolds numbers”. J Fluid Mech 54(3), p.565–575.

——— 1974.“Vortex shedding from spheres”, Journal of Fluid Mechanics, Vol. 62, Part 2, Jan 23, 209-221.

ADRIAN,RJ.,1991.”Particle-imaging techniques for experimental fluid mechanics.” Annu Rev Fluid Mech, Vol.23,p.261–304.

AKILLI, H., AKAR, A., and KARAKAUS, C., 2004, “Flow Characteristics of Circular Cylinders Arranged Side-By-Side in Shallow Water,” Flow Meas. Instrum., 15, pp. 187–197.

ALASSAR, R.S., AND BADR. H.M., 1997. “Oscillating Viscous Flow Over A Sphere,” Computers&Fluids, Vol.26, No.7, pp.661-682.

BALACHANDAR S, MITTAL R, NAJJAR FM., 1997. “Properties of the mean recirculation region in the wakes of two-dimensional bluff bodies,” J Fluid Mech. Vol.351, p.167–99.

BARKER, J.M., GARDNER, S.M., AND LIBURDY J.A., 1997.”Low Reynolds number near wake flow of a sphere,” ASME, FED Fluid Measurement and Instrumentation, vol 211, p 45-50.

BLOOR, M.S., 1964. “The transition to turbulence in the wake of a circular cylinder.” Journal of Fluid Mechanics, 19: 290-304.

CHEN, R.C., AND WU, J.L., 2000. “The flow characteristics between two interactive spheres”, Chemical Engineering Science 55, 1143-1158, 2000.

CONSTANTINESCU, GS., AND SQUIRES, KD., 2003. “LES and DES investigation of turbulent flow over a sphere at Re=10,000”, Flow Turbulence Combust, Vol.70, p.267–298.

——— 2004. “Numerical investigations of flow over a sphere in the subcritical and supercritical regimes.” Phys Fluids Vol.16, Issue.5, p.1449–1466.

FOURAS, A., AND SORIA, J., 1998. “Accuracy of out-of-plane vorticity measurements derived from in-plane velocity field data”. Exp Fluids, Vol.25, p.409–30.

GERRARD, J.H., 1978. “The wakes of cylindrical bluff bodies at low Reynolds number”. Phil. Trnas R. Soc. London A, 288: 351-382.

GIWOONG, Y., DONGJOO, K., AND HAECHEON, C., “Vortical Structures Behind A Sphere at Subcritical Reynolds Numbers”, Phys. Fluids, Vol.18, Issue 1, pp.1-14, 2006.

HADZIC I., BAKIC´ V., PERIC´ M., SAJN V., KOSEL F., 2002. “Experimental and numerical studies of flow around sphere at sub-critical Reynolds number”. Eng Turbulence Model Exp, Vol.5, p.667–676.

JEON, J., CHOI, J., WOO-PYUNG JEON, HAECHEON C., AND JINIL P., 2004. “Active control of flow over a sphere for Drag Reduction at a Subcritical Reynolds number”, J. Fluid Mech. vol. 517, p.113–129.

JOHNSON TA., AND PATEL VC., 1999. Flow past a sphere up to a Reynolds number of 300. J Fluid Mech, Vol.378, p. 9–70.

KEANE, RD., AND ADRIAN, RJ., 1989. “Optimization of particle image velocimeters”. Opt. Methods Flow Particle Diagnostics Vol.68, p.139–59.

KIM HJ., AND DURBIN, PA., 1988. „Observations of the frequencies in a sphere wake and of drag increase by acoustic excitation”, Phys Fluids Vol.31, issue.11, p.3260–3265.

KIM, I., AND PEARLSTEIN, A.J., 1990 Stability of the Flow Past A Sphere,Journal of Fluid Mechanics, vol. 211, Feb, p 73-93.

LIN, J-C, TOWFIGHI, J, AND ROCKWELL, D., 1995 “Instantaneous structure of near-wake of a cylinder: on the effect of Reynolds number”. J Fluids Struct,Vol.9, p.409–18.

MEHTA, D., 1985. “Aerodaynamic of Sport Balls”, Ann. Rev., Fluid Mechs, Vol. , 17:151-89.

NOCA, H.G. PARK, AND M. GHARIB., 1998. “Vortex formation length of a circular cylinder (300<Re<4000) using PIV”, Proceedings of FEDSM’98, June 21-25, Washington, DC, p.1-7.

OZGOREN, M., B. ŞAHIN., H. AKILLI., C. KARAKUŞ., S. YAYLA., A. ÖZTÜRK., AND A. AKAR., 2006 “Küre Etrafındaki Akış Yapısının Parçacık

Görüntülemeli Hız Ölçme Yöntemiyle İncelenmesi," UHUK 06-028, ODTÜ Ankara.

OZGOREN, M., B. ŞAHIN., PINAR, E., H. AKILLI., 2009 (Unpublished) "Experimental Investigation of Flow Structure Around a sphere and cylinder via Flow Visualization," AIAC- 09-012 , ODTÜ Ankara.

CHEN R.C.., AND Y.N. LU., 1999. "The Flow Characteristics of an Interactive Particle at Low Reynolds Numbers", International Journal of Multiphase Flow, 25, 1645-1655.

Ryu, K.W., and Lee, D.J., 1997. "Interaction between a Vortex Ring and a Rigid Sphere" European Journal of Mechanics, B/Fluids, V.16, N.5, , p.645-664.

SAHIN B., OZTURK N.A., AND AKILLI H., 2007. "Horseshoe vortex system in the vicinity of the vertical cylinder mounted on a flat plate", Flow Measurement and Instrumentation, Vol. 18, p.57–68.

SAHIN B., AND OZTURK N.A., 2009. "Behavior of flow at the junction of cylinder and base plate in deep water, Measurement", Vol. 42, p.225–240.

SAKAMOTO H, HANIU, H. A., 1990. "Study on vortex shedding from spheres in a uniform flow". J Fluids Eng Vol.112, p.386–392.

SCHOUVEILER, L., A. BRYDON, T., LEWEKE AND M.C., 2004. Thompson, "Interactions of the wakes of two spheres placed side by side," European Journal of Mechanics B/Fluids, Vol.23, 137–145.

TANEDA, S., 1978. "Visual observations of the flow past a sphere at Reynolds numbers between 104 and 106", Journal of Fluid Mechanics, Vol. 85, 187-192.

THOMPSON, M. C., LEWEKE, T. AND PROVANSAL, M., 2001. "Kinematics and dynamics of sphere wake transition", Journal of Fluids and Structures, Vol.15, 575-585.

TSUJI, Y., MORIKAWA, Y., AND TERASHIMA, K., 1982."Fluid-dynamic interaction between two spheres". International Journal of Multiphase Flow, Vol.8, 71-82.

ÜNAL, M.F., AND ROCKWELL, D., 1988. "On vortex formation from a cylinder. Part I. The initial" Journal of Fluid Mechanics, 19: 491-512.

WEI, Q., LIN, R., AND LIU, Z., 1998. „Vortex-induced Dynamic Loads on a Non-spinning Volleyball" Fluid Dynamics Research, V. 3, N.1-4, p.231-237.

WEI, T., AND SMITH, C.R., 1986. "Secondary vortices in the wake of circular cylinder". Journal of Fluid Mechanics, 169:513-533.

WERLE H., 1980. "ONERA photograph In: An album of fluid motion (assembled by Dyke V)". Parabolic Press, Stanford, pp 32–35.

WESTERWEEL, J,. 1993. "Digital particle image velocimetry, theory and application." Delft University Press.

WILLIAMSON, C. H. K., AND GOVARDHAN, R., 1997. "Dynamics and Forcing of a Tethered Sphere in a Fluid Flow", Journal of Fluids and Structures, 11 , 293–305.

WU JS., AND FAETH GM., 1993, "Sphere wakes in still surroundings at intermediate Reynolds numbers". AIAA J Vol.31, Issue.8, p.1448–1455.

WU, J.S., AND FAETH, GM., 1994. "Sphere Wakes at Moderate Reynolds Numbers in Turbulent Environment", AIAA Jounal, Vol.32, No. 3, 535-541.

YOUNG II, JANG., AND SANG JOON, LEE., 2008. "PIV analysis of near-wake behind a sphere at a subcritical Reynolds number", Experiments in Fluids, Vol. 44, Issue 6, pp.905-914.

YUN, G., KIM, D., AND CHOI, H., 2006. "Vortical structures behind a sphere at subcritical Reynolds numbers." Phys Fluids, Vol. 18(1), 015102.

YUTAKA, T., YOSHINOBU, M., AND KOZO, T., 1982. "Fluid-Dynamic Interaction Between Two Spheres", International Journal of Multiphase Flow ,Vol. 8, Issue 1, pp.71-82.

ZHU, C., LIANG, S. C., AND FAN, L.-S., 1994. "Particle wake effects on the drag force of an interactive particle, International Journal of Multiphase Flow", 20, 117-129.

CIRRICULUM VITAE

Engin PINAR was born on 1981 in Mersin, Turkey. He graduated from Hacı Ömer Sabancı High School, and enrolled in Mechanical Engineering Department of Mustafa Kemal Üniversty in 2000, He began his MSc education at the Department of Mechanical Engineering of Çukurova University in 2005. He completed his Master of Science education in 2009.